

Computational Fluid Dynamics of Supersonic Retro-propulsion for Elipsled Geometry

a project presented to
The Faculty of the Department of Aerospace Engineering
San José State University

in partial fulfillment of the requirements for the degree
Master of Science in Aerospace Engineering

by

Matthew Humphries

May 2018

approved by

Dr. Periklis Papadopoulos
Faculty Advisor



Table of Contents

Abstract	3
1. Introduction	3
2. Supersonic-Retro-propulsion Flow Field Characteristics	4
3. Previous Experimental Results.....	5
3.1 Single Centered Nozzle Engine Configuration	5
3.2 Tri Nozzle Engine Configuration.....	7
3.3 Quad Nozzle Configuration	7
4. Computational Fluid Dynamics Validation of Experiments.....	9
4.1 CFD - Single Nozzle Engine Configuration	9
4.2 CFD - Tri Nozzle Engine Configuration	10
4.3 Quad Nozzle Engine Configuration	11
4.4 Outer Nozzle Configurations.....	12
5. Large Body Geometries.....	13
6. Methodology	14
7. Design	14
8. Testing.....	19
9. Elipsled Results	24
9.1 Nozzles normal to the body	25
9.1.1 Mach 1 Simulations.....	25
9.1.2 Mach 2 Simulations.....	29
9.1.3 Mach 2.5 Simulations.....	33
9.1.4 Mach 3 Simulations.....	37
9.1.5 Mach 4 Simulations.....	41
9.2 Mesh Refinement	45
10. Future Work.....	51
11. Summary.....	51
Appendix A - Mesh Temperature and Pressure Figures	54
Appendix B - Bell Nozzle MATLAB Code	79

Abstract

Supersonic retro-propulsion is becoming a leading design to allow for high mass payloads to safely reach the surface of Mars during entry, descent and landing. Research has been conducted largely on sphere-cone shaped geometries with different jet stream nozzle engine configurations. A single centered engine shows to have the best stability when at high Mach numbers, high coefficient of thrust, and a large range of angles of attack. Tri and quad nozzle engine configurations increase the amount of retro-propulsion thrust possible, but limit the flight characteristics because they form unsteady shock waves and flow around the vehicle. Designing multi-nozzle engine configurations and large body geometries are becoming of much interest as high mass payloads will not be able to EDL to Mars using sphere cone designs. Elipsled type geometries have limited research, but may show promise. A parametric study was performed focusing on ranging free stream velocities and angles of attack.

Nomenclature

EDL	=	entry, descent, landing
C_t	=	coefficient of thrust
TPS	=	thermal protection system
UPWT	=	Unitary Plan Wind Tunnel
SRP	=	Supersonic Retro-propulsion
M	=	Mach number
Re	=	Reynolds number
c_p	=	pressure coefficient
Qdot	=	max dynamic pressure
α , AOA	=	angle of attack, deg
β	=	angle of yaw, deg
ϕ	=	model roll, deg
T	=	temperature, deg-F
X, Y, Z	=	tunnel coordinate system, in
x, y, z	=	model coordinate system, in

1. Introduction

Mars exploration is the future of the aerospace industry and is directing the interest of many companies to put a human on Mars. Over the past decades, man has accomplished to send multiple rovers to the surface of Mars. Each successful landing of a rover, verified a possible technique to reach the surface safely. However, the mass of these rovers has not required a change in the design of the transporting vehicle. A human capsule and supporting supplies has the possibility of reaching fifty metric tons or more. Previous EDL techniques will not suffice to land a human safely on the surface. The search to find new techniques, technologies and vehicle geometries has become one of the main points of research and design.

Supersonic retro-propulsion is the technique of using propulsion to decelerate a capsule upon entry into an atmosphere [2][3][8][11]. Built into the heat shield of the capsule are one or many jet stream nozzle engines that are used to inject engine thrust into the oncoming supersonic flow. Combining this with different amounts of C_t and changing the angle of attack, entering, descending and landing on the surface of Mars with a high mass payload may be

*Graduate Student, San Jose State University Aerospace Engineering, 119 S. 4th St. San Jose, CA 95112, AIAA Student Member.

accomplished. Previous research was being conducted on the best size and shape of sphere-cone fore-bodies, as well as the configurations of nozzle engines.

Sphere-cone fore-bodies limit the size of the payload. Using a different shaped fore-body, while including retro-propulsion nozzles will allow for larger shaped payloads that are not restricted to the size limitations of a sphere-cone. SpaceX has released information of a shuttle type geometry that will perform a vertical landing on Mars after aero-braking through Mars' atmosphere [16].

2. Supersonic-Retro-propulsion Flow Field Characteristics

For spherical cone vehicle shapes with a single nozzle engine at the center, the flow field can be seen in figure 1. As the supersonic flow moves towards the vehicle a bow shock will form. When no jet flow is inserted into the flow, the bow shock is close to the vehicle. Upon inserting jet flow from the nozzle into the flow, it pushes the bow shock away from the surface of the vehicle. The jet flow is contained within shear layers and is ended at a terminal shock. At the point where the opposing velocities meet and the velocity goes to zero, this is called the interface. As the free stream flow meets the jet flow, the jet flow is recirculated. At the point where the supersonic free stream flow, subsonic shock flow, and the subsonic recirculating flow meet is called the triple point [4].

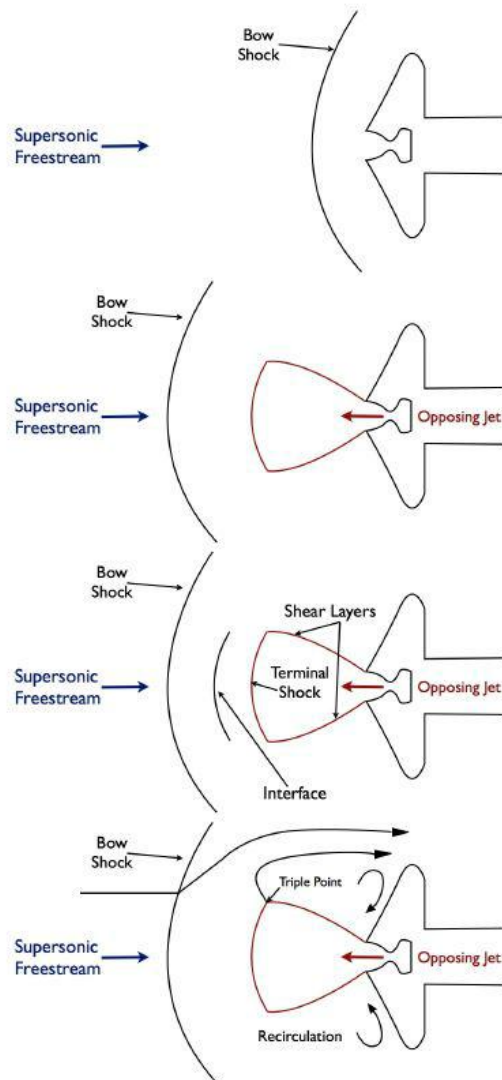


Fig. 1 SRP flow field characteristics [4]

3. Previous Experimental Results

Table 1 SRP flow field characteristics [4]

Step	Parameter of Interest	Typical Settings
1	Set Model Configuration and Roll Increment	Baseline, Center, Tri, Quad, Roll = 0 and 180
2	Set Tunnel Flow Conditions	$M = 1.8/Re = 1.5$, $M = 2.4/Re = 1$, $M = 2.4/Re = 1.5$
3	Set Nozzle Thrust	$C_t = 0, 2, 4, 6, 8, 10$
4	Set Model Position	$Z = 0, \pm 12, \pm 24$
5	Conduct Alpha Sweep in the horizontal plane	$\alpha = 0, \pm 4, \pm 8, 12, 16, 20$
6	Conduct Beta Sweep in the vertical plane for schlieren	$\phi = 0, 4, 8, 12$

3.1 Single Centered Nozzle Engine Configuration

Experimental scale model testing conducted at NASA Langley Unitary Plan Wind Tunnel consisted of a 5-in diameter, 70-deg sphere-cone fore-body with a roughly 10-in long cylindrical aft-body. Testing was conducted using a unitary plan wind tunnel supersonic retro-propulsion model assembly, which had locations for 4 nozzle engines that could be plugged for separate experiments which can be seen in figure 2. Nozzle engine configurations can be better seen in figure 3, which also includes instrumentation holes around the surface of the cone [2].

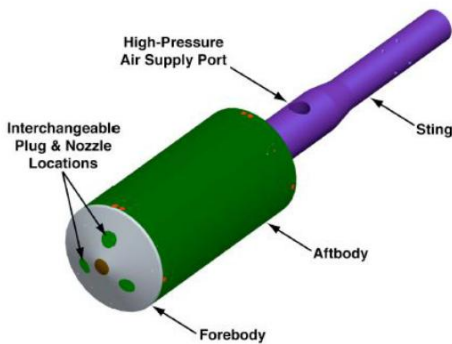


Fig. 2 UPWT SRP model assembly [2]

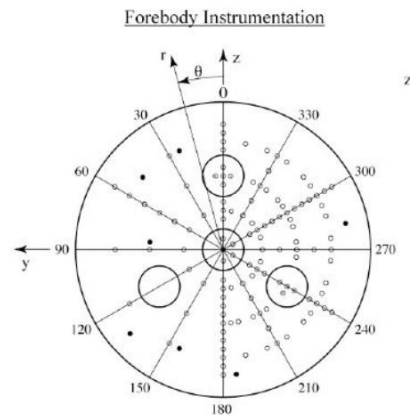
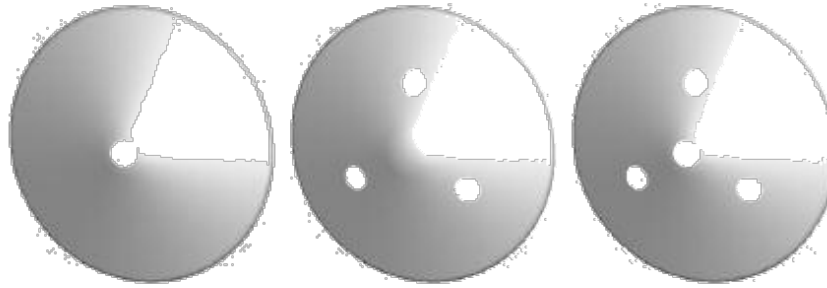


Fig. 3 UPWT SRP model assembly instrumentation [2]

When all 4 nozzle engines are plugged, this was considered the base line configuration. Sphere-cone fore-body has been heavily tested and thus is used to confirm controlled testing. The center nozzle engine configuration was heavily tested as discussed later in this paper. Three of the nozzle engines were spaced radially 120° apart as seen in figure 3. This nozzle engine configuration was used when conducting the peripheral nozzle engine experiments. When all four nozzle engines were being used, this was considered the quad nozzle engine configuration, seen in figure 4, and was the lowest on the priority list to conduct experiments for [2].



Single (left), Tri (center), Quad (right)

Fig. 4 Nozzle configurations. [6]

Seen below in figure 5, the baseline sphere-cone fore-body with no nozzle engines injecting flow produces a steady bow shock around the model. Increasing the Mach number does not cause unsteadiness and further pushes the bow shock closer to the model [2].



Mach 2.4(left), Mach 3.5(center), Mach 4.6(right)

Fig. 5 Single nozzle without jet stream injected. [2]

When injecting the jet flow, the bow shock standoff distance increased greatly at roughly 300% [2]. As C_t increases, the standoff distance increased again. The center nozzle design provided the most stable flow field for angles of attack below 10° and for all Mach numbers, as well as coefficients of thrust [2][3][4][5].



Fig. 6 Single nozzle $C_t = 0.5$ Mach 2.4. [2]



Fig. 7 Single nozzle $C_t = 4$ Mach 2.4. [2]

Adjusting the angle of attack to 12° while at Mach 4 produces an unsteady flow on the lower portion of the bow shock. It can easily be seen when compared to when the angle of attack is at 0° seen in figure 8 and figure 9 [2][3][4][5].



Fig. 8 Single nozzle, $\alpha = 0$ -deg, $C_t = 4$, Mach 4.6. [2]



Fig. 9 Single nozzle, $\alpha = 12$ -deg, $C_t = 4$, Mach 4.6. [2]

3.2 Tri Nozzle Engine Configuration

The tri-nozzle engine design produced significantly more unsteadiness in the flow field compared to the single nozzle. As C_t and Mach number increased, bow shock oscillations resulted forming an unsteady flow field. This was also true when angle of attack was increased or decreased from 0. The tri-nozzle engine design did have a lower standoff distance of the bow shock because the three nozzles caused a lower pressure ratio across the sphere-cone fore-body [2][3][4][5].



Fig. 10 Tri-Nozzle, $C_t = 2$, Mach 2.4. [2]



Fig. 11 Tri-Nozzle, $C_t = 4$, Mach 4.6. [2]

3.3 Quad Nozzle Configuration

The quad-nozzle engine design also proved to produce unsteadiness in the flow field. However it was less than that of the tri-nozzle engine in certain conditions [2][3][4][5].



Fig. 12 Quad-Nozzle, $\alpha = 0$ $C_t = 2$, Mach 2.4.[2]



Fig. 13 Quad-Nozzle, $\alpha = 4$ $C_t = 2$, Mach 2.4. [2]



Fig. 14 Quad-Nozzle, $\alpha = 8$ Ct =2, Mach 2.4.[2]



Fig. 15 Quad-Nozzle, $\alpha = 12$ Ct =2, Mach 2.4.[2]



Fig. 16 Quad-Nozzle, $\alpha = 16$ Ct =2, Mach 2.4.[2]

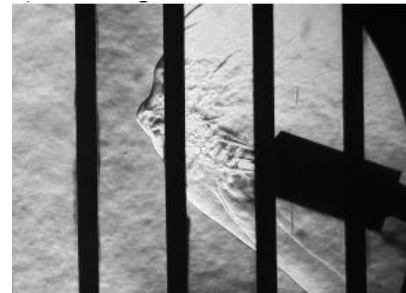


Fig. 17 Quad-Nozzle, $\alpha = 20$ Ct =2, Mach 2.4.[2]

When rolling the UPWT SRP model, it reduces the unsteadiness in the quad nozzle configuration. This could be a result of the nozzles being in a different orientation to the oncoming flow. It can be seen when comparing high angle of attack experiments seen below. The unsteadiness when the quad nozzle configuration is rotated by 180° is the most decreased at an angle of attack of 20°. The bow shock at the front is much stronger and is clearly defined [2][3][4][5].



Fig. 18 Quad-Nozzle, $\alpha = 16$ Ct =2, $\phi = 0$ Mach 2.4.[2]



Fig. 19 Quad-Nozzle, $\alpha = 16$ Ct =2, $\phi = 180$ Mach 2.4.[2]

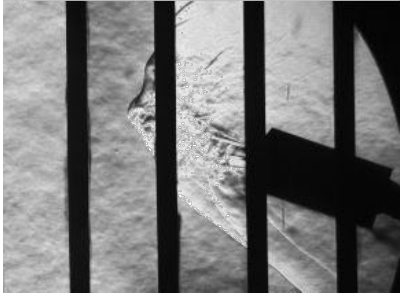


Fig. 20 Quad-Nozzle, $\alpha = 20$ $C_t = 2$, $\phi = 0$
Mach 2.4.[2]



Fig. 21 Quad-Nozzle, $\alpha = 20$ $C_t = 2$, $\phi = 180$
Mach 2.4.[2]

Further testing was conducted by researchers at NASA Ames Research Center and similar results were found. NASA Ames researchers conducted the same experiments with many of the same parameters as NASA Langley. NASA Ames was able to gather overlapping data showing that both experiments were valid. NASA Ames concluded that a single nozzle engine design was the best design for a large range of parameters. When comparing C_t for each nozzle engine design, the same thrust for the single nozzle engine produced a bigger and more stable jet stream and had the largest standoff distance for the bow shock. When changing the angle of attack, it was also noted that the single nozzle engine provided the best stability of the three designs [2][5].

4. Computational Fluid Dynamics Validation of Experiments

NASA Ames Research Center was successful in matching the real world experimental results that NASA Langley achieved at the Unitary Plan Wind Tunnel. NASA Ames used multiple computation fluid dynamic solvers to check these results, but this section only focuses on one, Data Parallel Line Relaxation. DPLR solves Reynolds-Averaged Navier-Stokes equations [4]. The results from DPLR showed the clearest similarities to the experimental results from NASA Langley and as such, makes it easier to compare them.

4.1 CFD - Single Nozzle Engine Configuration

Single nozzle engine configuration again can be shown to have steady bow shock waves around the vehicle. Upon increasing the angle of attack, some unsteadiness begins to occur on the lower portion of the flow field. Further increasing the angle of attack, increased unsteadiness in the lower portion occurs.

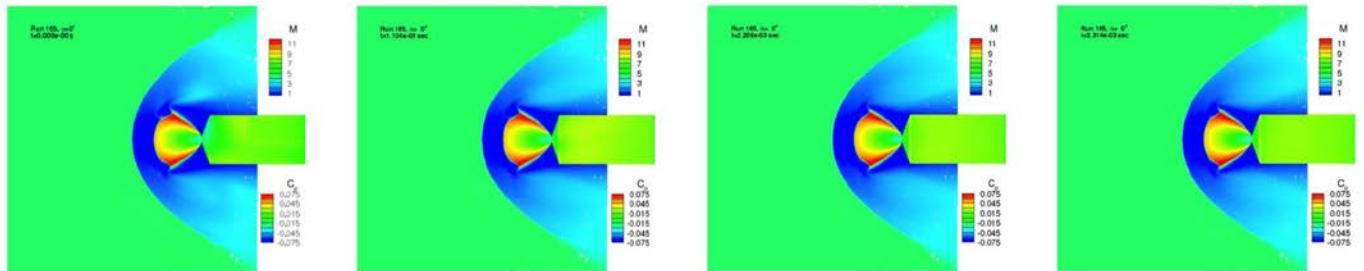


Fig. 22 $C_t = 2$, $\alpha = 0$ [4]

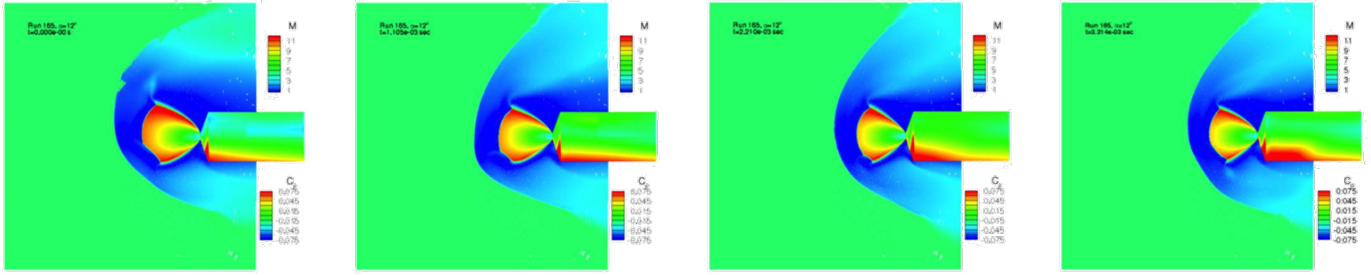


Fig. 23 $C_t = 2, \alpha = 12$ [4]

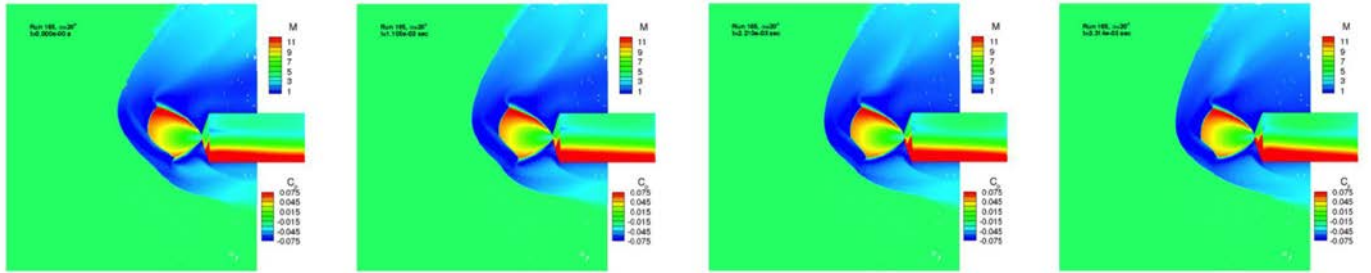


Fig. 24 $C_t = 2, \alpha = 20$ [4]

4.2 CFD - Tri Nozzle Engine Configuration

When looking at the tri nozzle engine configuration the flow is steady when the angle of attack is zero. Increasing the angle of attack results in very unsteady flow on the lower portion of the flow field. The flow field does seem to become steady at times, but overall continues to be unsteady.

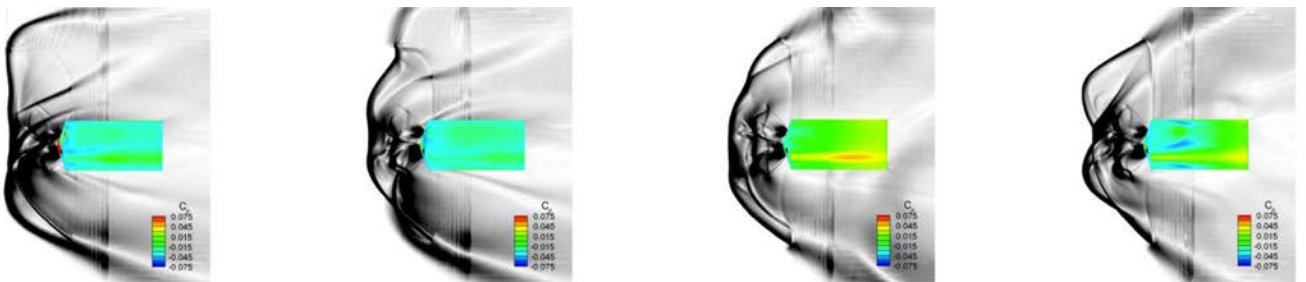


Fig. 25 $C_t = 3, \alpha = 0$ [4]

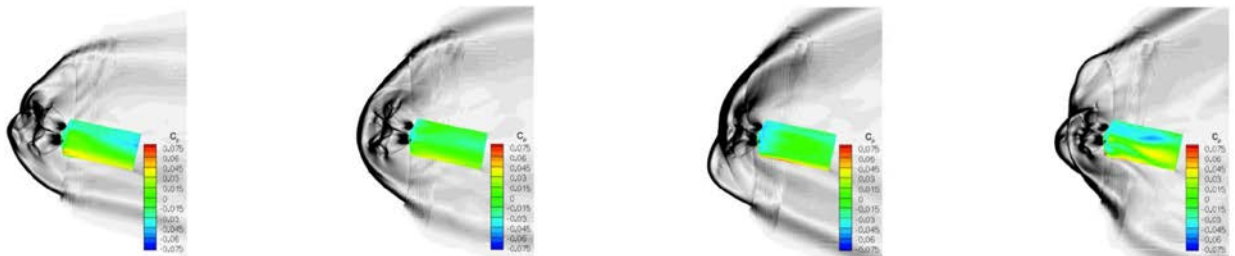


Fig. 26 $C_t = 3, \alpha = 12$ [4]

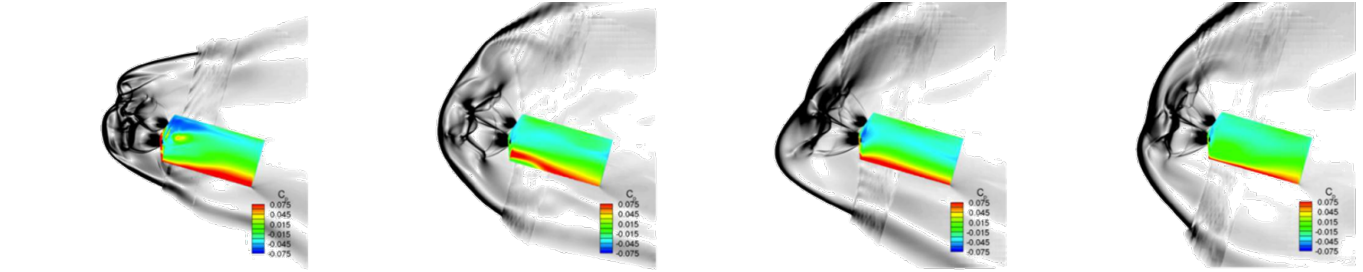


Fig. 27 $C_t = 3, \alpha = 16$ [4]

4.3 Quad Nozzle Engine Configuration

Unsteady flow continues when increasing the amount of nozzle engines to four. Again at zero angle of attack, the flow is steady and shock waves are clearly defined. Increasing the angle of attack causes unsteady flow, though not to the same extent as the tri nozzle configuration. This could be due to the single center nozzle increasing the stand off distance of the bow shock.

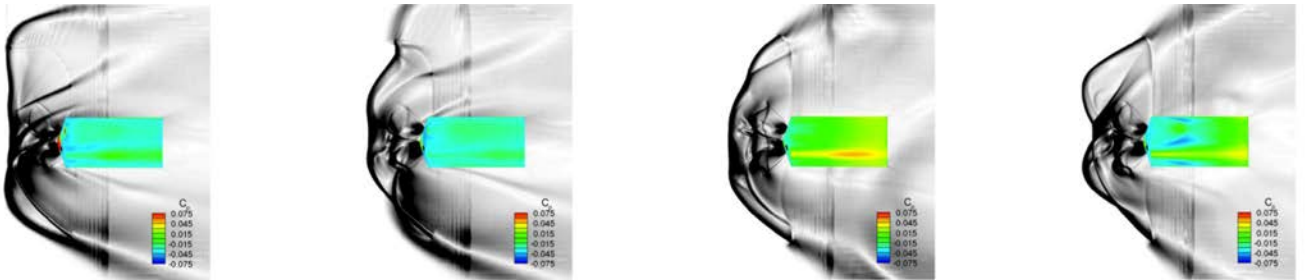


Fig. 28 $C_t = 3, \alpha = 0$ [4]

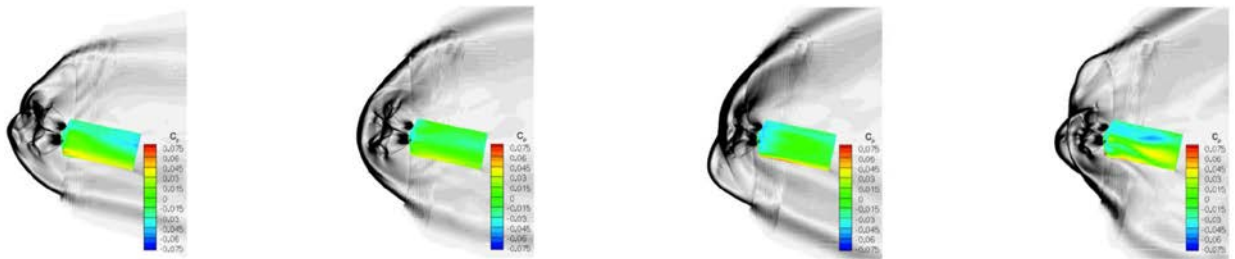


Fig. 29 $C_t = 3, \alpha = 12$ [4]

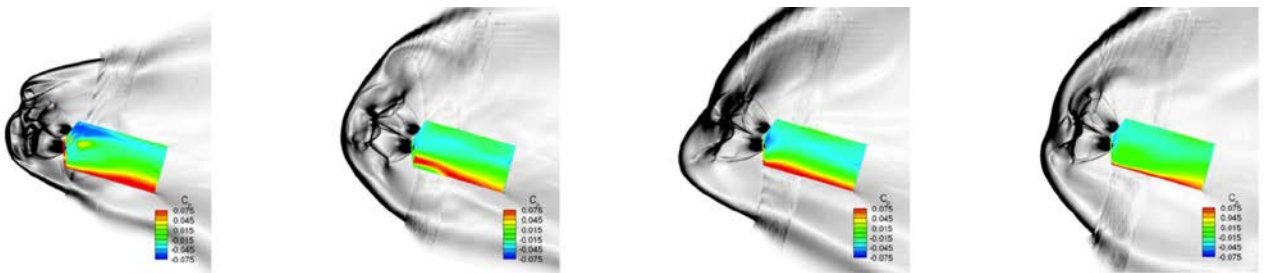


Fig. 30 $C_t = 3, \alpha = 16$ [4]

4.4 Outer Nozzle Configurations

It can be seen that when free stream flow meets the jet flow from the nozzle engine that the exhaust does not flow towards the center of the body, but around the body. Leaving the center of the body free of unstable flow. This can be further seen in Figure 32. In which the two exhausts do not interfere with each other.

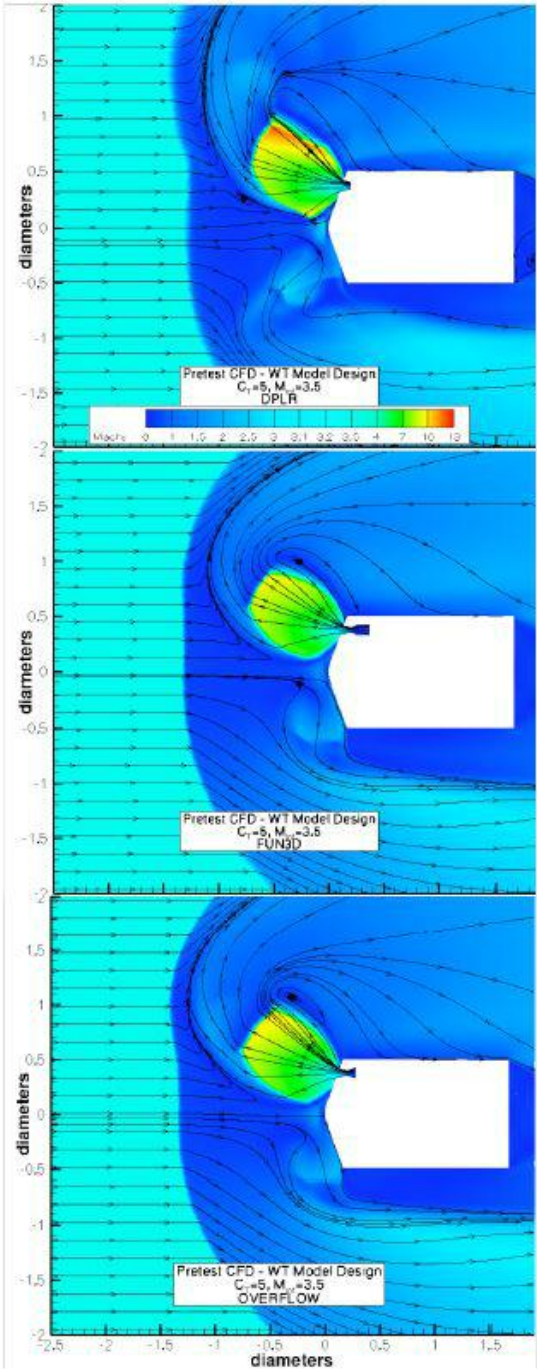


Fig. 31 Single Outer Nozzle [19]

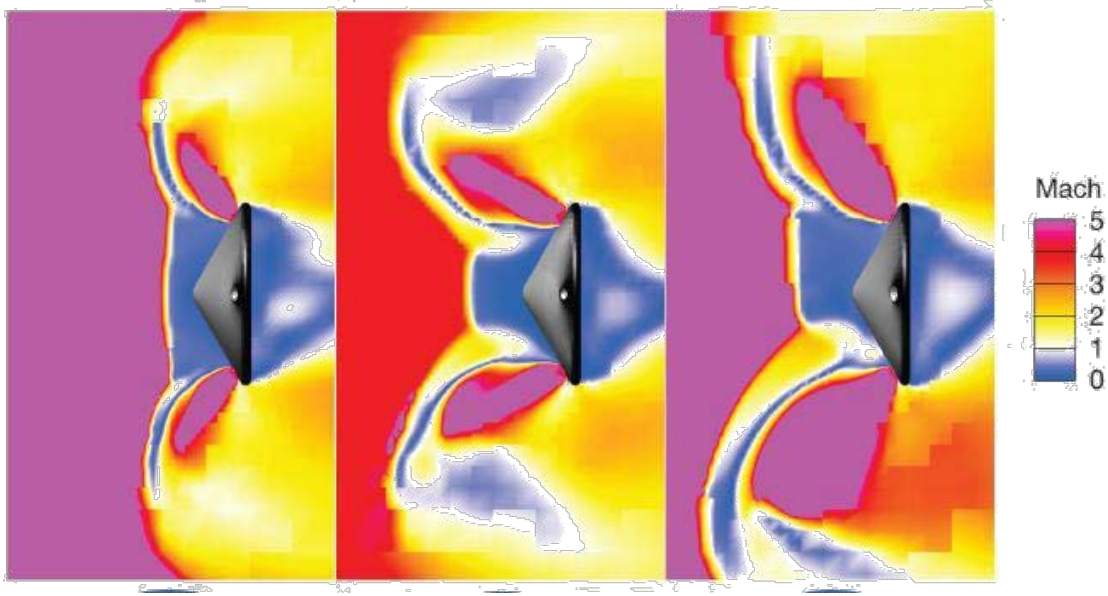


Fig. 32 Dual Outer Nozzles [20]

5. Large Body Geometries

Data on different supersonic retro-propulsive geometries is small and limited. Georgia Institute of Technology performed a study on an elipsled shape vehicle. It was found for high mass EDL, that a longer slender body could be used over a sphere-cone blunt body. With further research and by optimizing the elipsled's shape, it could show to have a higher mass payload [1][8]. This could result in a body that is similar in shape to that of the NASA Space Shuttle. The NASA Space Shuttle is a proven re-entry vehicle that had many successful flights and many experiments performed on its shape and design. This knowledge and data would help to design and create a large body geometry with SRP for the EDL on Mars.

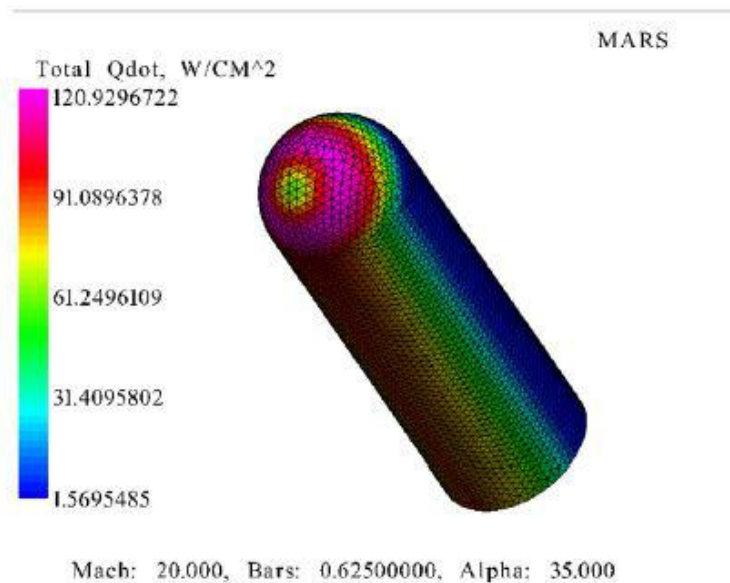


Fig. 33 Elipsled shape showing Total Qdot. [8]

6. Methodology

Geometry design was based upon current research and experimental results in the aerospace field. NASA Ames Research Center and Georgia Institute of Technology both were considered when designing the nozzle. A MATLAB script was written to create a bell nozzle design, as well as the requirements for the combustion chamber. Nozzle dimensions from MATLAB were then used to create the nozzle within Solidworks and exported for computational fluid dynamic validation within STAR-CCM+ software.

7. Design

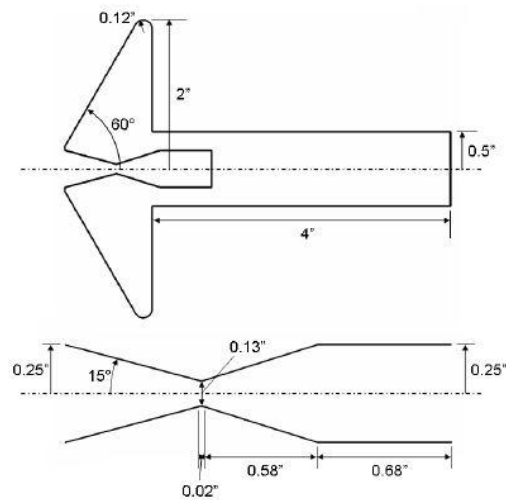


Fig. 34 Georgia Institute of Technology Single Nozzle Dimensions [7]

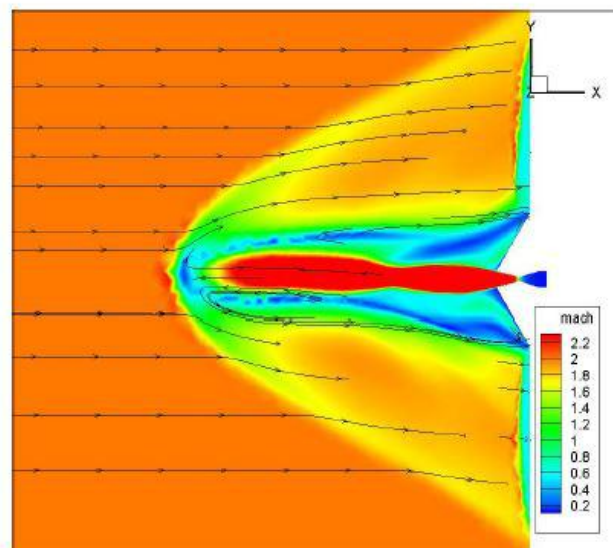


Fig. 35 Georgia Institute of Technology Bow Shock [7]

Bell nozzle design was achieved using MATLAB code that receives inputs such as estimated nozzle exit diameter, chamber pressure, and estimated thrust and outputs dimensions which when used with "The Thrust Optimized Parabolic

Nozzle" [18] technique. This gives an accurate bell nozzle shape to meet the input requirements. It also outputs correct dimensions for the combustion chamber and resulting pressures and temperatures to be used. An example case of the inputs and outputs can be seen below. MATLAB code can be found in Appendix B.

```

R = 8314;
G_0 = -9.8;
G_m = 3.711;

thrust = 600;
F_thrust = 0;
P_ambient = 101325;
P_exit = 101325;
dia_e = 0.0127;

Lstar = 0.9;
IT_ratio = 10 ;
theta_c = 40*pi/180;
theta_e = 15*pi/180;

% index of O/F Ratio used
i = 7;
% index of Pressure used
j = 7;

```

Fig. 36 MATLAB Code Inputs

```

conical_engine_misc =
                               Var1
                               -----
Contraction Angle    0.69813
Expansion Angle     0.2618
L*                   0.9
Epsilon             11.87
O/F Ratio           2.1

conical_engine_dims =
                               Metric    Imperial
                               -----    -----
Combustor Diameter   0.022671    0.89258
Throat Diameter     0.0071694    0.28226
Nozzle Exit Diamter 0.0247      0.97244
Length of Combustor 0.092845    3.6553
Length of Nozzle    0.032713    1.2879

Bell_engine_misc =
                               Var1
                               -----
Contraction Angle    0.69813
Expansion Angle      3
L*                   0.9
Epsilon             11.87
O/F Ratio           2.1

Bell_engine_dims =
                               Metric    Imperial
                               -----    -----
Combustor Diameter   0.022671    0.89258
Throat Diameter     0.0071694    0.28226
Nozzle Exit Diamter 0.0247      0.97244
Length of Combustor 0.092845    3.6553
Length of Nozzle    0.02617     1.0303
Expansion Radius     0.0013693    0.053911
Contraction Radius   0.005377     0.21169

```

Fig. 37 MATLAB Code Output

A custom MATLAB script was written to produce the correct bell nozzle dimensions and the correct combustion chamber dimensions for the fuel used. The fuel used for the calculations was liquid oxygen and methane, which is a fuel that is most likely to be used for Mars exploration for the ability to create both on the surface of Mars using the Sabatier process. Fuel characteristics were used for designing the engine and correct temperatures and pressures were used in the combustion chamber for testing. However, during CFD simulations, reactant flow was not used due to hardware and time limitations to perform the simulations.

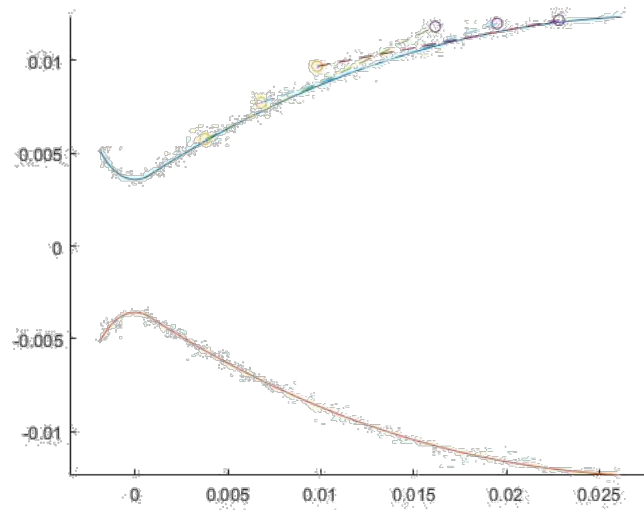


Fig. 38 MATLAB created Nozzle

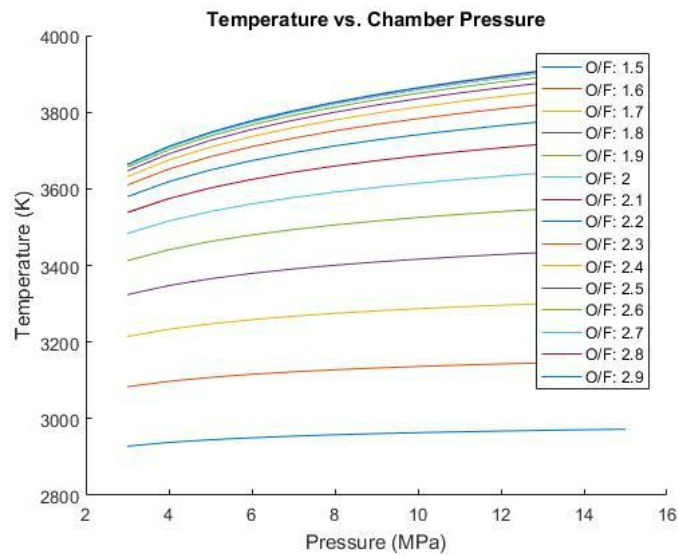


Fig. 39 MATLAB Temperature vs. Pressure

Given the dimensions for aspects of the nozzle from the MATLAB code, they can then be used to create the bell nozzle shape with "The Thrust Optimized Parabolic Nozzle" [18] technique. This primarily involves taking the throat radius and using an equation to apply it to the radii of two circles, one of which is within the other. This provides the correct shape for the throat and continuing out the bell nozzle.

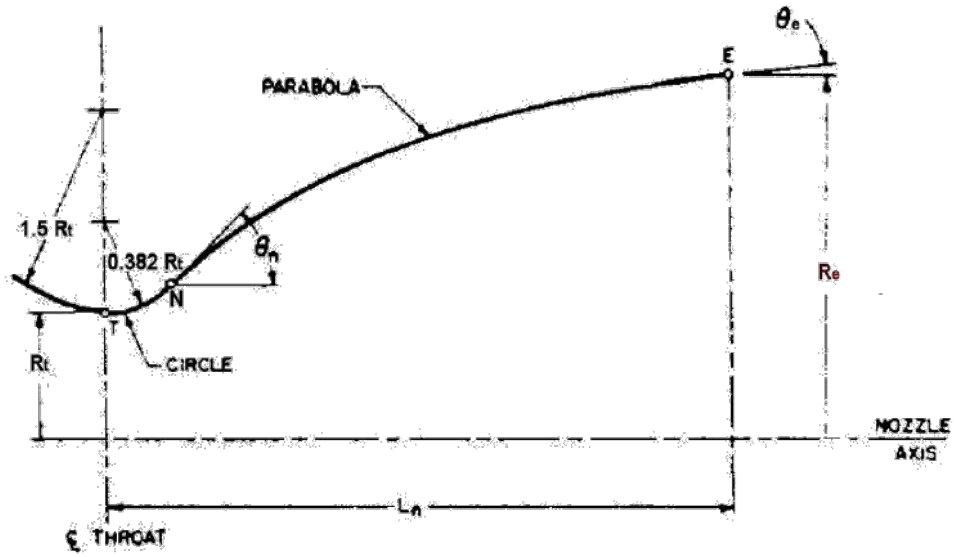


Fig. 40 Nozzle Diagram Geometry [18]

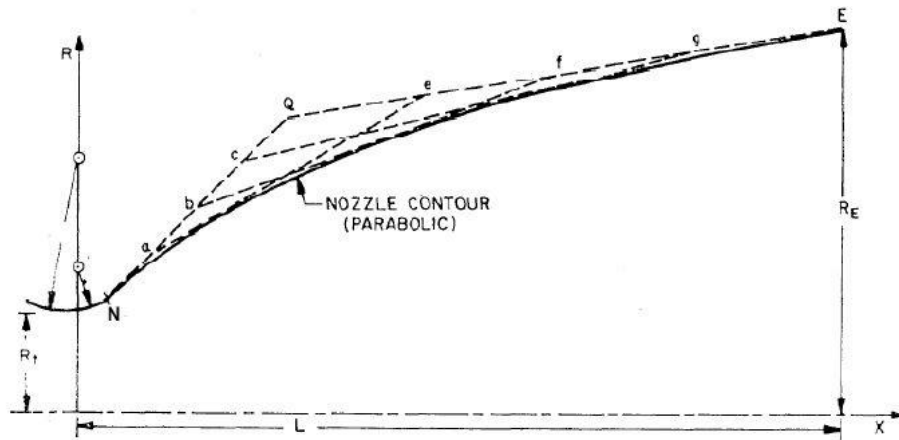


Fig. 41 Nozzle Contour Technique [18]

Taking the given outputs from MATLAB and using the bell nozzle geometry technique, a bell nozzle similar in size to the Georgia Institute of Technology conical nozzle can be created with Solidworks which then can be manipulated and output to the correct file type to be imported into STAR-CCM+. Within STAR-CCM+, a control volume mesh and mesh refinement will be performed.

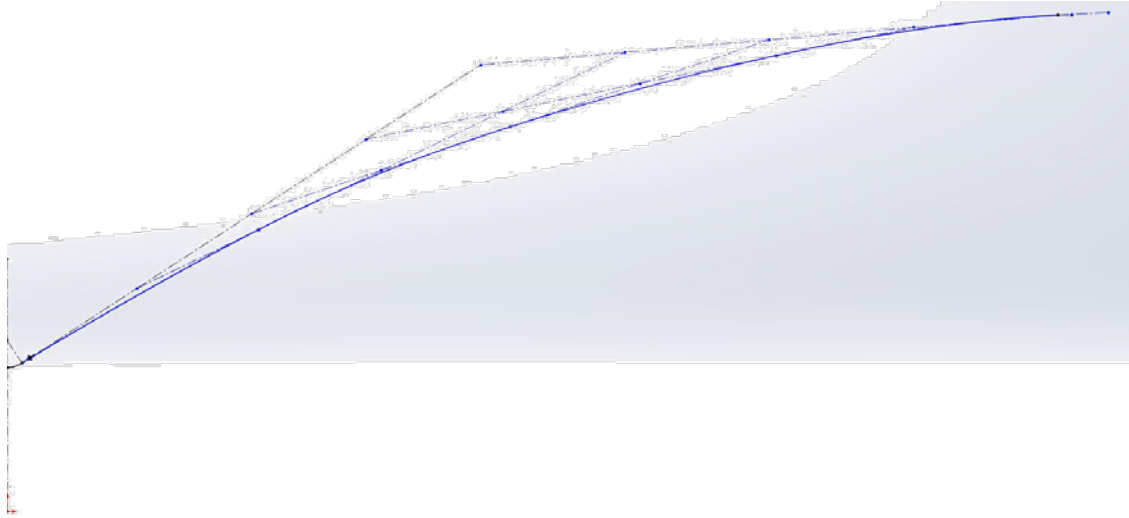


Fig. 42 Bell Nozzle Geometry

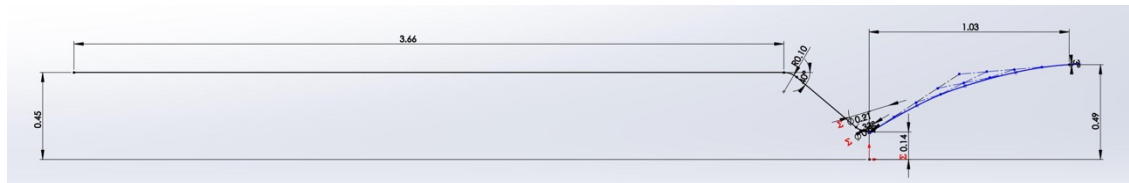


Fig. 43 Designed Engine Outline

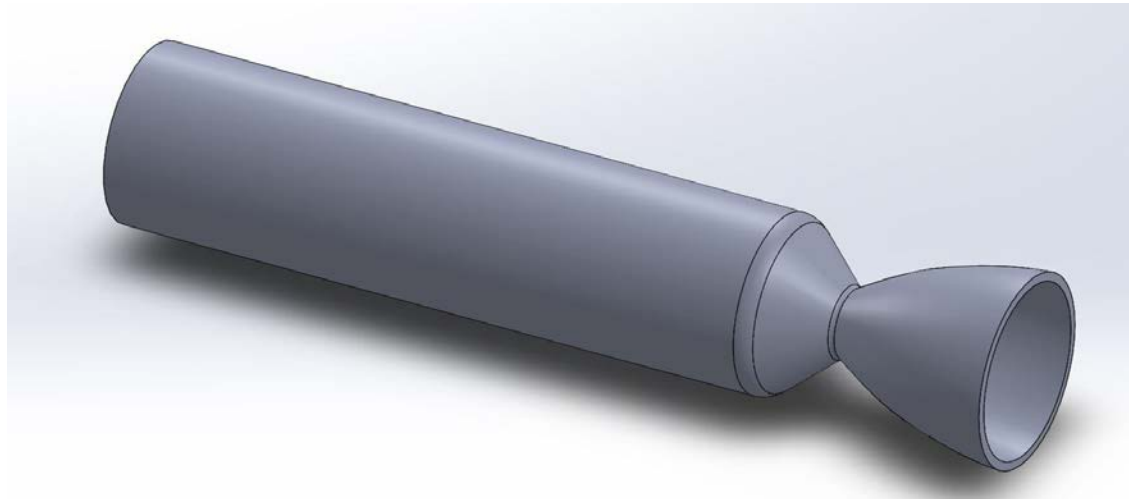


Fig. 44 Designed Engine Revolve



Fig. 45 Solidworks Model for STAR-CCM+ Import

8. Testing

Simulation environment for all simulations, consisted of:

- steady state
- turbulent
- coupled energy
- viscous
- ideal gas
- Mach 3 free stream flow entering the control volume from the right side.
- The top and left wall were pressure outlet boundary layers. The bottom wall was axisymmetric.

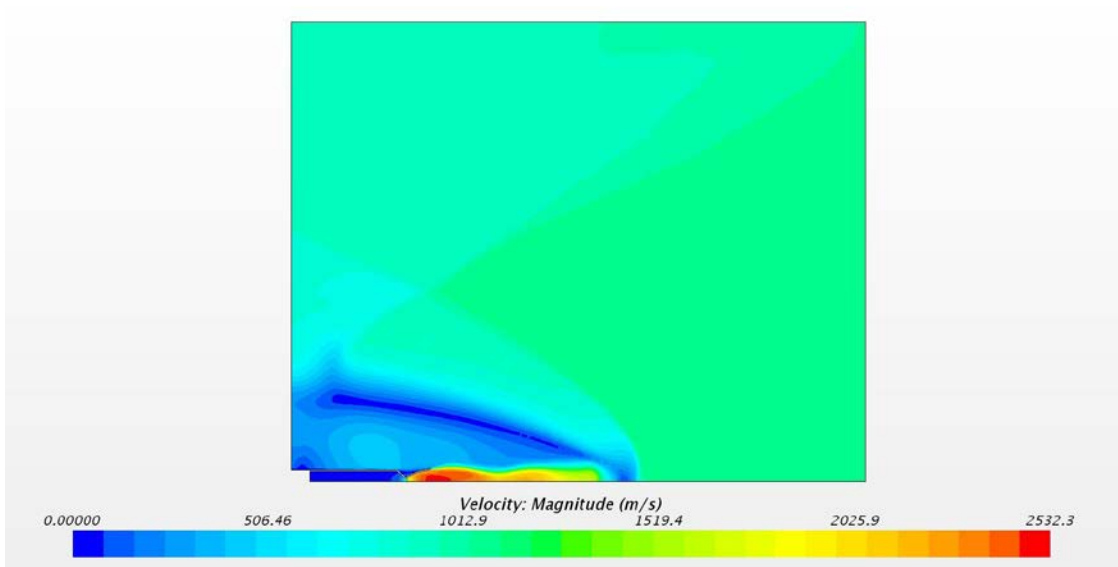


Fig. 46 Velocity Magnitude with Mach 3 free stream

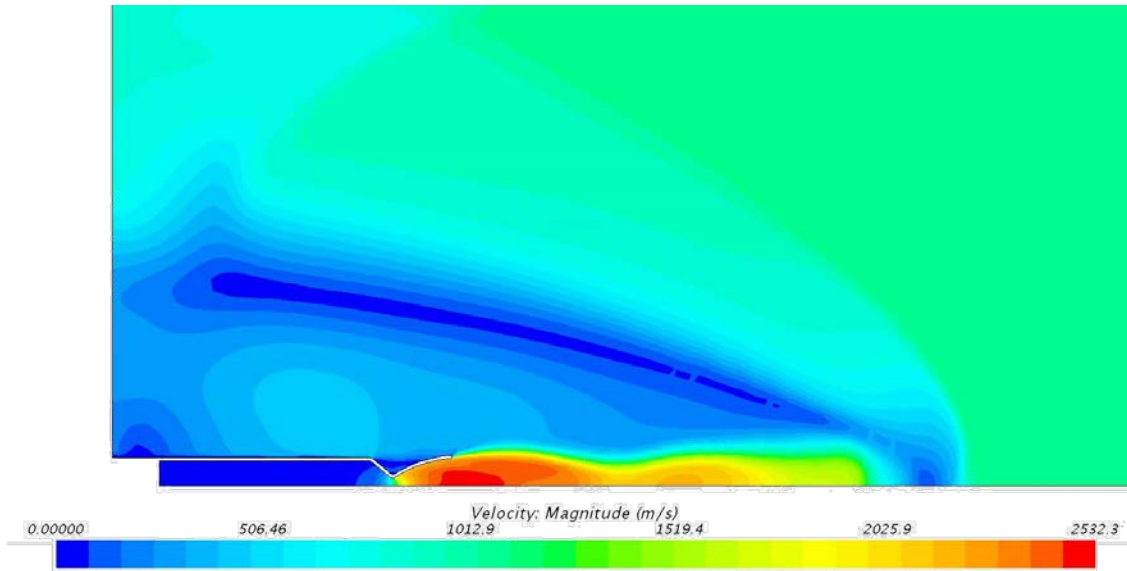


Fig. 47 Velocity Magnitude with Mach 3 free stream zoomed

As can be seen in the velocity magnitude figures, the exhaust plume extends into the free stream flow where it terminates at a bow shock. The bow shock can be seen extending back towards and around the nozzle.

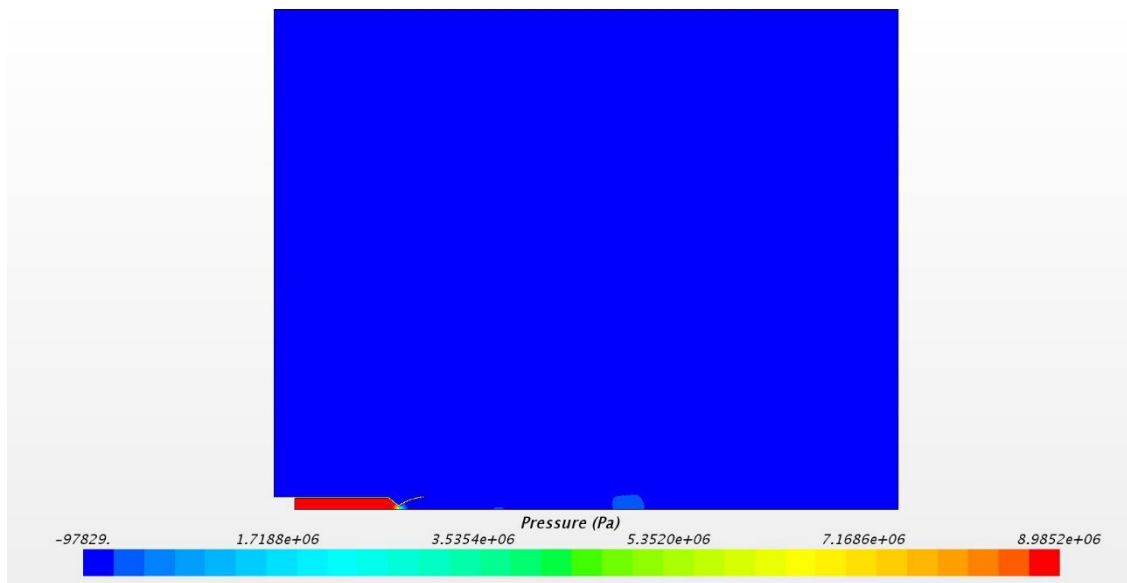


Fig. 48 Pressure

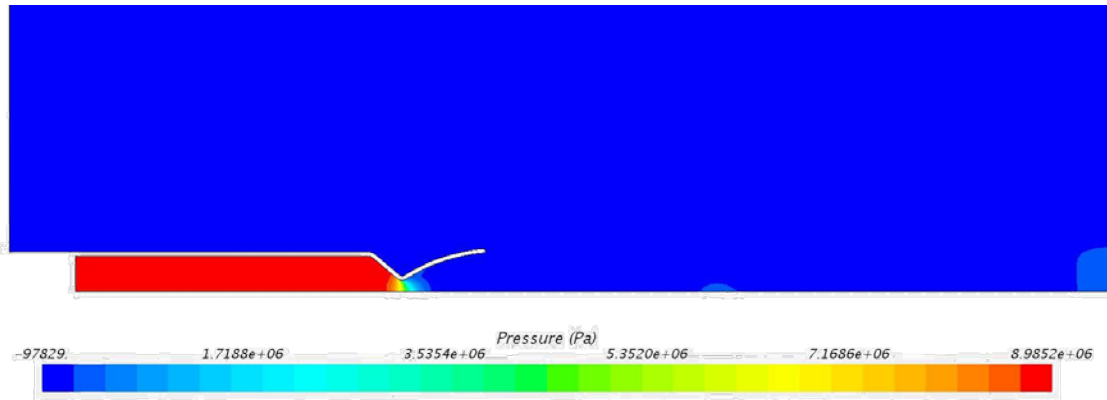


Fig. 49 Pressure Zoomed

Pressure figures show that the pressure within the combustion chamber is 9 MPa which is what was used in the MATLAB script for the designed nozzle. Pressure can be seen to dramatically decrease as it reaches the throat of the nozzle.

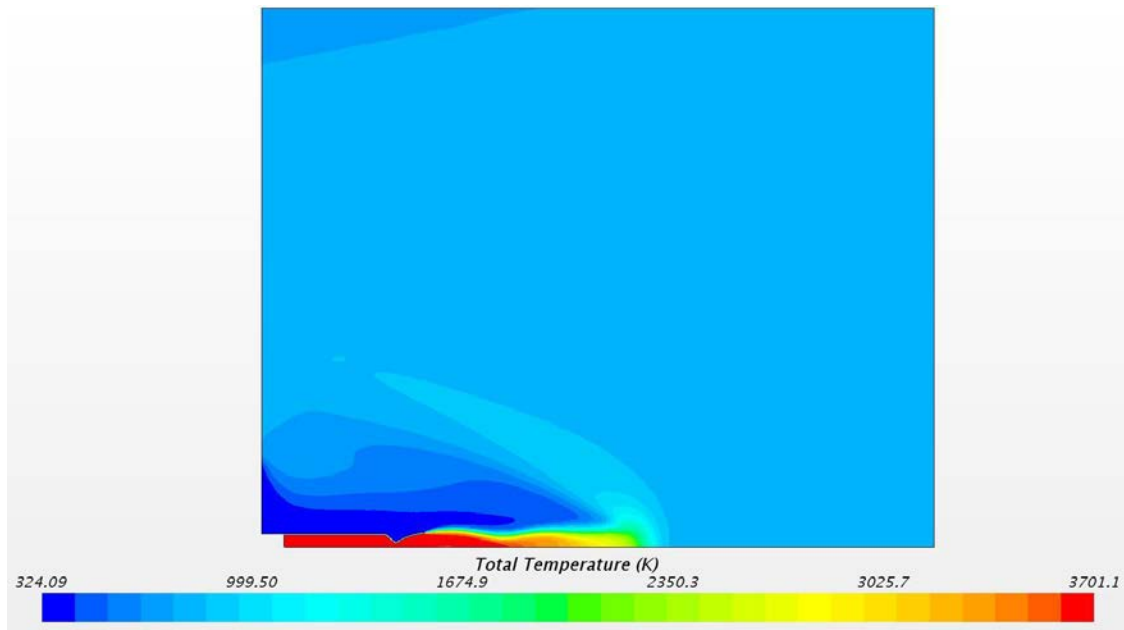


Fig. 50 Temperature

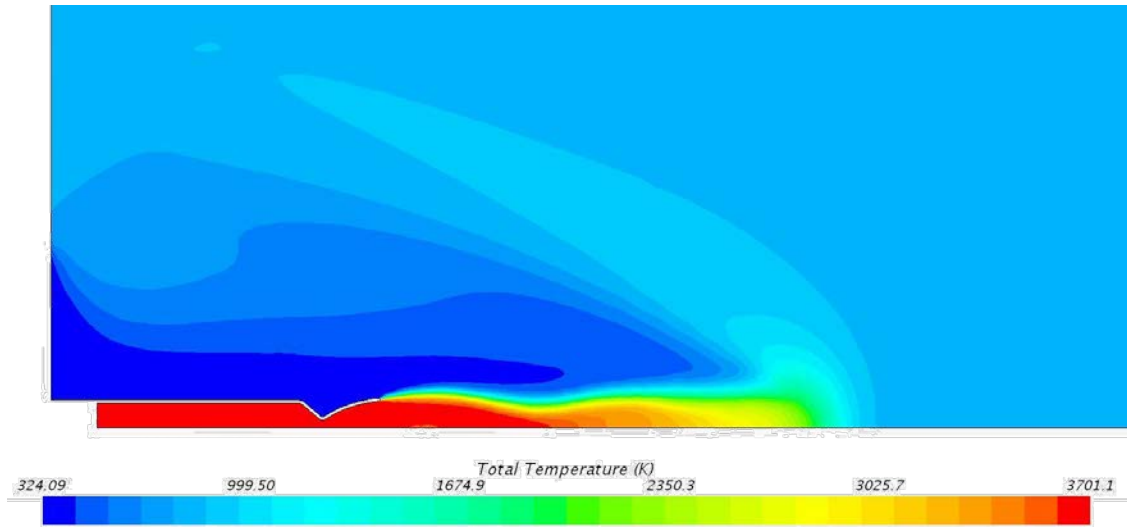


Fig. 51 Temperature Zoomed

As with the pressure figures, temperature figures show the correct temperature within the combustion chamber which was set to 3750 Kelvin in the MATLAB script.

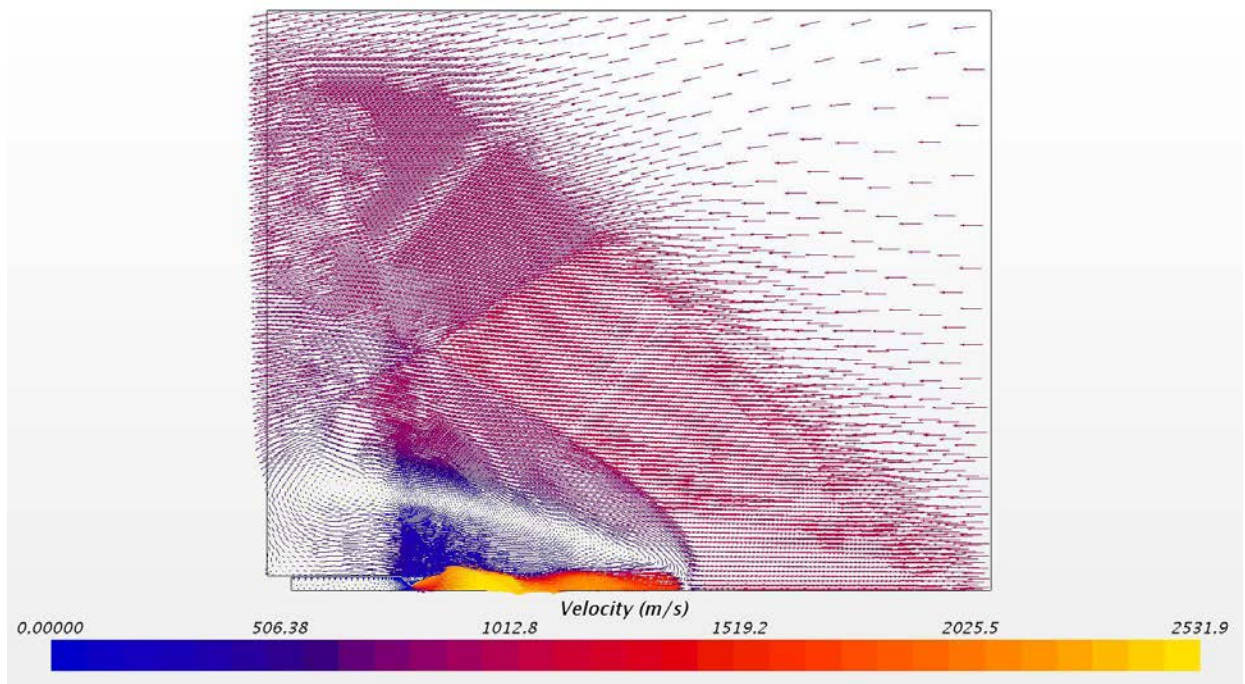


Fig. 52 Vector Velocity Magnitude

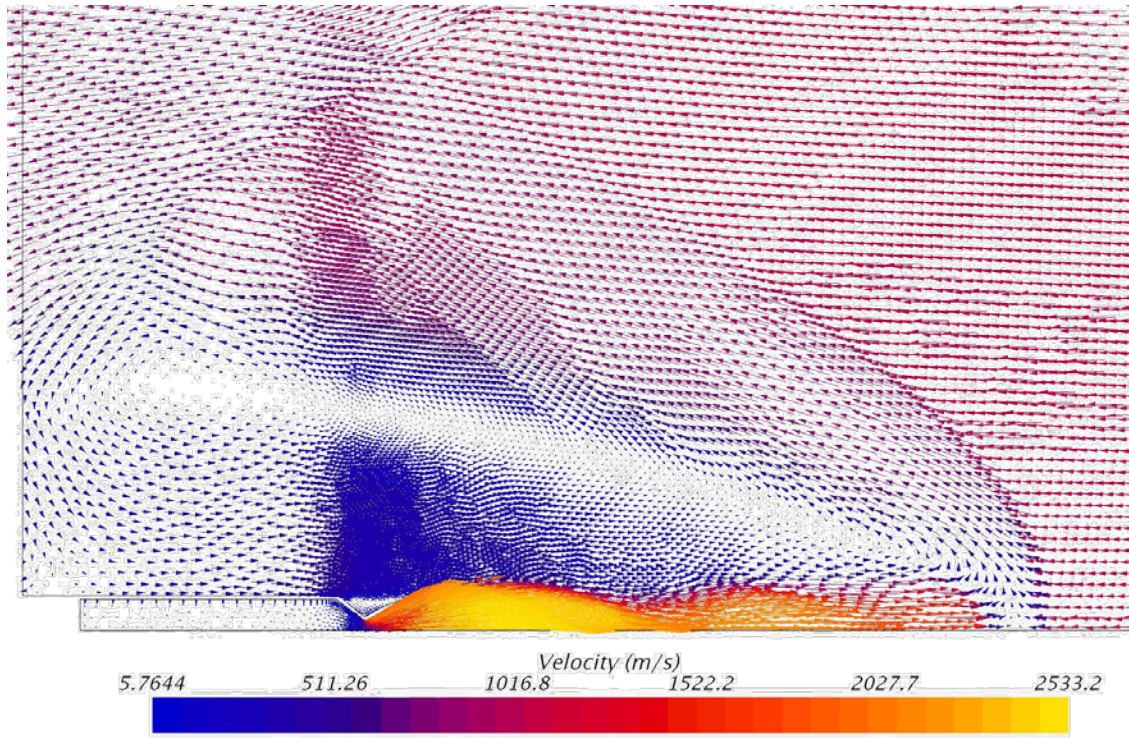


Fig. 53 Vector Velocity Magnitude Zoomed

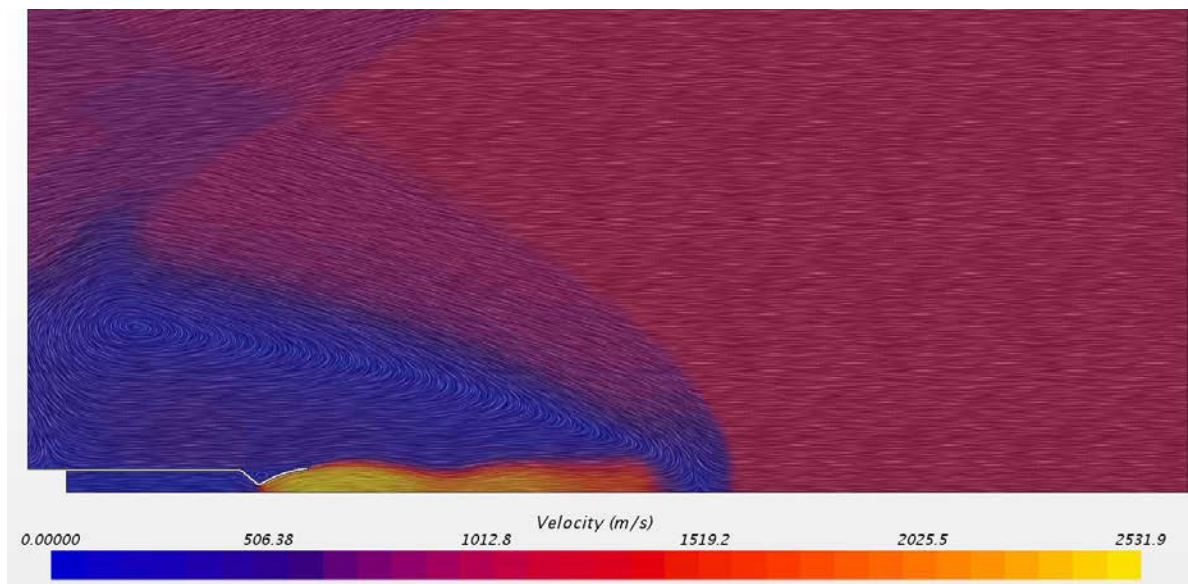


Fig. 54 Vector Velocity Magnitude Zoomed

Velocity vector figures further show how the exhaust plume extends and ends at a bow shock. This type of figure really outlines the bow shock and how the flow is redirected back towards the nozzle. With the results seen from the single nozzle engine testing, the flow characteristics are similar to that of NASA and Georgia Institute of Technology seen in Figure 8 and Figure 35. For this reason, this nozzle design will be used for the elipsled geometry model.

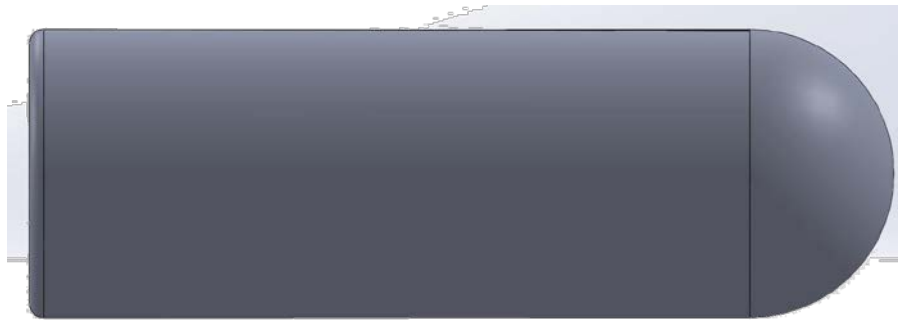


Fig. 55 Solidworks Model of Elipsled

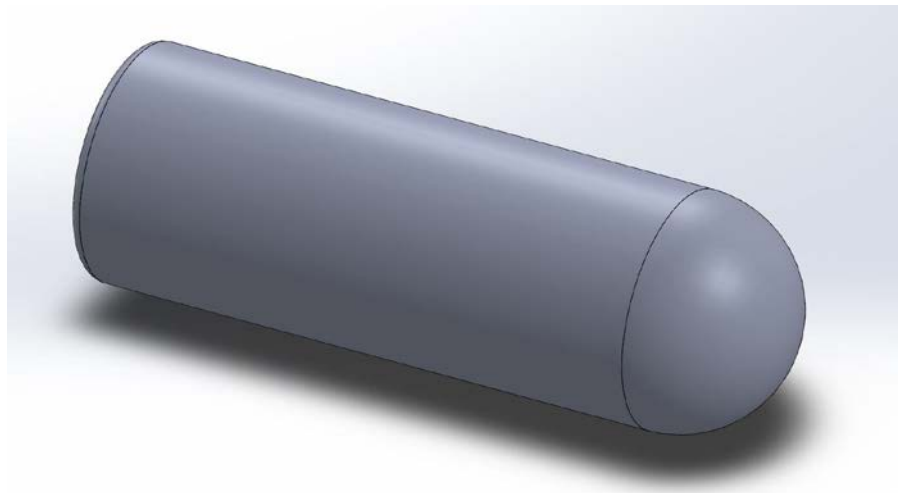


Fig. 56 Bottom View of Elipsled

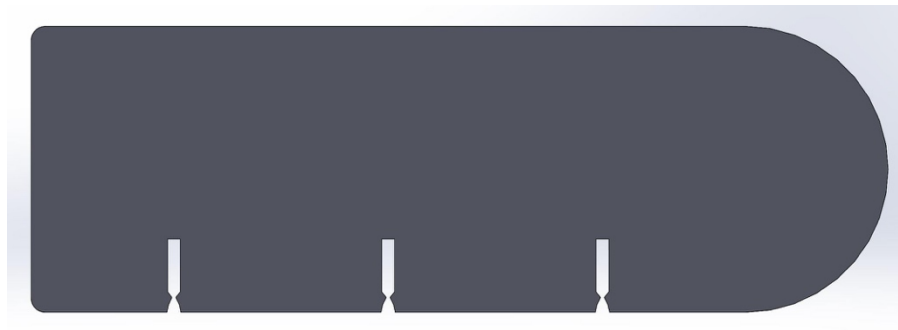


Fig. 57 Nozzles facing Normal to the Body

9. Elipsled Results

A sweeping study of multiple angles of attack at ranging free stream velocities was performed. Free stream velocities began at Mach 1 and increased to Mach 5. Starting at 15° angle of attack to the free stream flow, the angle was increased to 30°, 60° and finally 90°. The results can be seen below.

9.1 Nozzles normal to the body

9.1.1 Mach 1 Simulations

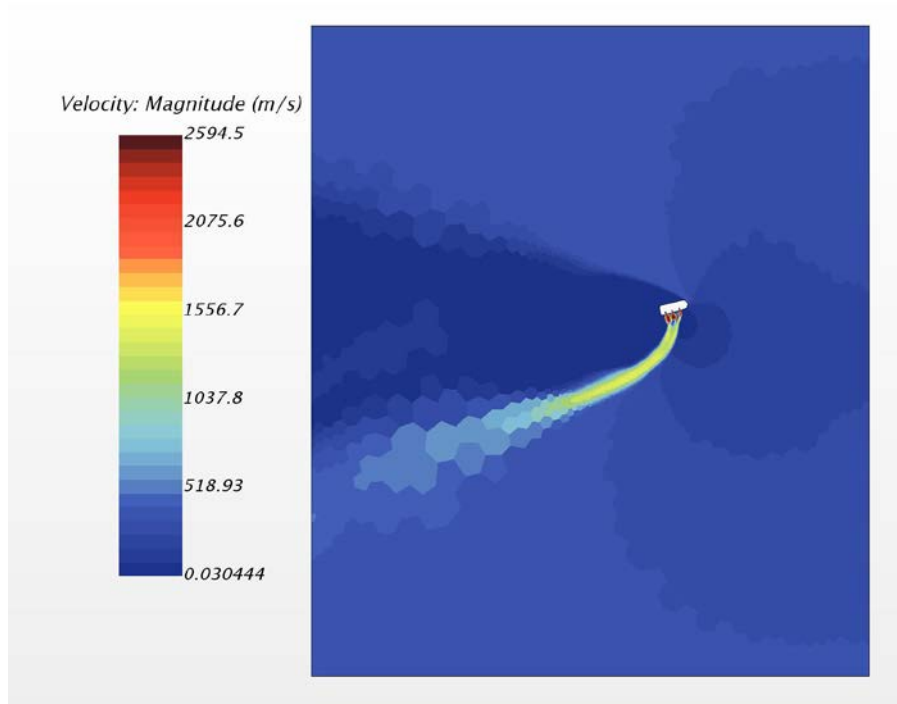


Fig. 58 $\alpha = 15^\circ$, Mach 1

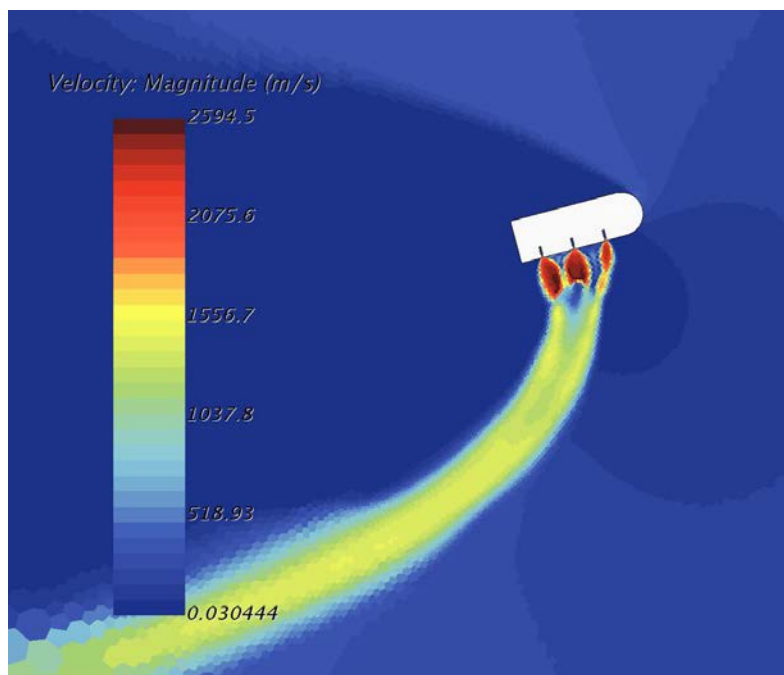


Fig. 59 $\alpha = 15^\circ$, Mach 1

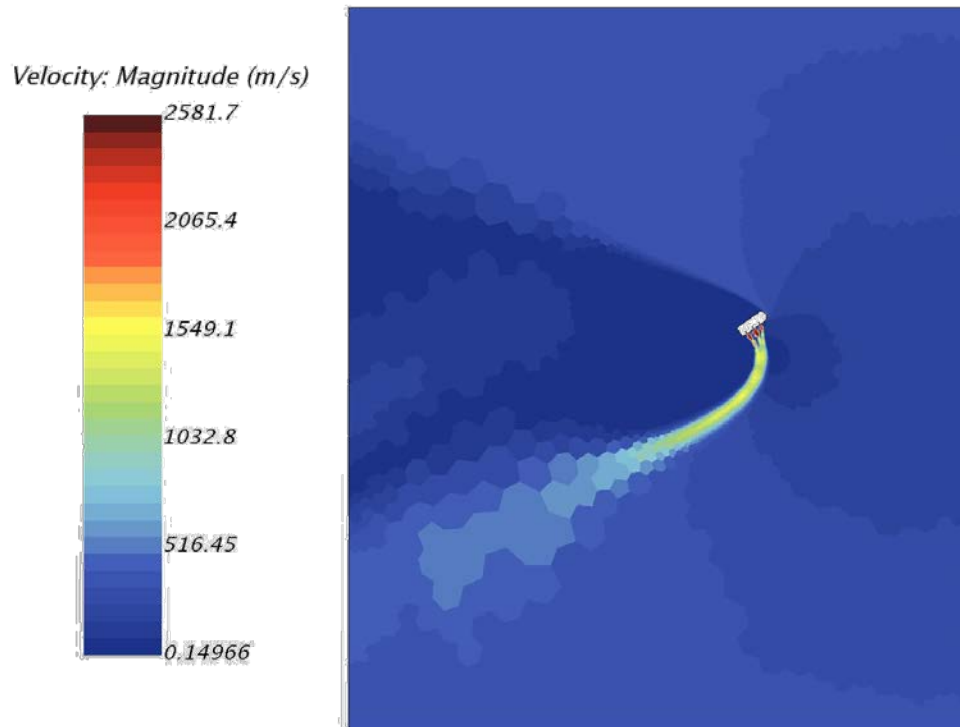


Fig. 60 $\alpha = 30^\circ$, Mach 1

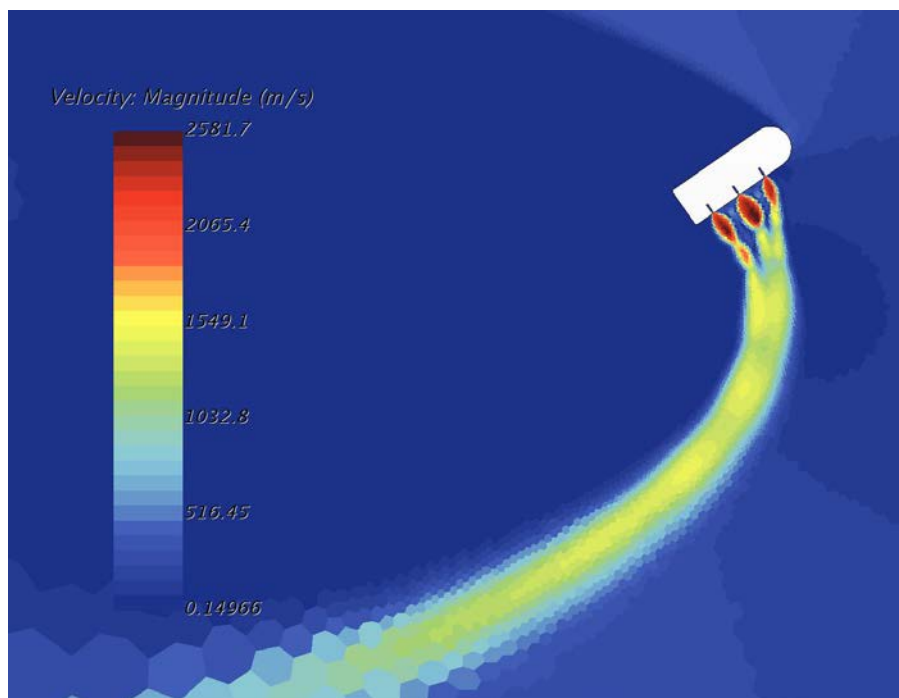


Fig. 61 $\alpha = 30^\circ$, Mach 1

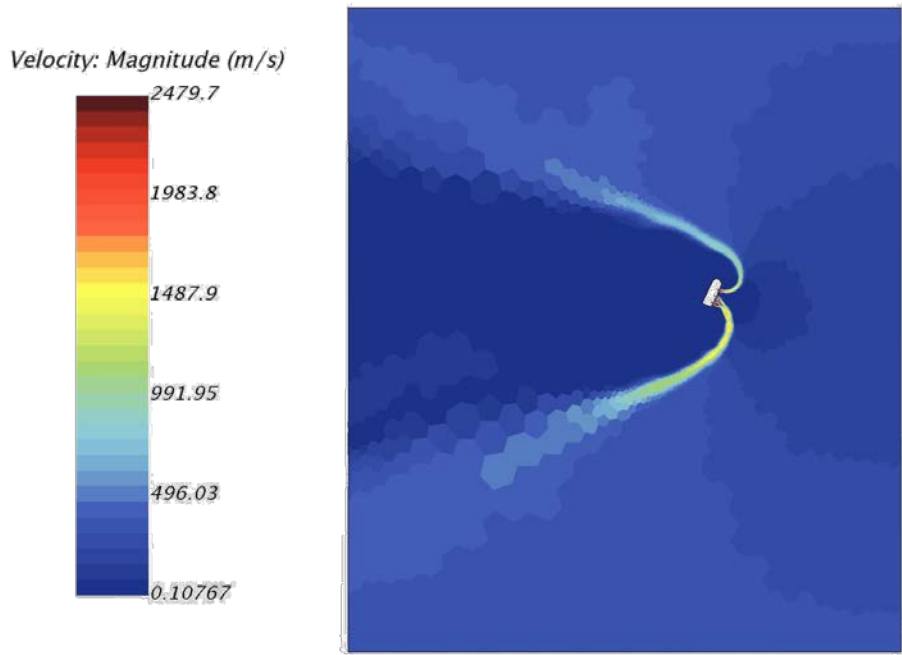


Fig. 62 $\alpha = 60^\circ$, Mach 1

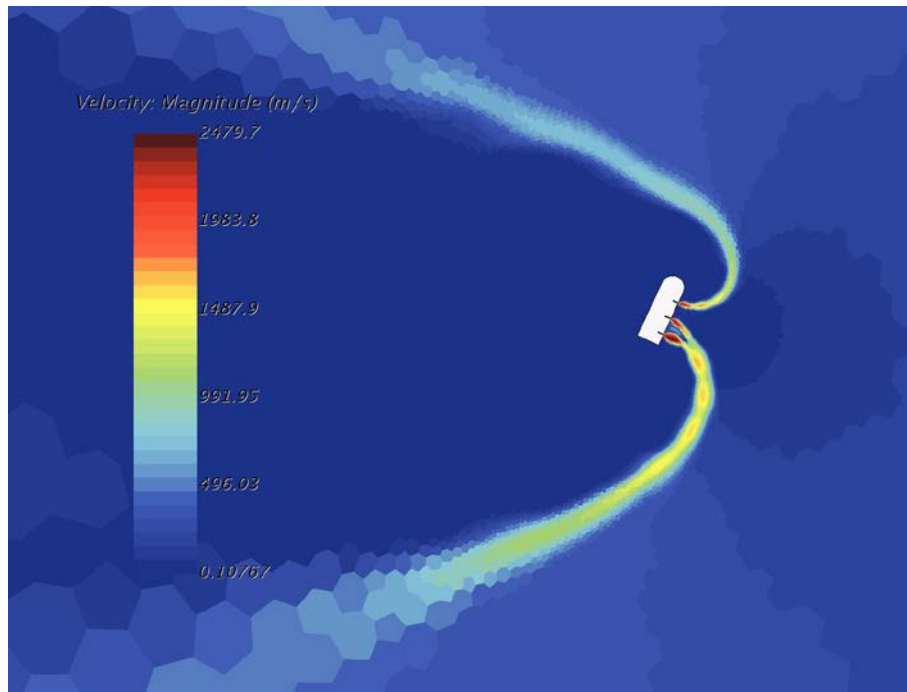


Fig. 63 $\alpha = 60^\circ$, Mach 1

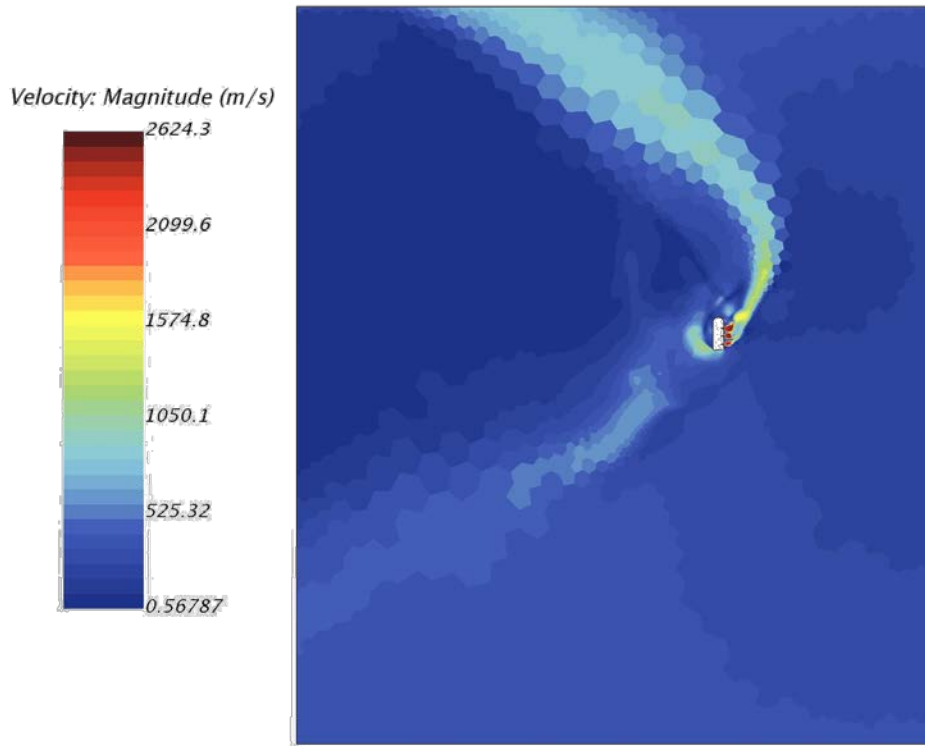


Fig. 64 $\alpha = 90^\circ$, Mach 1

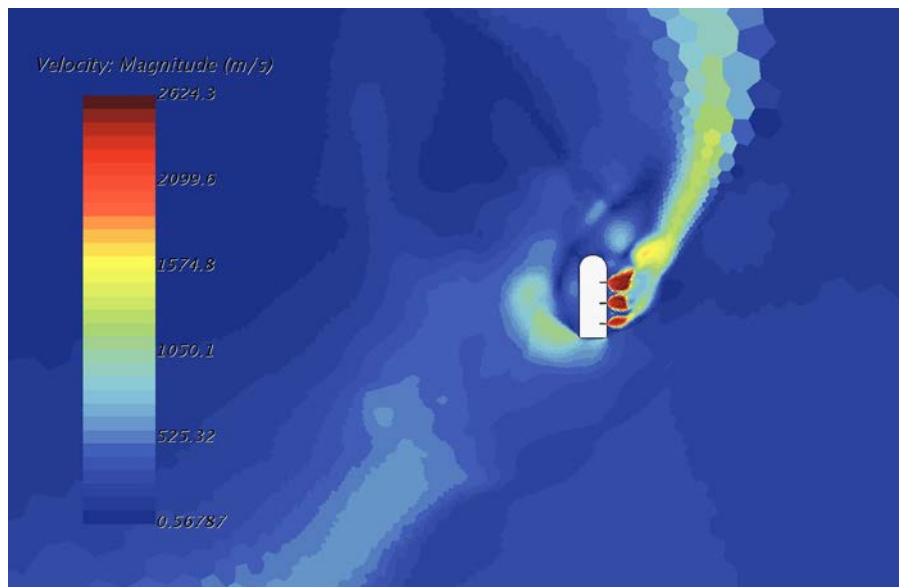


Fig. 65 $\alpha = 90^\circ$, Mach 1

Beginning at 15° AOA at Mach 1 free stream, it can be seen that all three engines are under expanded and the exhaust plume is being directed down and away from the body. The engine closest to the nose of the body is slightly over expanded, most likely due to a low pressure region after the shock wave. This continues as the AOA is increased to 30° . When the AOA reaches 60° the front engines exhaust plume is now being directed over the nose of the body and all three engines are closer to performing optimally. Finally when the flow reaches 90° the exhaust plume as reversed from

the 15° and is now going up around the nose of the body. Since the free stream flow is slow the shock wave does not have a large effect on the exhaust plume and its interaction with the elipsled.

9.1.2 Mach 2 Simulations

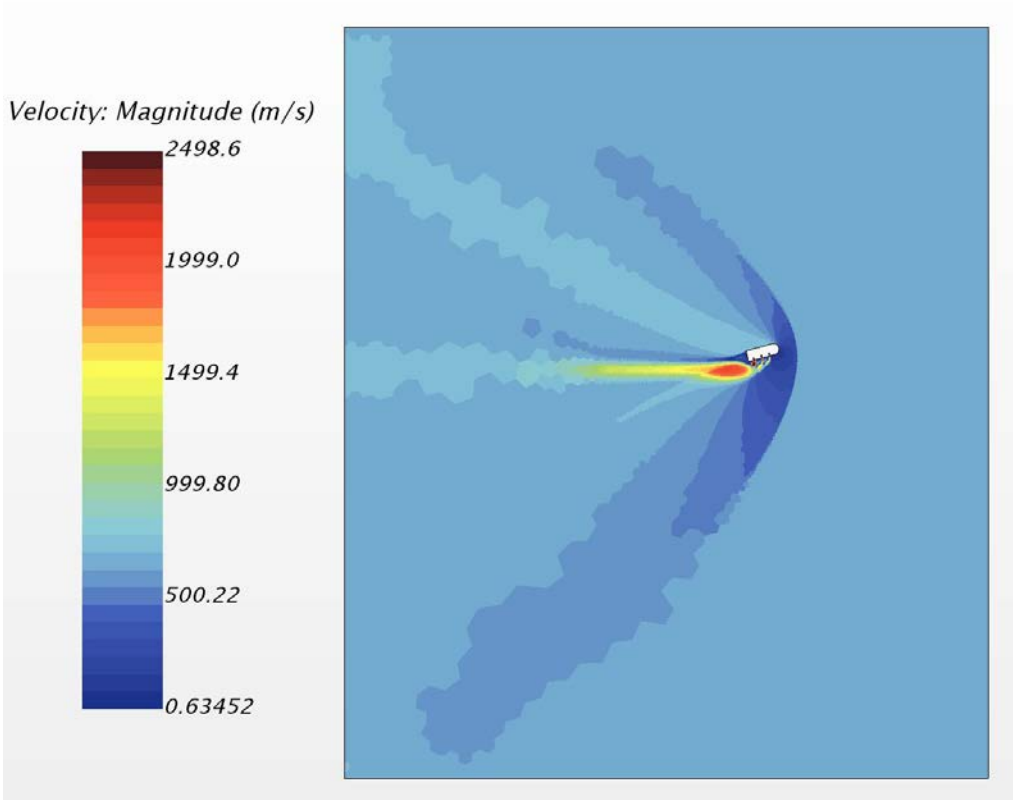


Fig. 66 $\alpha = 15^\circ$, Mach 2

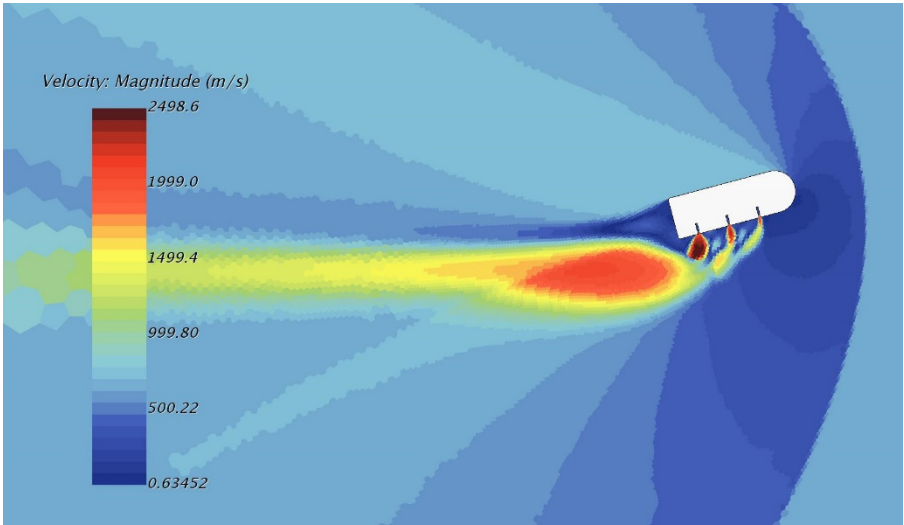


Fig. 67 $\alpha = 15^\circ$, Mach 2

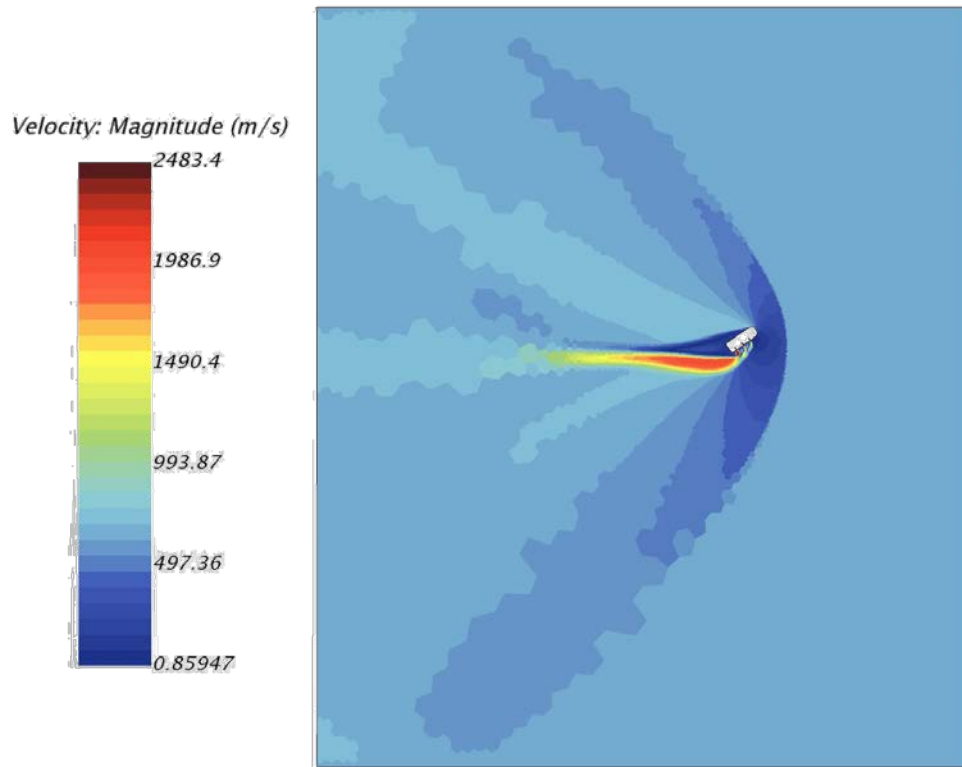


Fig. 68 $\alpha = 30^\circ$, Mach 2

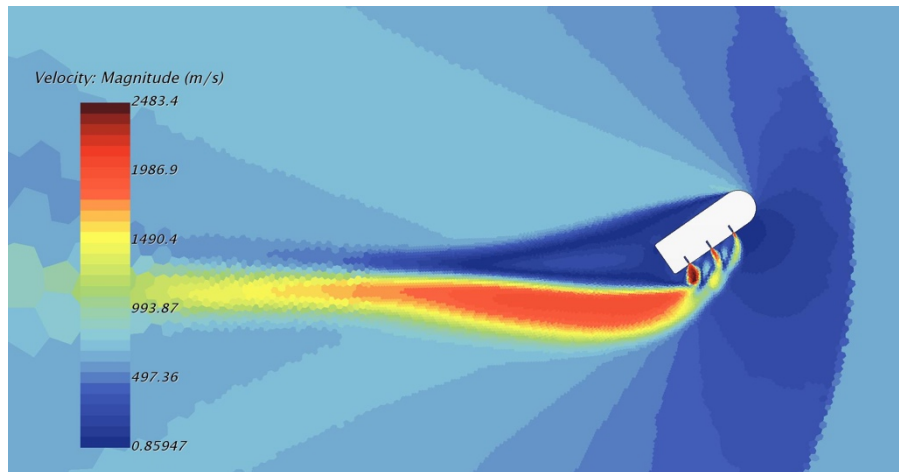


Fig. 69 $\alpha = 30^\circ$, Mach 2

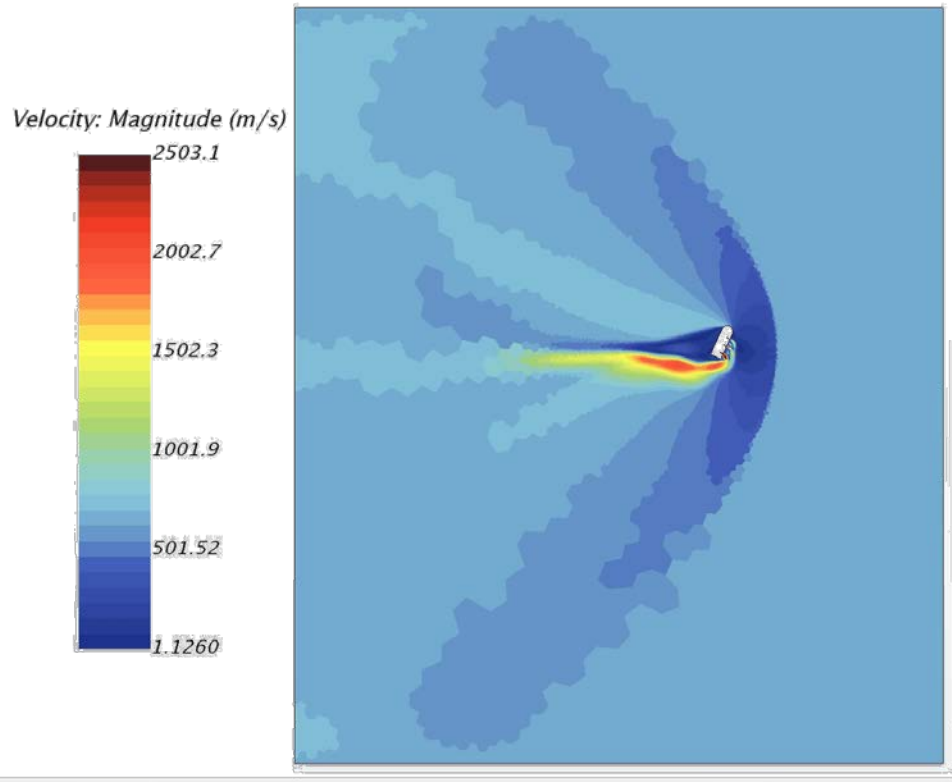


Fig. 70 $\alpha = 60^\circ$, Mach 2

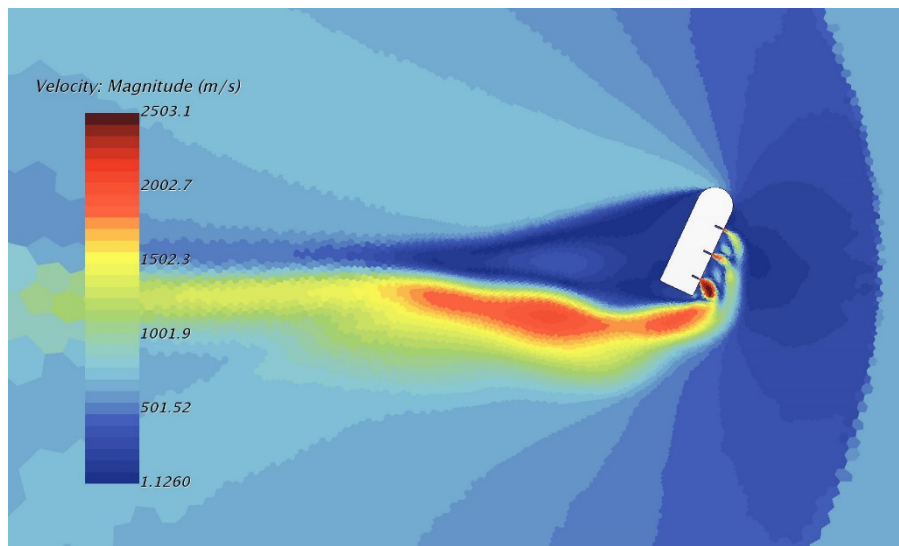


Fig. 71 $\alpha = 60^\circ$, Mach 2

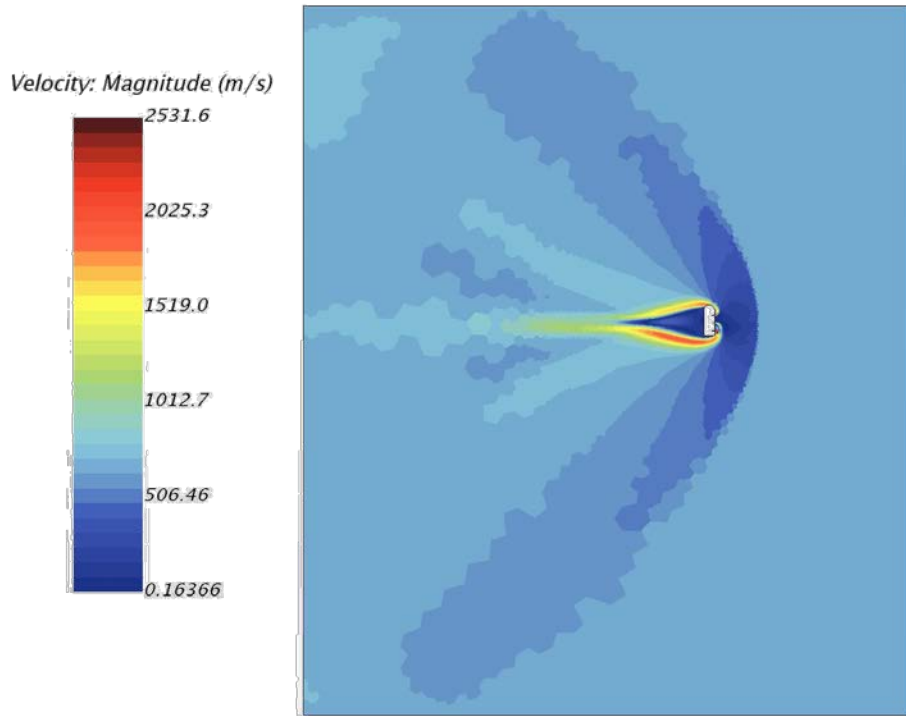


Fig. 72 $\alpha = 90^\circ$, Mach 2

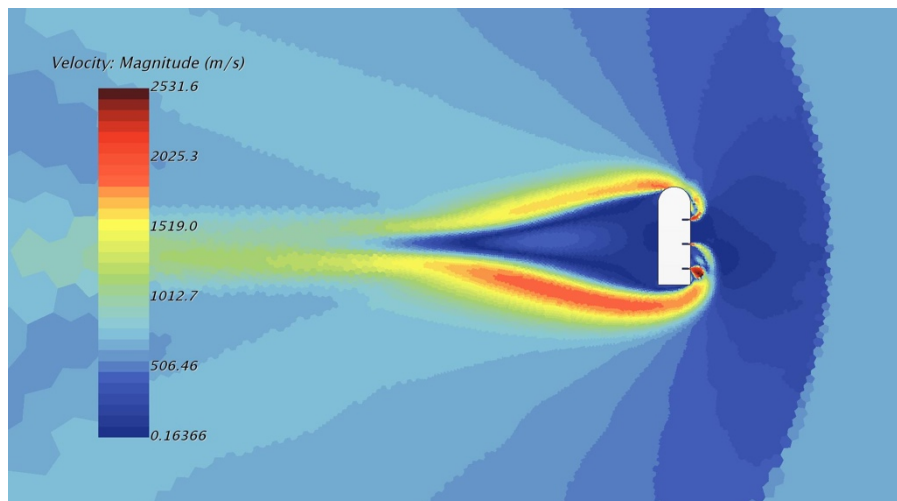


Fig. 73 $\alpha = 90^\circ$, Mach 2

As the free stream velocity is increased to Mach 2, a clear bow shock wave is formed at the nose of the body. Compared to the Mach 1 simulations, the shock wave effects the exhaust plume much more. Looking at the 15° AOA the exhaust plume on each engine is different. The rear engine is under expanded, the center engine is almost ideally expanded and the front nozzle closest to the nose is over expanded. The exhaust plume does however flow out and away from the body. The same flow characteristic can be seen on both the 30° and the 60° AOA simulations. However when the AOA is increased to 90° the shock wave separates the exhaust plume and splits the flow around the rear and nose of the elipsled.

9.1.3 Mach 2.5 Simulations

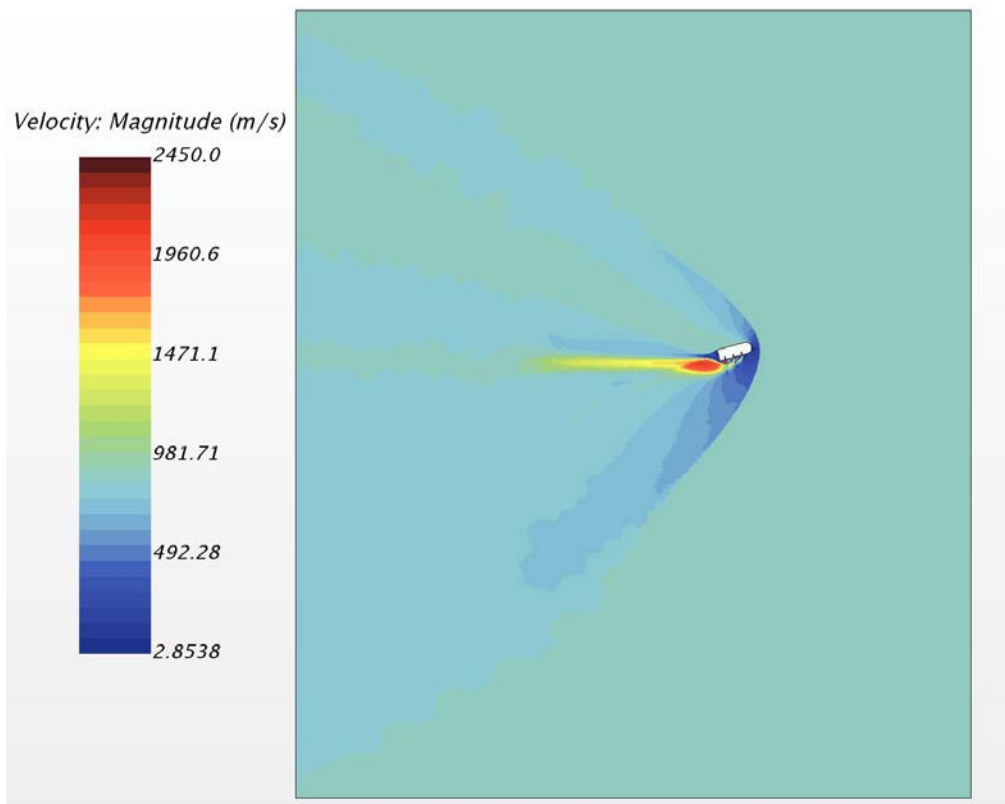


Fig. 74 $\alpha = 15^\circ$, Mach 2.5

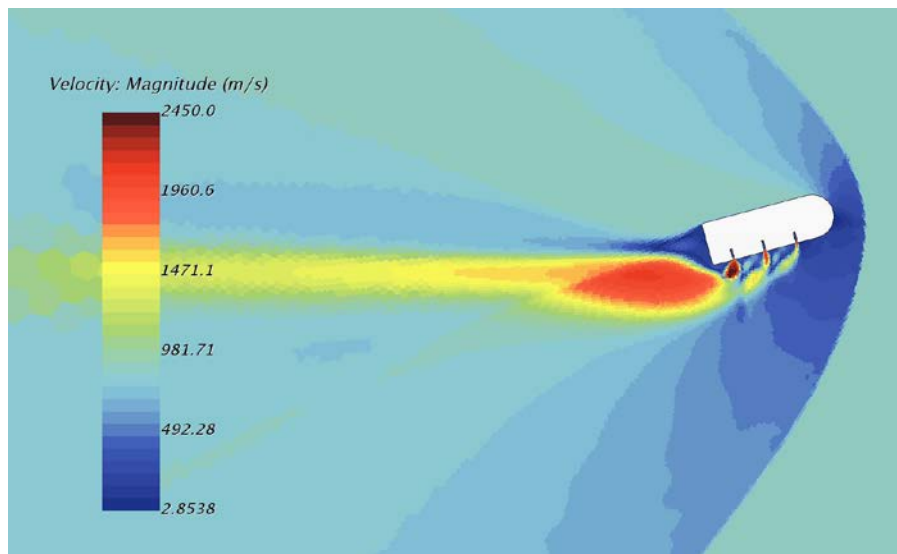


Fig. 75 $\alpha = 15^\circ$, Mach 2.5

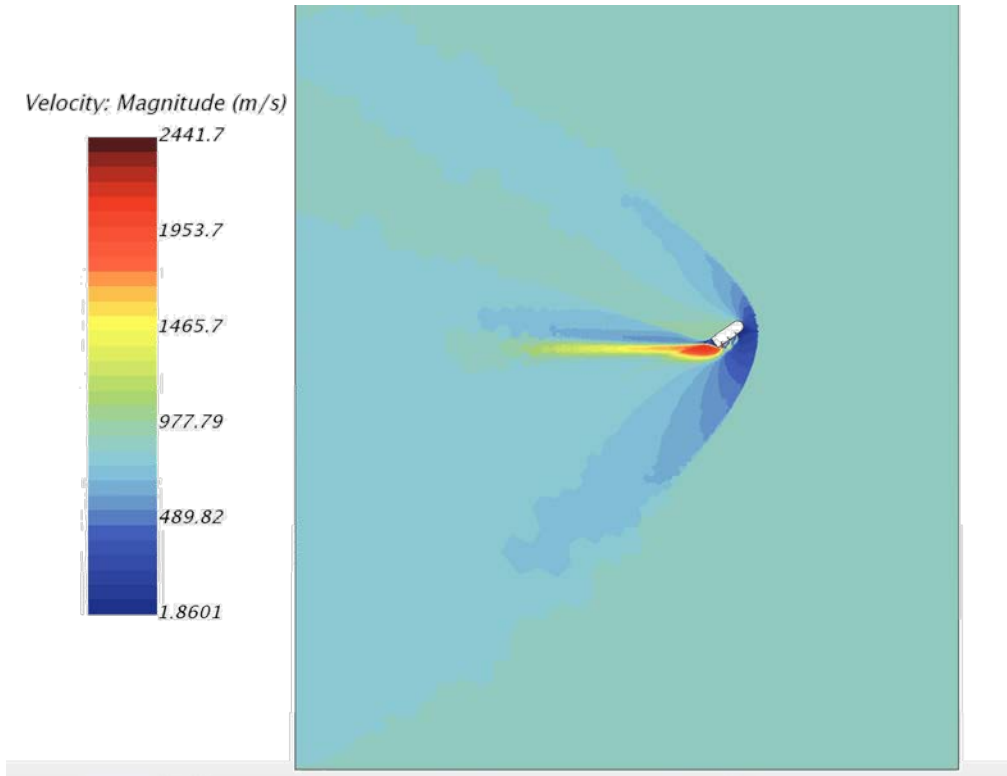


Fig. 76 $\alpha = 30^\circ$, Mach 2.5

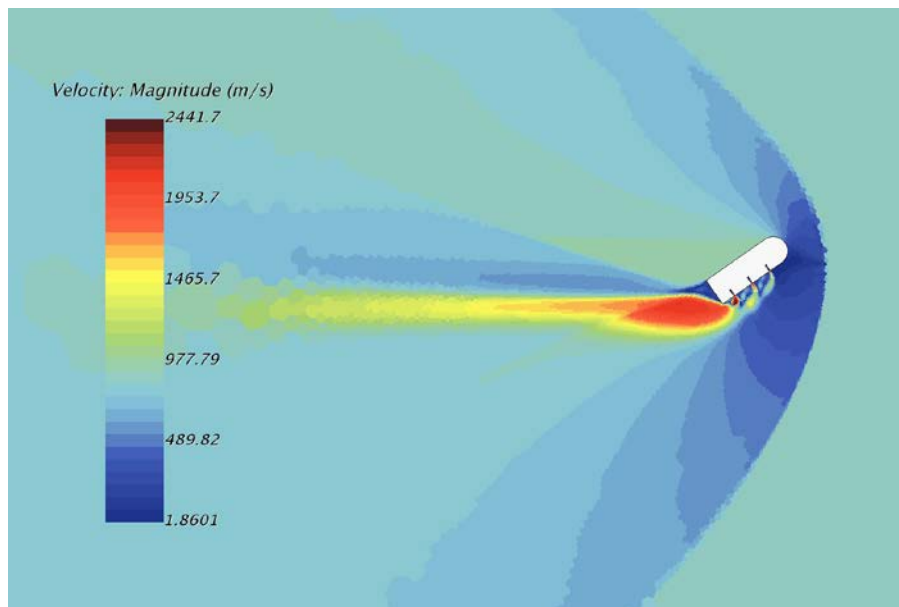


Fig. 77 $\alpha = 30^\circ$, Mach 2.5

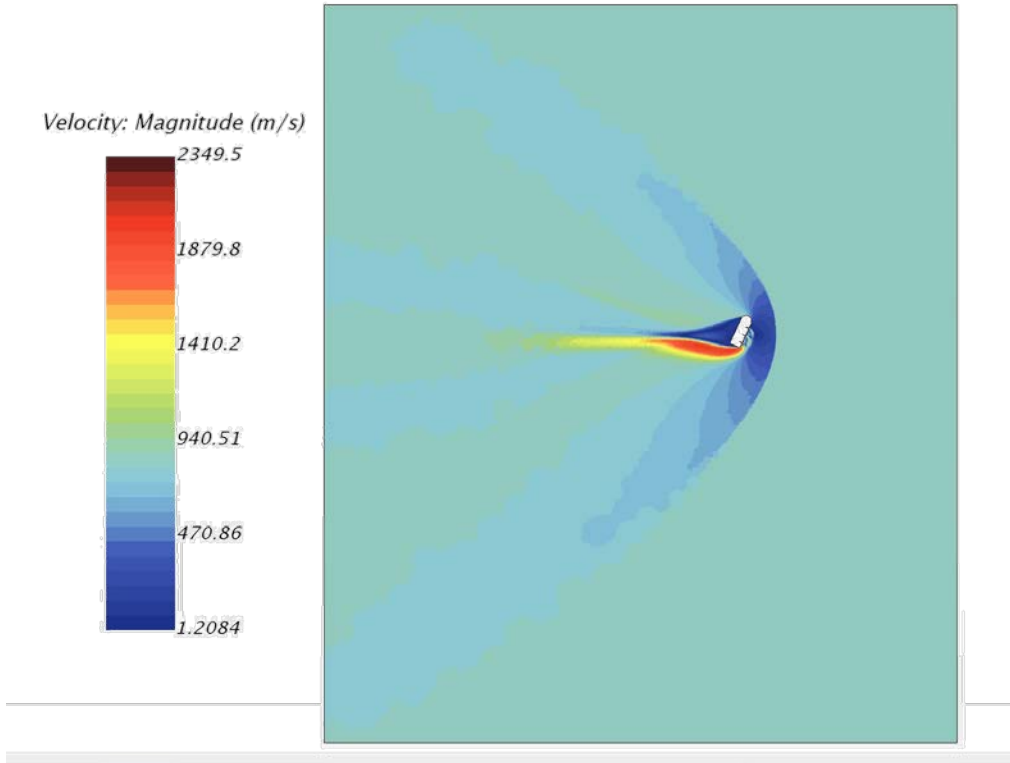


Fig. 78 $\alpha = 60^\circ$, Mach 2.5

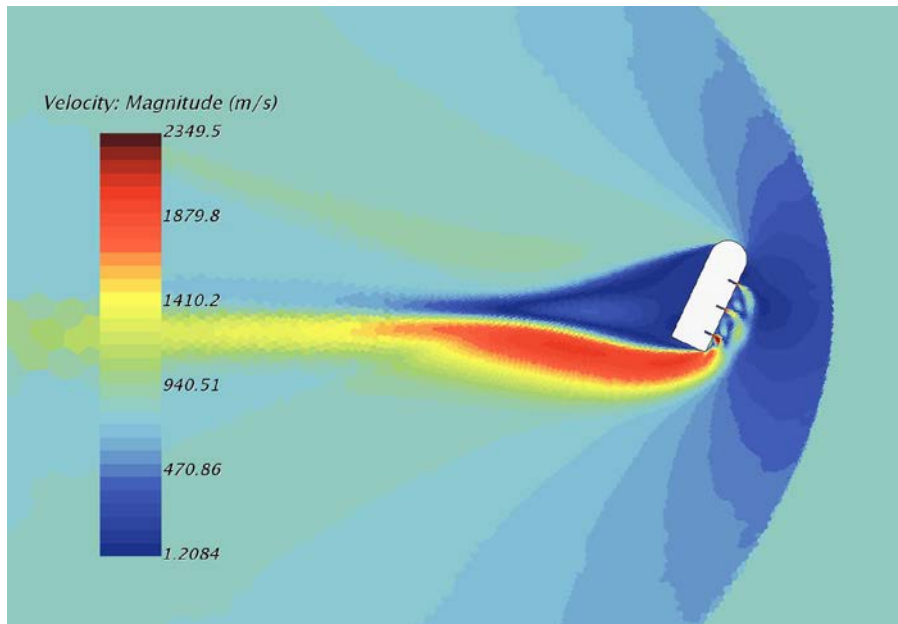


Fig. 79 $\alpha = 60^\circ$, Mach 2.5

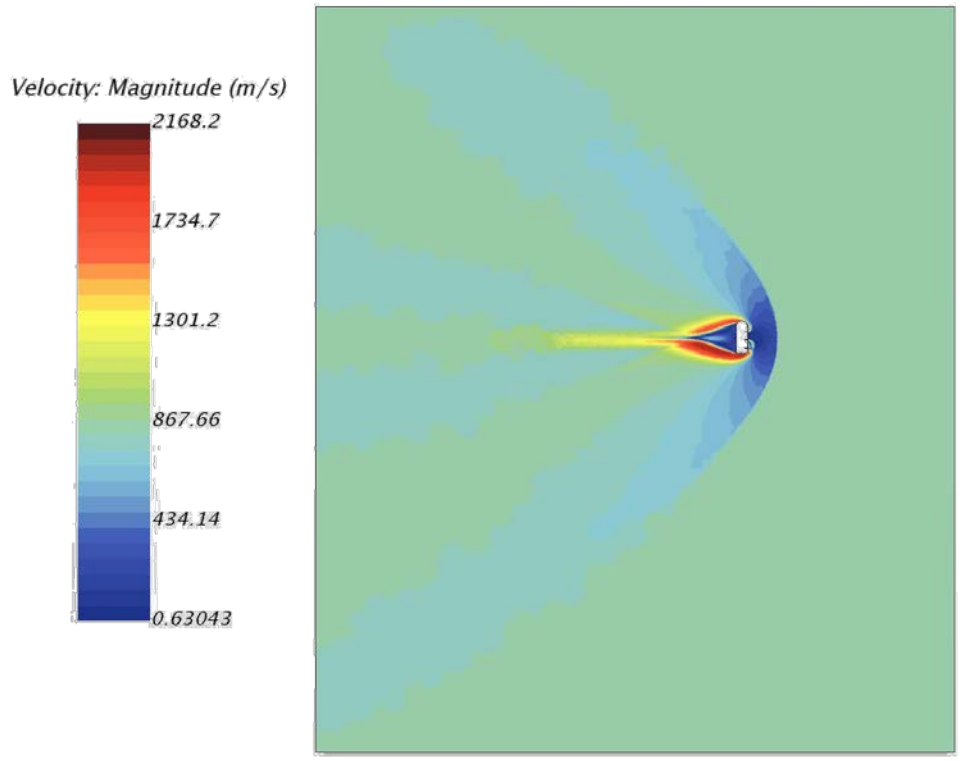


Fig. 80 $\alpha = 90^\circ$, Mach 2.5

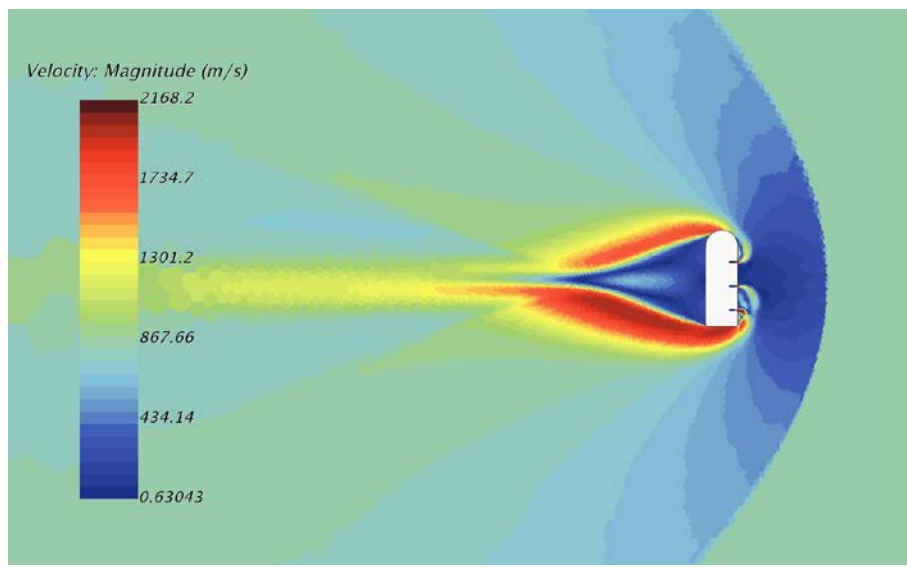


Fig. 81 $\alpha = 90^\circ$, Mach 2.5

9.1.4 Mach 3 Simulations

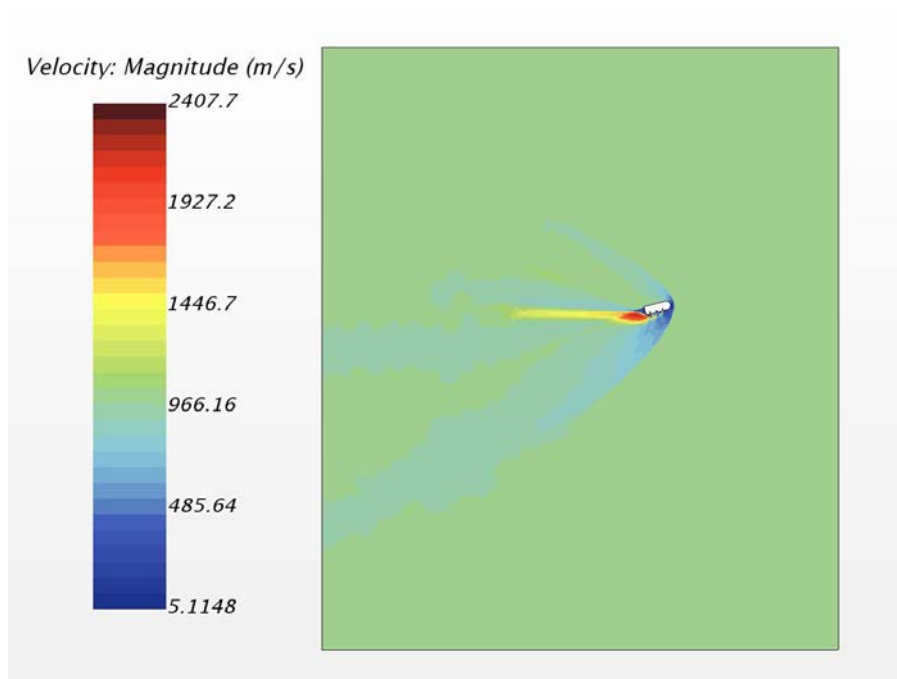


Fig. 82 $\alpha = 15^\circ$, Mach 3

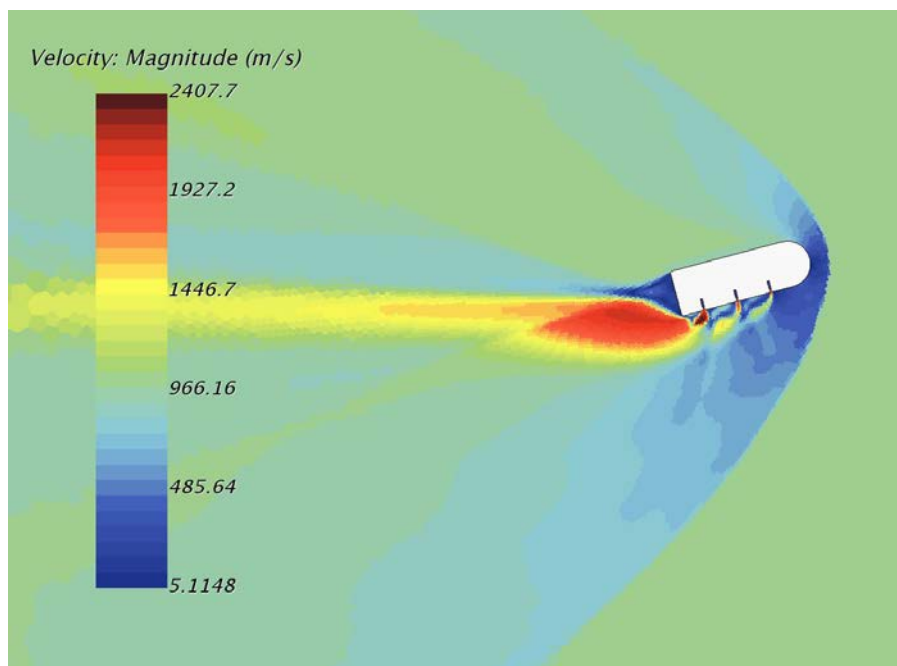


Fig. 83 $\alpha = 15^\circ$, Mach 3

Velocity: Magnitude (m/s)

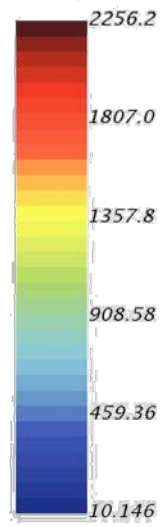


Fig. 84 $\alpha = 30^\circ$, Mach 3

Velocity: Magnitude (m/s)

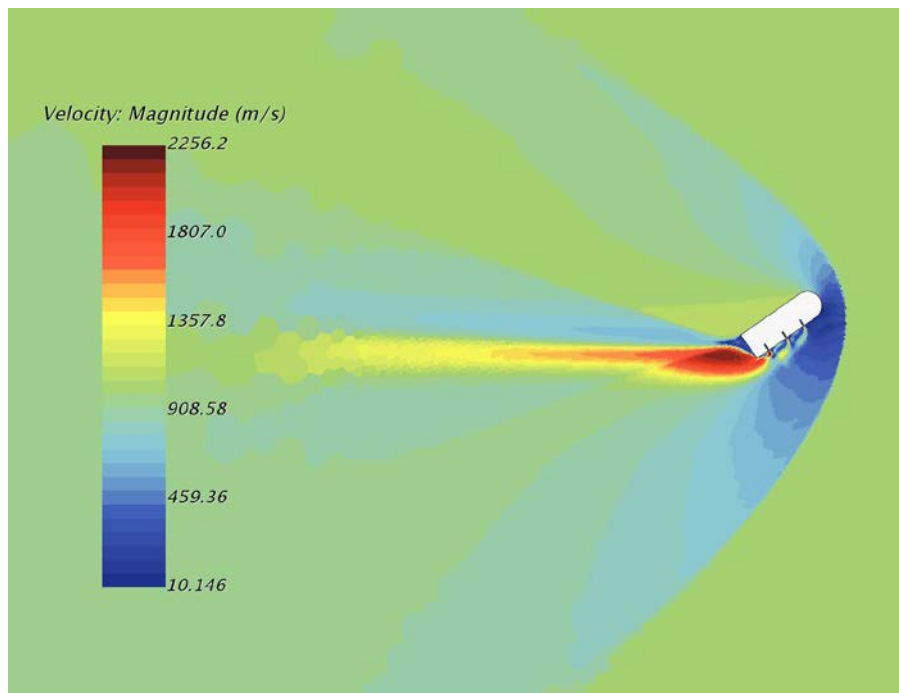
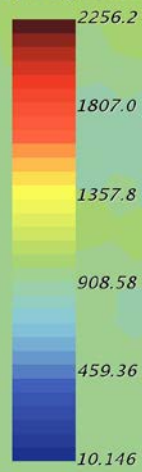


Fig. 85 $\alpha = 30^\circ$, Mach 3

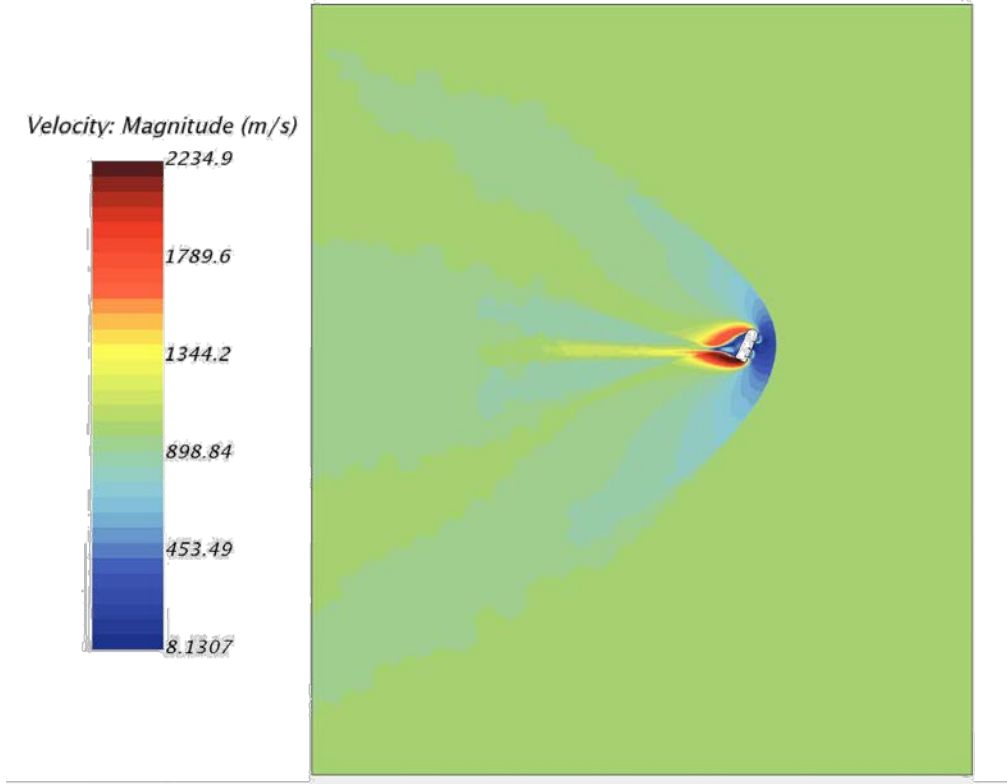


Fig. 86 $\alpha = 60^\circ$, Mach 3

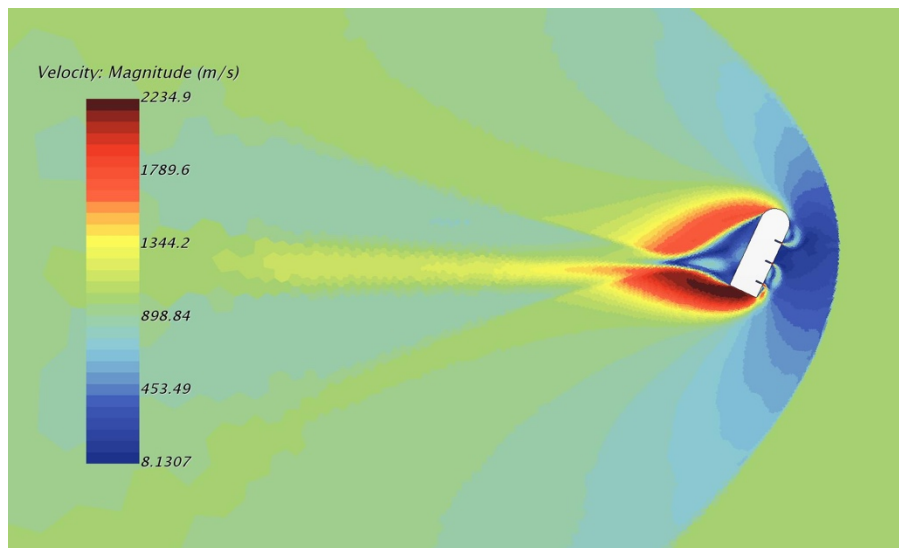


Fig. 87 $\alpha = 60^\circ$, Mach 3

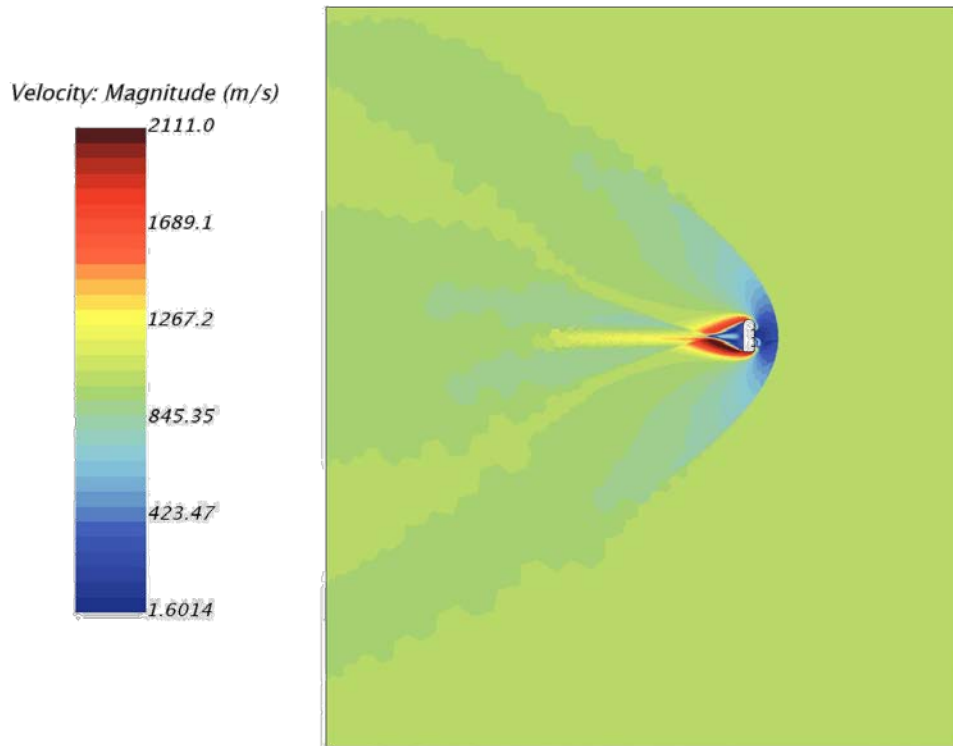


Fig. 88 $\alpha = 90^\circ$, Mach 3

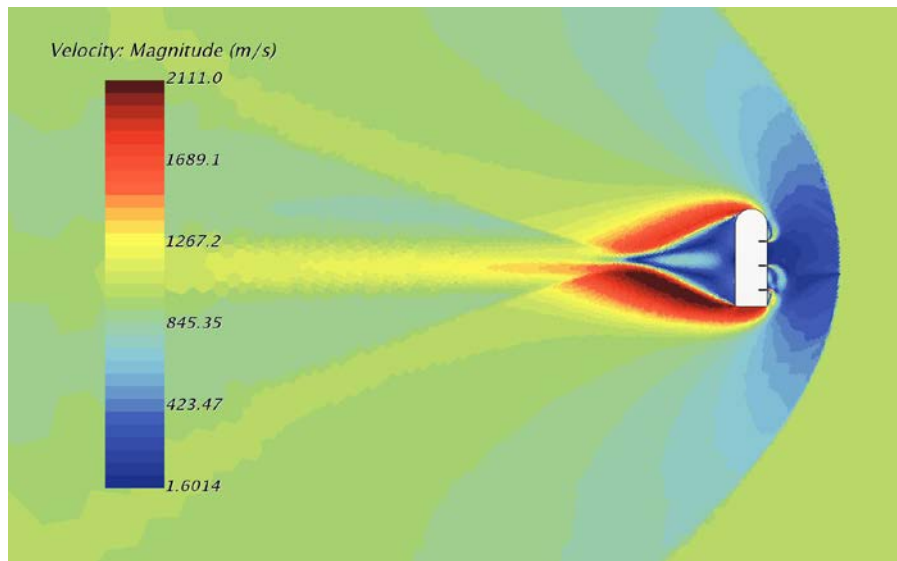


Fig. 89 $\alpha = 90^\circ$, Mach 3

Similar to the Mach 2.5 results, at an AOA of 15° , the front and center engines exhaust is over expanded and the rear engines exhaust it slightly under expanded. This continues with the elipsled at 30° AOA, however when the elipsled increases its AOA to 60° , exhaust from the front engine flow past the nose of the body, instead down along the bottom of the elipsled like in lower Mach number simulations. The trends then continues with the 90° with the exhaust flowing over the nose and the rear of the elipsled.

9.1.5 Mach 4 Simulations

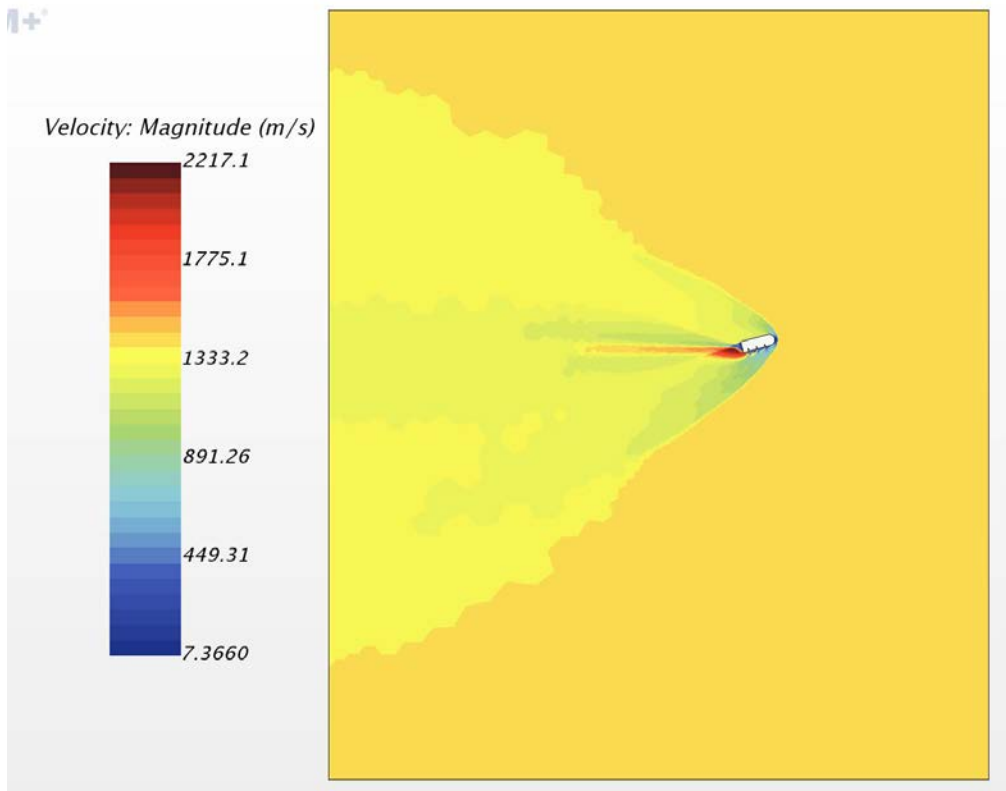


Fig. 90 $\alpha = 15^\circ$, Mach 4

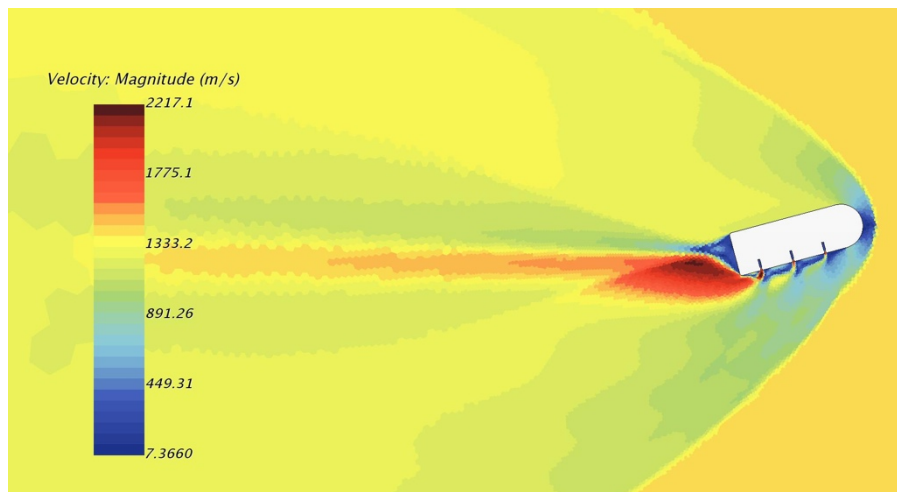


Fig. 91 $\alpha = 15^\circ$, Mach 4

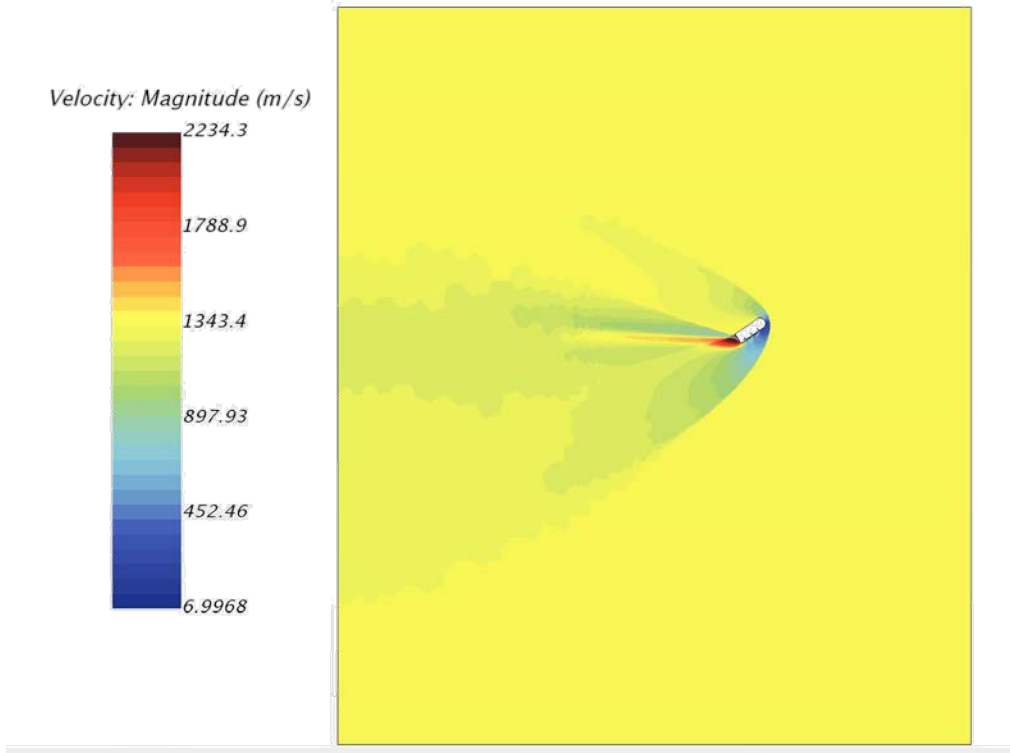


Fig. 92 $\alpha = 30^\circ$, Mach 4

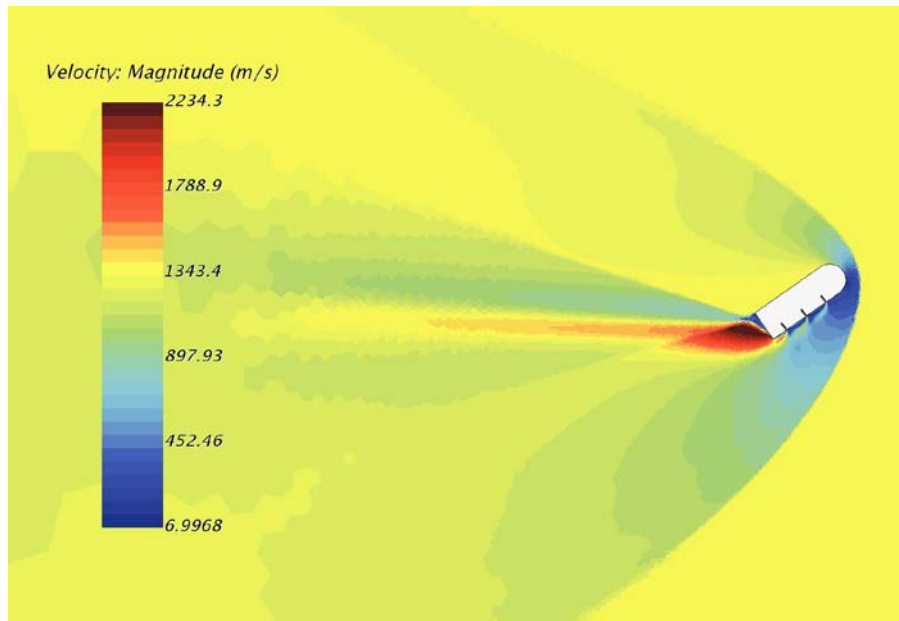


Fig. 93 $\alpha = 30^\circ$, Mach 4

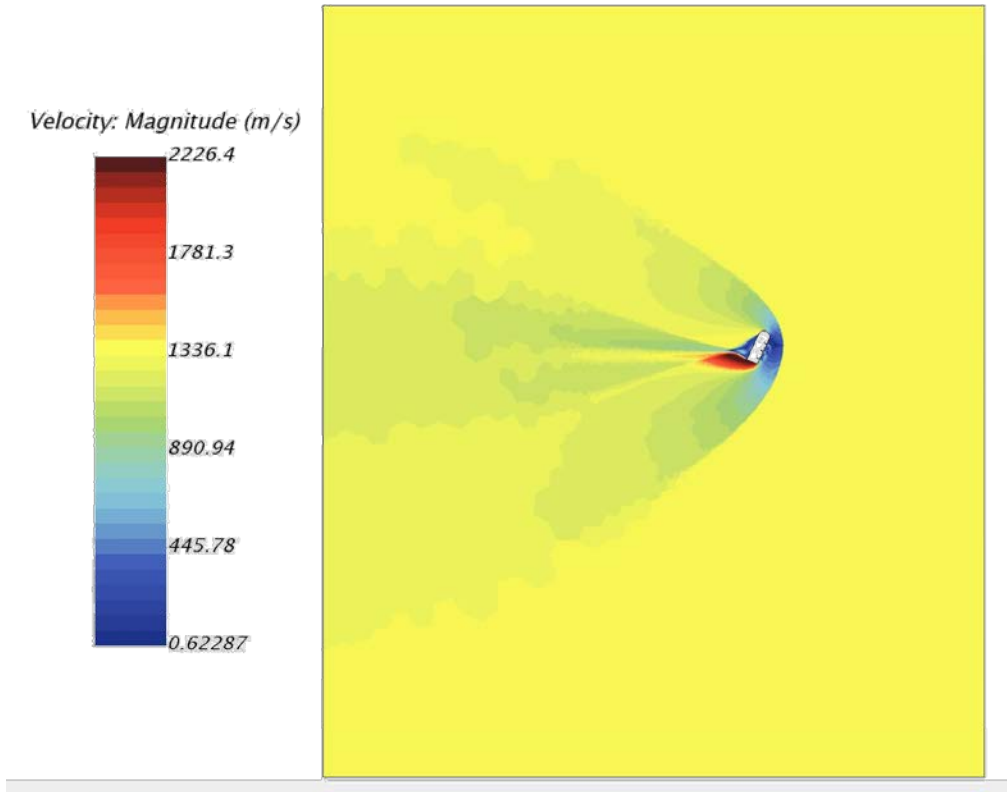


Fig. 94 $\alpha = 60^\circ$, Mach 4

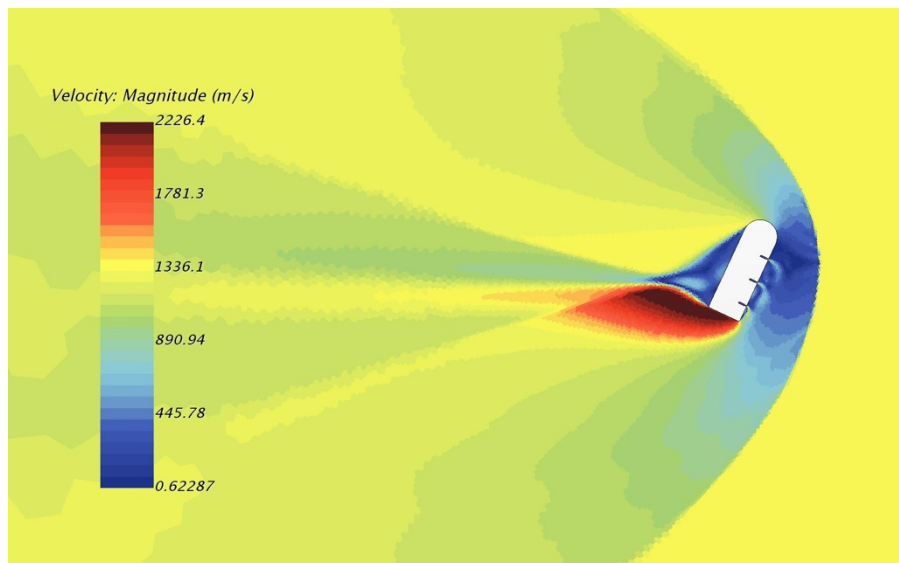


Fig. 95 $\alpha = 60^\circ$, Mach 4

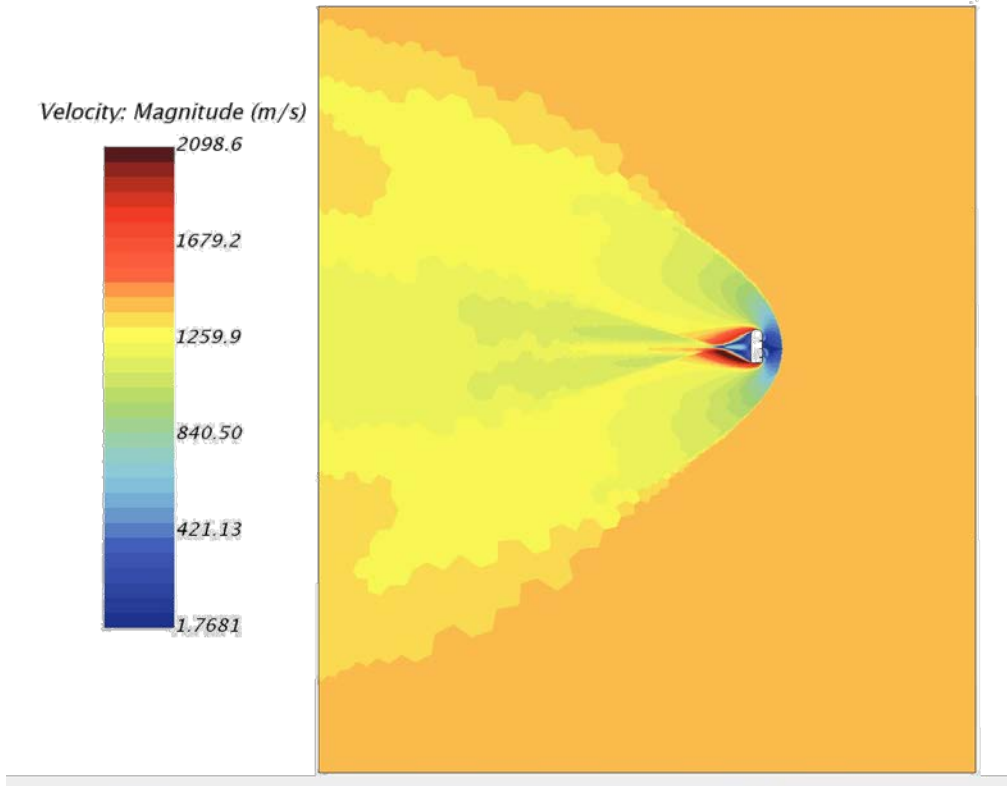


Fig. 96 $\alpha = 90^\circ$, Mach 4

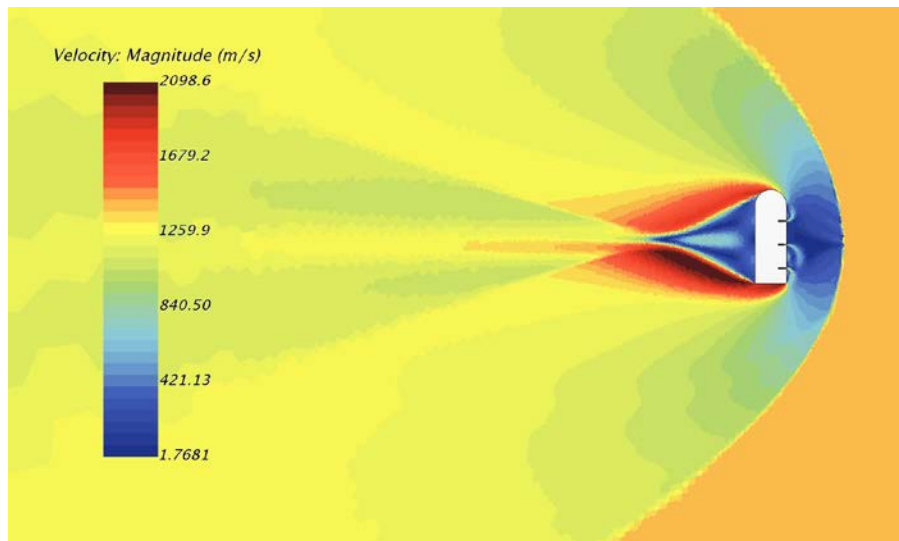


Fig. 97 $\alpha = 90^\circ$, Mach 4

Mach 4 for all AOA resulted in all the engines being grossly over expanded. This is most likely due to a shock wave forming in or near the nozzle. This results in almost no exhaust from the front and center engine and the rear engine's exhaust is pulled to the rear of the elipsled. However the 90° AOA, the front engines exhaust it pulled over the nose of the vehicle, similar to the lower Mach number results.

9.2 Mesh Refinement

Mesh refinement analysis was conducted on the Mach 2.5 simulations and cell count was increased from 50,000 cells to 250,000 cells. The analysis showed that the flow characteristics did not change, only the resolution of the data was increased. This can be seen when comparing the refined mesh figures to the normal figures seen above.

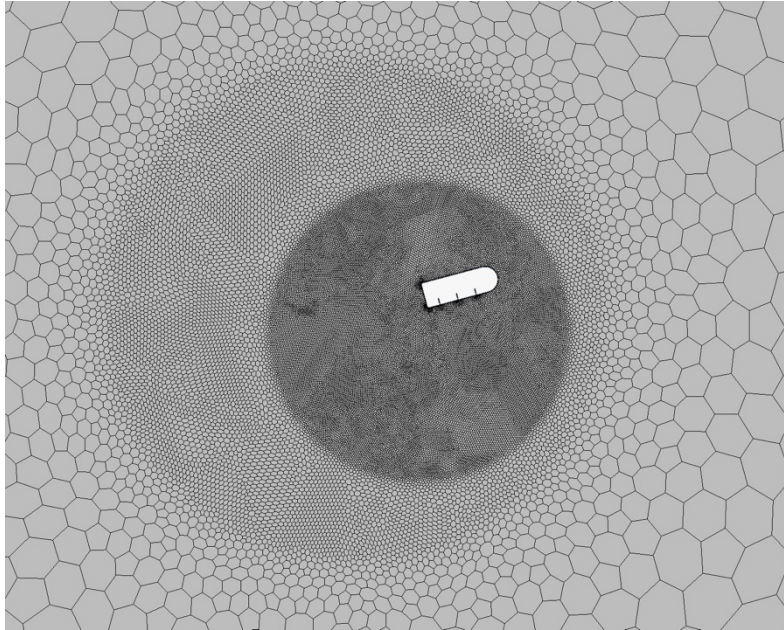


Fig. 98 50,000 Cell Count Mesh

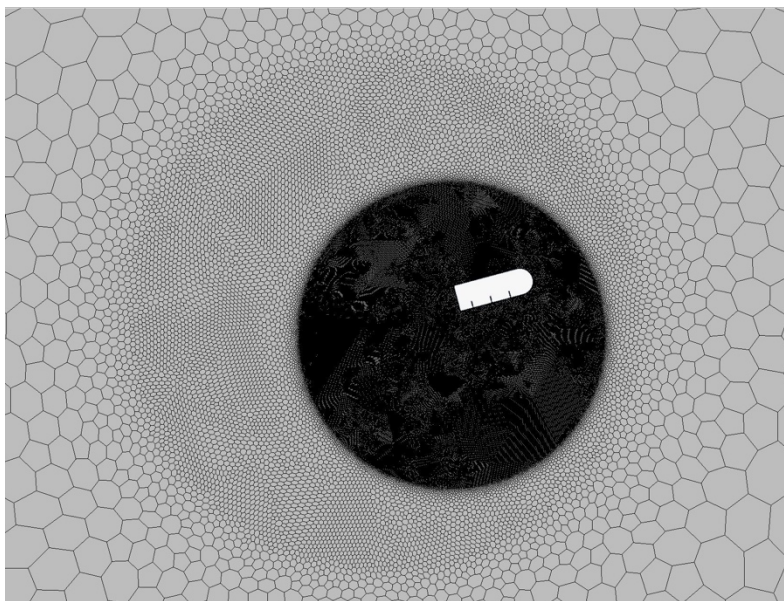


Fig. 99 250,000 Cell Count Mesh

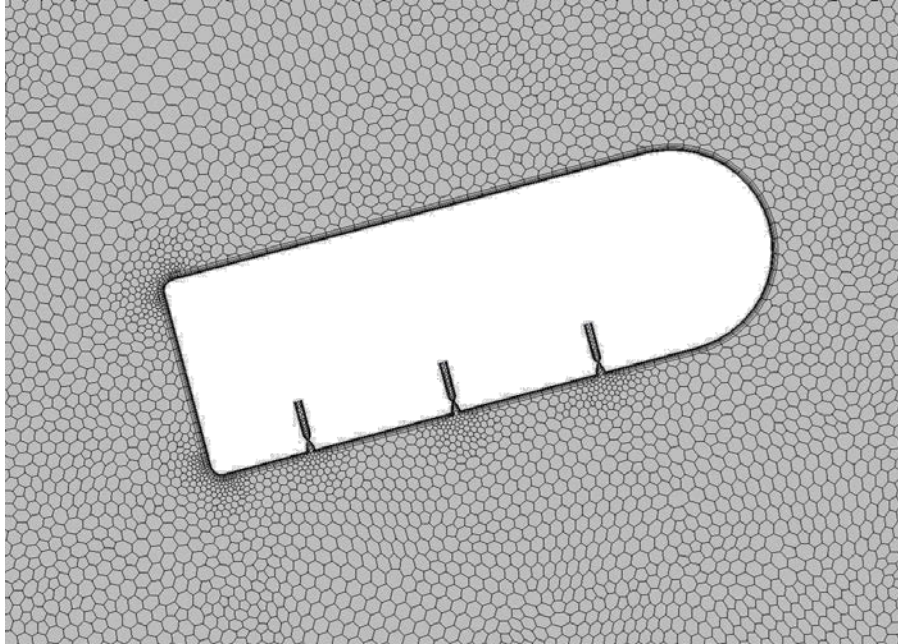


Fig. 100 50,000 Cell Count Mesh Zoomed

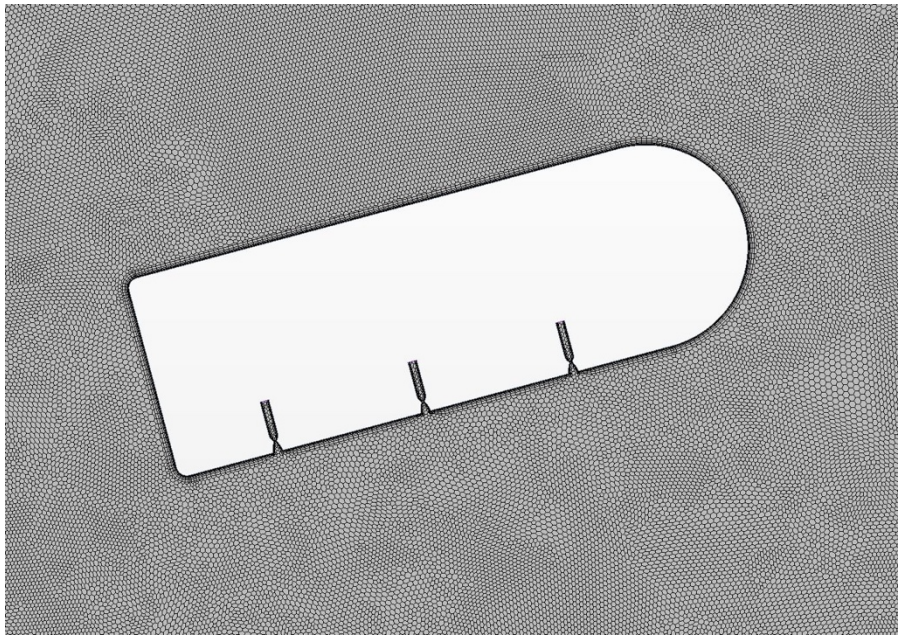


Fig. 101 250,000 Cell Count Mesh Zoomed

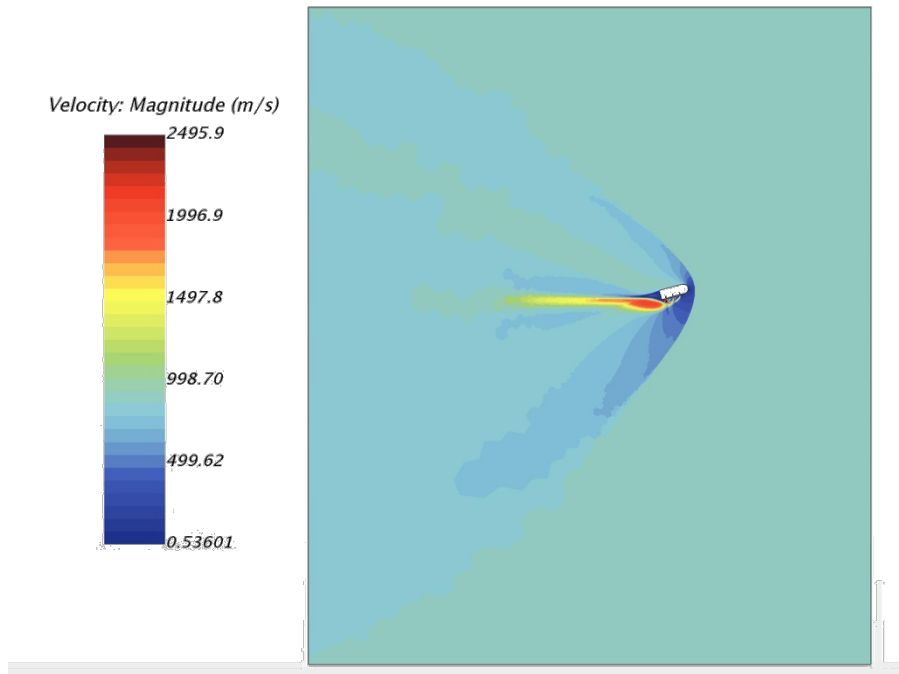


Fig. 102 $\alpha = 15^\circ$, Mach 2.5, Refined Mesh

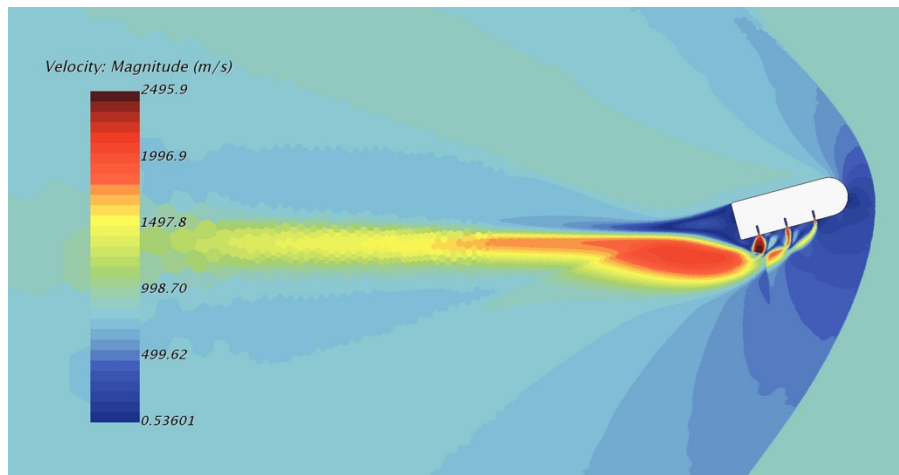


Fig. 103 $\alpha = 15^\circ$, Mach 2.5, Refined Mesh

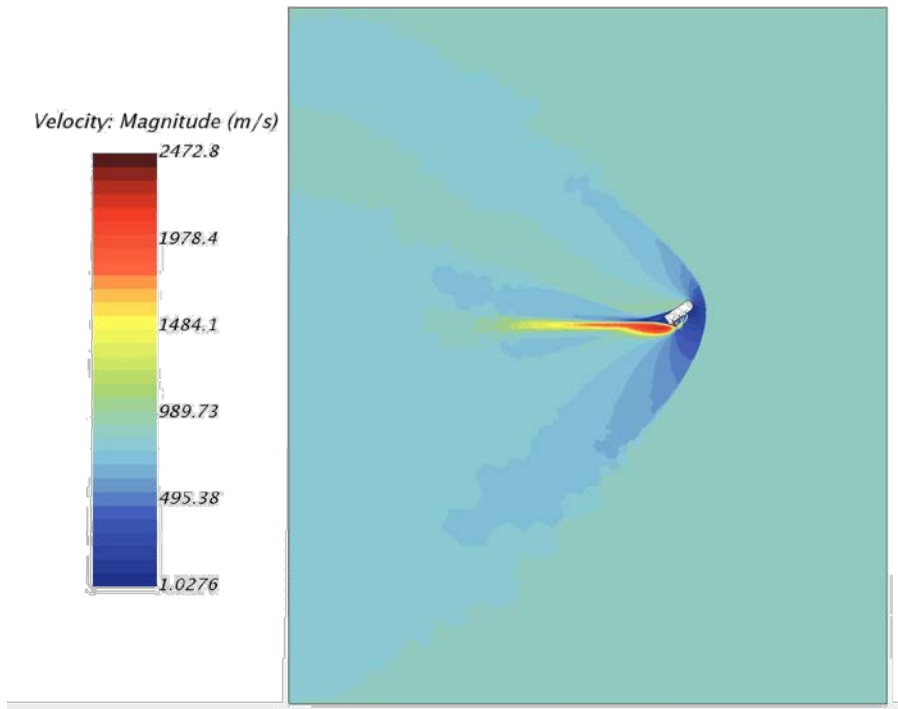


Fig. 104 $\alpha = 30^\circ$, Mach 2.5, Refined Mesh

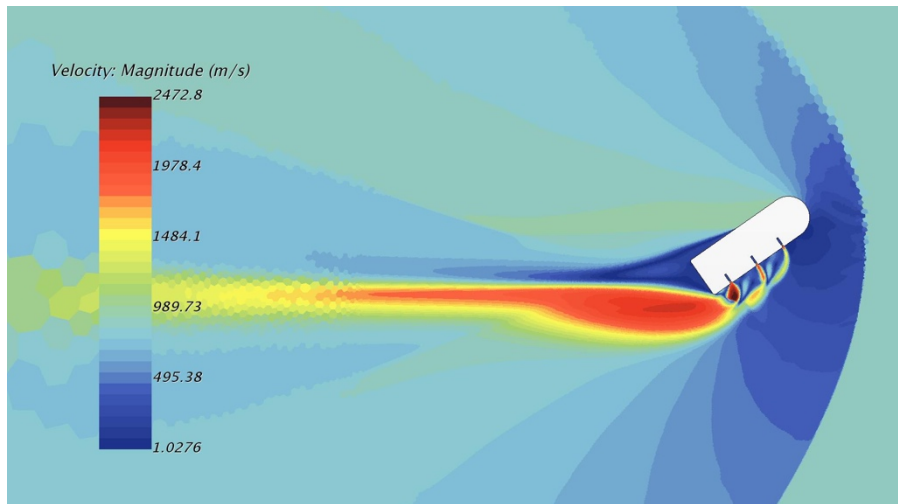


Fig. 105 $\alpha = 30^\circ$, Mach 2.5, Refined Mesh

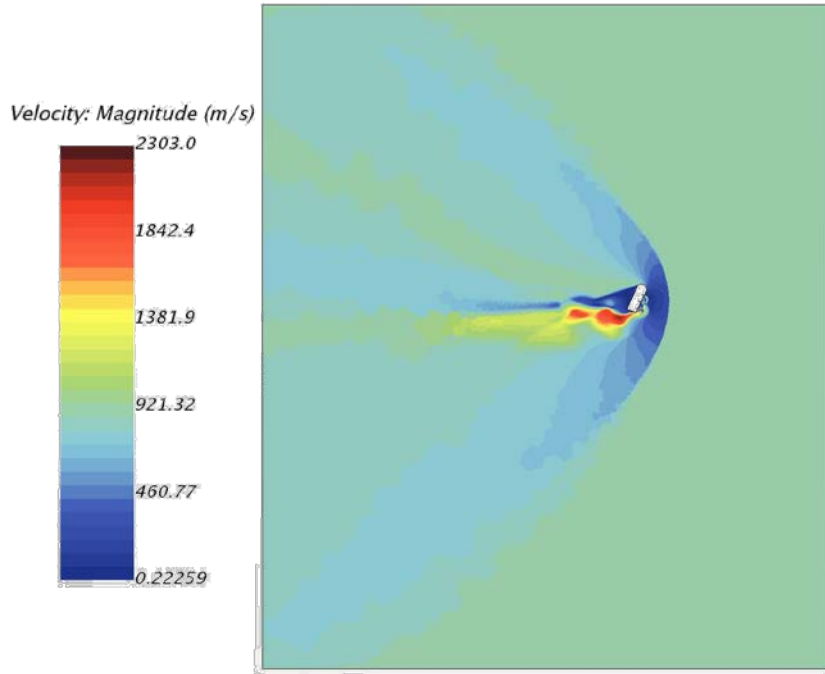


Fig. 106 $\alpha = 60^\circ$, Mach 2.5, Refined Mesh

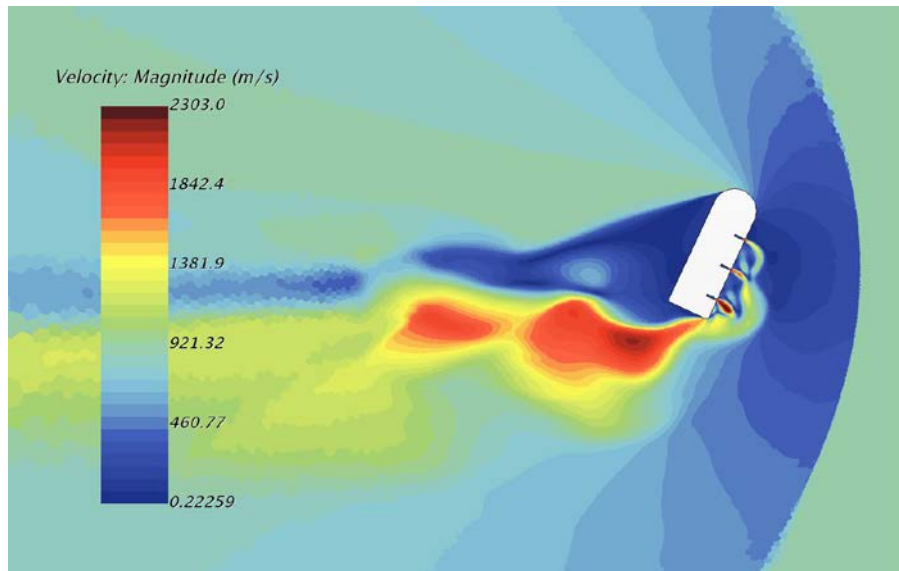


Fig. 107 $\alpha = 60^\circ$, Mach 2.5, Refined Mesh

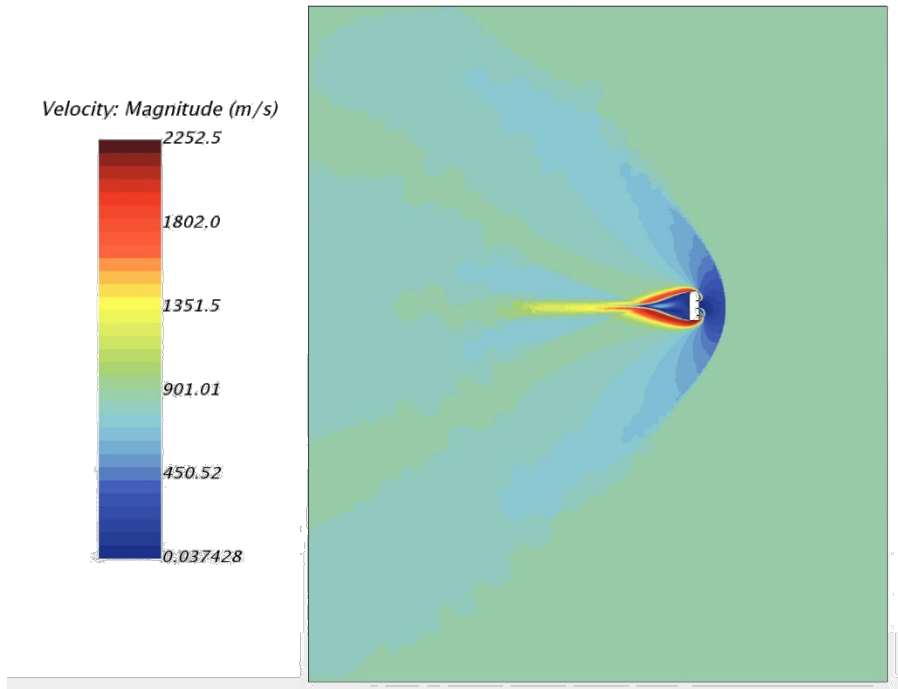


Fig. 108 $\alpha = 90^\circ$, Mach 2.5, Refined Mesh

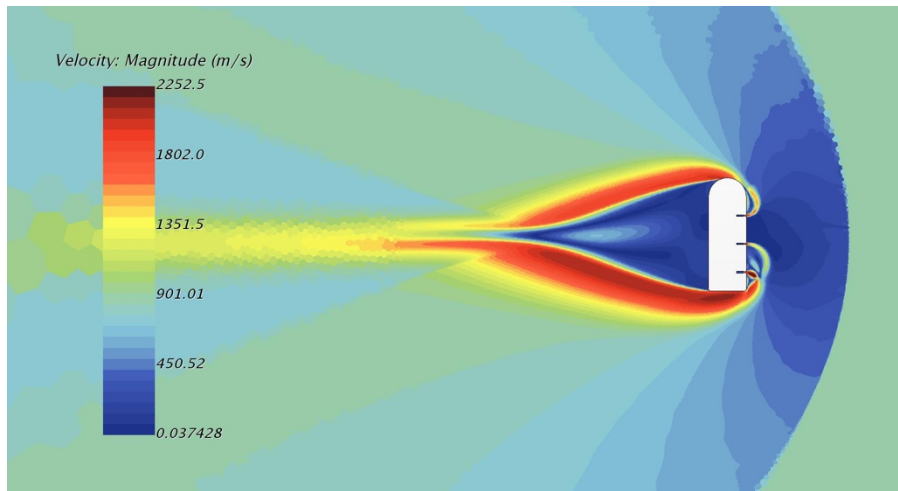


Fig. 109 $\alpha = 90^\circ$, Mach 2.5, Refined Mesh

10. Future Work

The results gathered were not as precise as hoped. Increasing cell count and adjusting physics models could yield more precise and accurate results. Further engine design could also result in a more stable elipsled designs. Current design has all the nozzles being the same, but adjust mass flow and location of engines on the body could results in a more stable flow around the elipsled. A greater parametric study should be conducted and see the benefits of adjust free steam velocities, engine location, engine mass flow, angle of attack and elisplesd geometry changes. A final 3D simulation for the most promising result should be conducted as well to view the total flow around the vehicle, not just a 2D slice.

11. Summary

Overall it can be seen that the designed single nozzle matches the flow characteristics of Georgia Institute of Technologies nozzle engine design, which is based off of a NASA nozzle engine design. The long jet flow terminates into a weak bow shock that can be seen extending back towards the nozzle. When using this nozzle for the elipsled with nozzle normal to the body, the flow can be seen to extend under the body and flow back towards the rear of the body. When comparing the flow from each nozzle, the nozzle farthest to the rear of the body, the exhaust is under expanded due to a pressure drop from the flow of the first two nozzles. To fix this, each nozzle could be designed for different exit pressures for ideal expansion. From the results gathered, a configuration with the current nozzle engine parameters and free stream velocity of Mach 2, had the best flow characteristics and perceived to be the most stable of all simulations. Pressure and temperature figures for all simulations can be found in Appendix A.

References

- [1] A. Korzun, G. Dubos, C. Iwata, B. Stahl, J. Quicksall, "A concept for the entry, descent, and landing of high-mass payloads at Mars," *Acta Astronautica*, Vol. 66, 2010, pp. 1146-1159
- [2] S. Berry, M. Rhode, K. Edquist, C. Player, "Supersonic Retropropulsion Experimental Results from the NASA Langley Unitary Plan Wind Tunnel," *American Institute of Aeronautics and Astronautics*, June 27, 2011
- [3] A. Korzun, J. Cruz, R. Braun, "A Survey of Supersonic Retropropulsion Technology for Mars Entry, Descent, and Landing," *IEEEAC paper 1246*, Version 12, Updated December 14, 2007
- [4] D. Schauerhamer, K. Trumble, B. Kleb, J. Carlson, K. Edquist, "Continuing Validation for Computational Fluid Dynamics For Supersonic Retropropulsion," *American Institute of Aeronautics and Astronautics*, January 1, 2011
- [5] S. Berry, M. Rhode, K. Edquist, "Supersonic Retropropulsion Experimental Results from the NASA Ames 9x7 Foot Supersonic Wind Tunnel," *American Institute of Aeronautics and Astronautics*, June 25, 2012
- [6] K. Zarchi, D. Shauerhamer, W. Kleb, J. Carlson, K. Edquist, "Computational Fluid Dynamics Validation and Post-test Analysis of Supersonic Retropropulsion in the Ames 9x7 Unitary Tunnel," *American Institute of Aeronautics and Astronautics*, June 25, 2012
- [7] C. Cordell Jr, I. Clark, R. Braun, "CFD Verification of Supersonic Retropropulsion for a Central and Peripheral Configuration," *IEEEAC paper 1190*, Version 3, Updated January 11, 2011
- [8] B. Steinfeldt, J. Thesinger, A. Korzun, I. Clark, M. Grant, R. Braun, "High Mass Mars Entry, Descent, and Landing Architecture Assessment," *AIAA Space 2009 Conference & Exposition*, September 14-17, 2009
- [9] R. Braun, R. Manning, "Mars Exploration Entry, Descent and Landing Challenges"
- [10] C. Cordell Jr, R. Braun "An Analytical Approach to Modeling Supersonic Retropropulsion Flow Field Components," *AIAA Atmospheric Flight Mechanics Conference*, January 13-17, 2014
- [11] K. Edquist, A. Dyakonov, J. Shidner, J. Studak, M. Tigges, D. Kipp, R. Prakash, K. Trumble, I. Dupzyk, A. Korzun, "Development of Supersonic Retro-Propulsion for Future Mars Entry, Descent, and Landing Systems," *American Institute of Aeronautics and Astronautics*, June 28, 2010
- [12] T. Zang, A. Dwyer-Cianciolo, D. Kinney, A. Howard, G. Chen, M. Ivanov, R. Sostaric, C. Westhelle, "Overview of NASA Entry, Descent and Landing Systems Analysis Study," *American Institute of Aeronautics and Astronautics*, August 21, 2010
- [13] B. Venkatachari, Y. Ito, G. Cheng, C. Chang, "Numerical Investigation of the Interaction of Counterflowing Jets and Supersonic Capsule Flows," *American Institute of Aeronautics and Astronautics*, June 27, 2011
- [14] E. Daso, V. Pritchett, T. Wang, D. Ota, I. Blankson, A. Auslender, "The Dynamics of Shock Dispersion and Interactions in Supersonic Freestreams with Counterflowing Jets," *American Institute of Aeronautics and Astronautics*, January 1, 2007
- [15] K. Trumble, D. Schauerhamer, W. Kleb, K. Edquist, "Analysis of Navier-Stokes Codes Applied to Supersonic Retro-Propulsion Wind Tunnel Test," *IEEEAC paper 1471*, Version 1, Updated October 26, 2010
- [16] "Mars-SpaceX" retrieved from url: http://www.spacex.com/sites/spacex/files/mars_presentation.pdf

[17] Baker, D., "NASA space shuttle manual: an insight into the design, construction and operation of the NASA space shuttle", Sparkford: Haynes, 2011.

[18] Newlands, R., "The Thrust Optimised Parabolic Nozzle", Aspire Space Technical Papers

[19] Trumble, L., Schauerhamer, D., Kleb, W., Carlson, J., Buning, P., Edquist, K., Barnhardt, M., "An Initial Assessment of Navier-Stokes Codes Applied to Supersonic Retro-Propulsion", American Institute of Aeronautics and Astronautics, July 1, 2010

[20] Bakhtian, N., Aftosmis, M., "Parametric Study of Peripheral Nozzle Configurations for Supersonic Retropropulsion" Journal of Spacecraft and Rockets, Vol. 47, No. 6, November - December 2010

Appendix A - Mesh Temperature and Pressure Figures

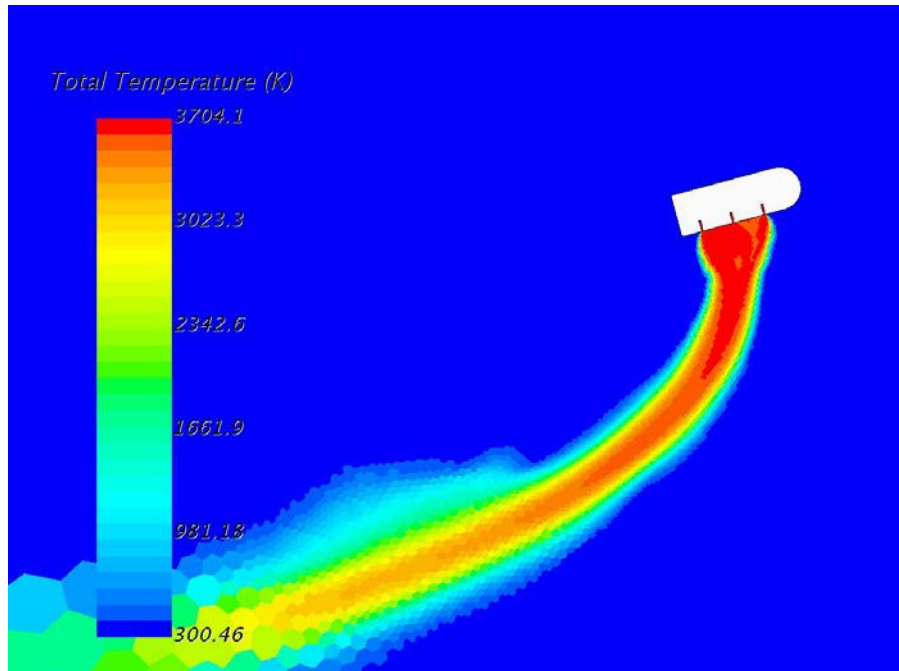


Fig. 110 $\alpha = 15^\circ$, Mach 1

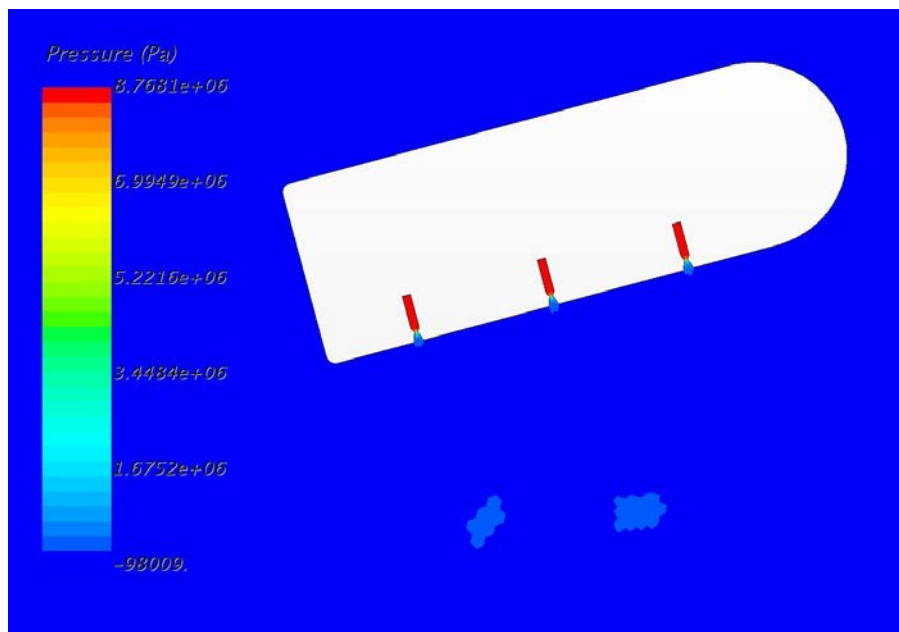


Fig. 111 $\alpha = 15^\circ$, Mach 1

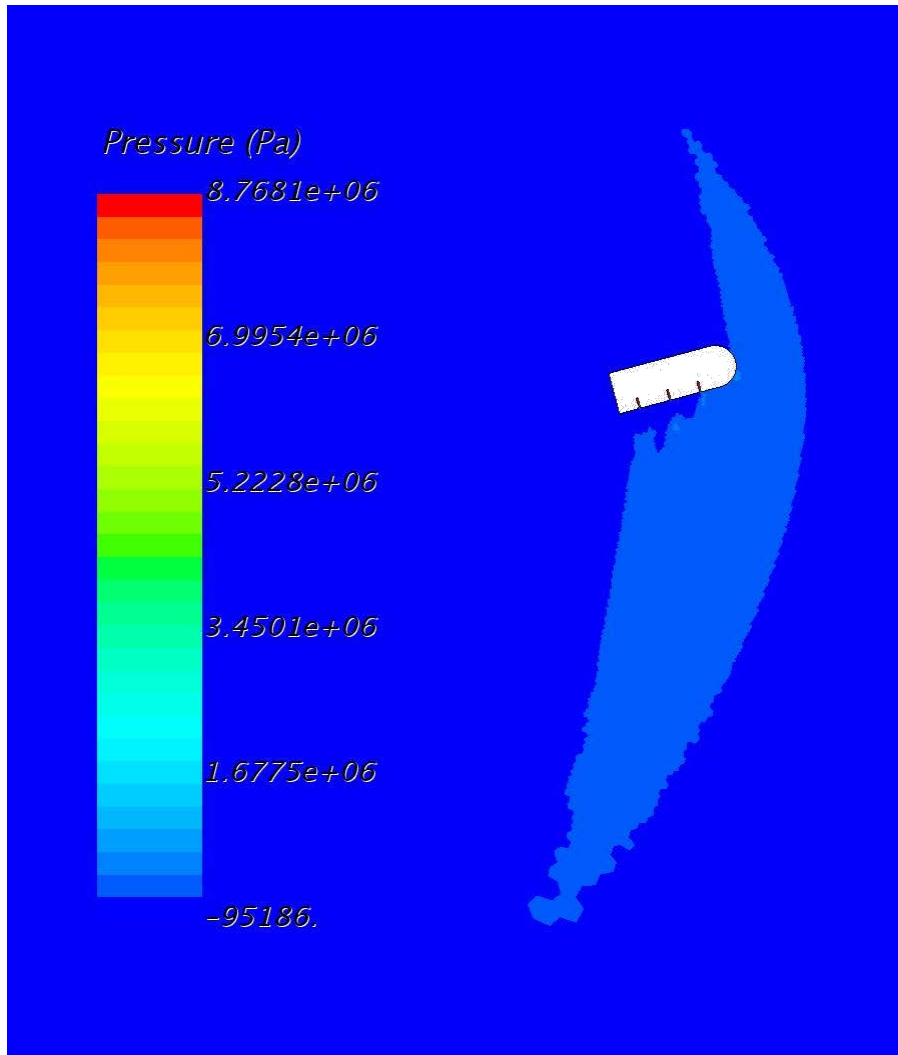


Fig. 112 $\alpha = 15^\circ$, Mach 2

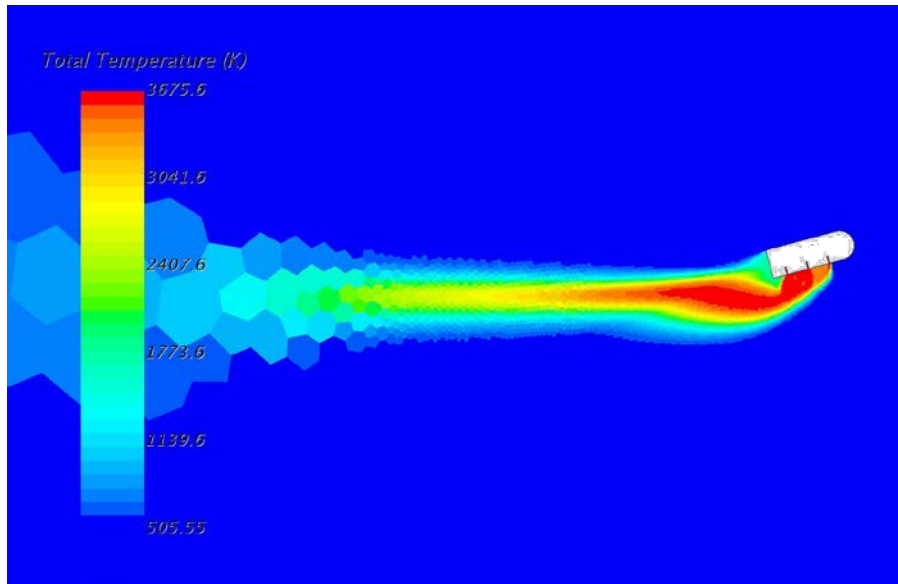


Fig. 113 $\alpha = 15^\circ$, Mach 2

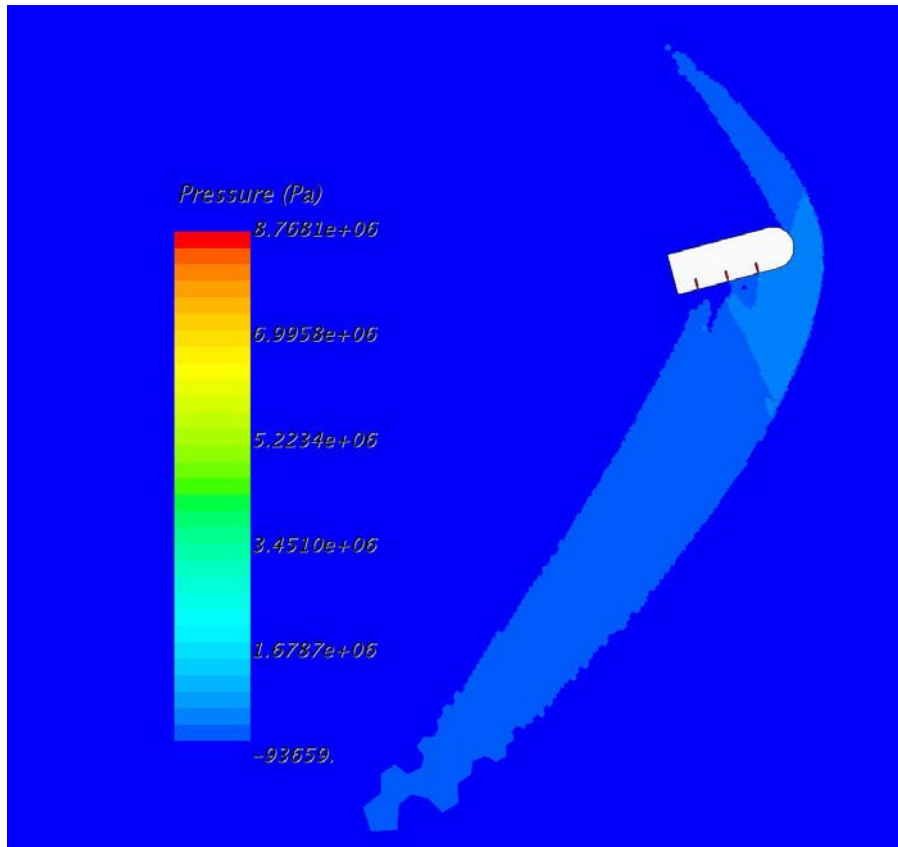


Fig. 114 $\alpha = 15^\circ$, Mach 2.5

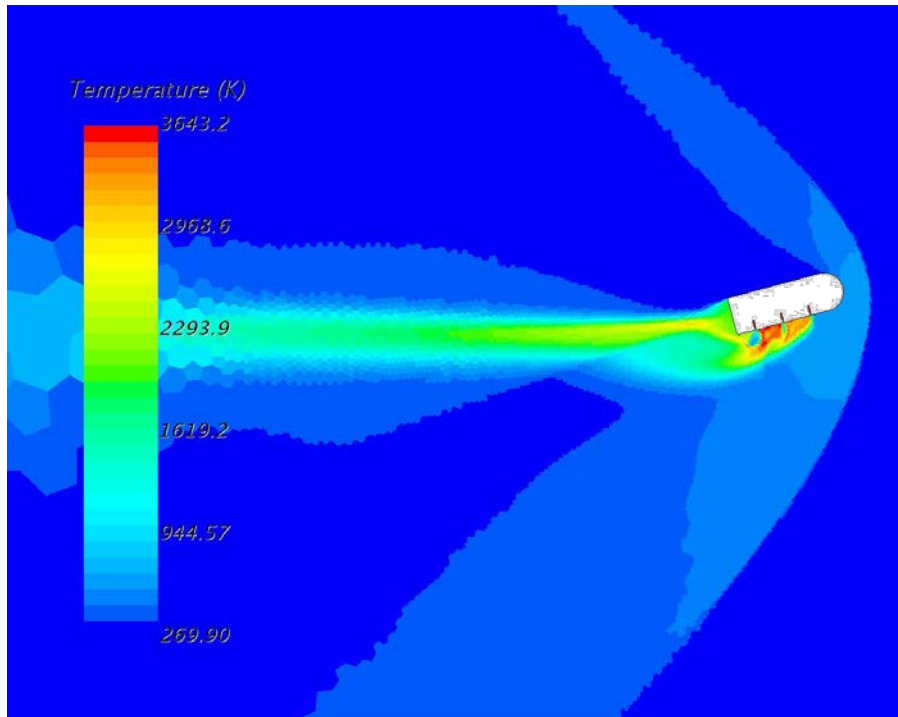


Fig. 115 $\alpha = 15^\circ$, Mach 2.5

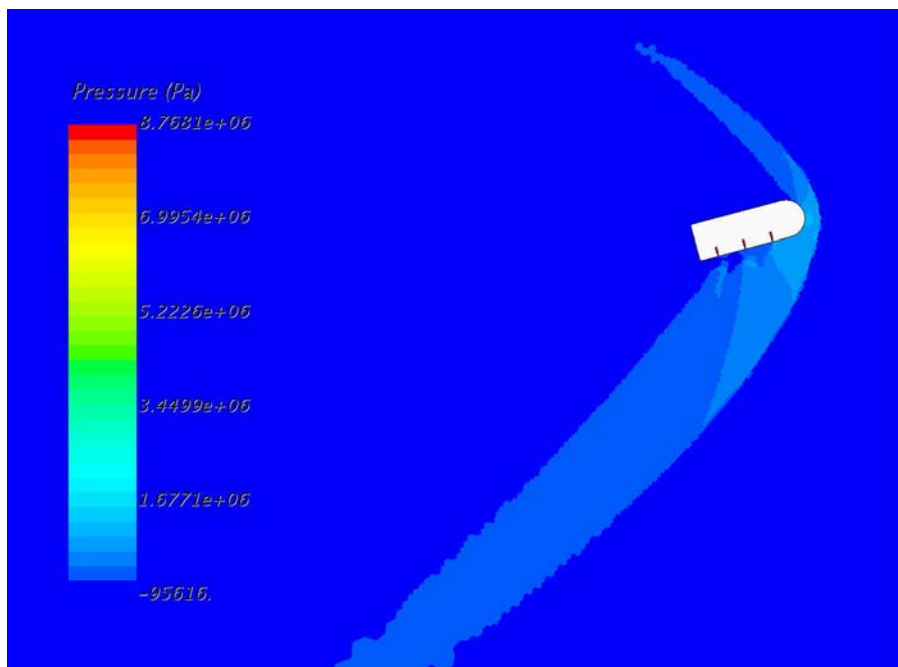


Fig. 116 $\alpha = 15^\circ$, Mach 3

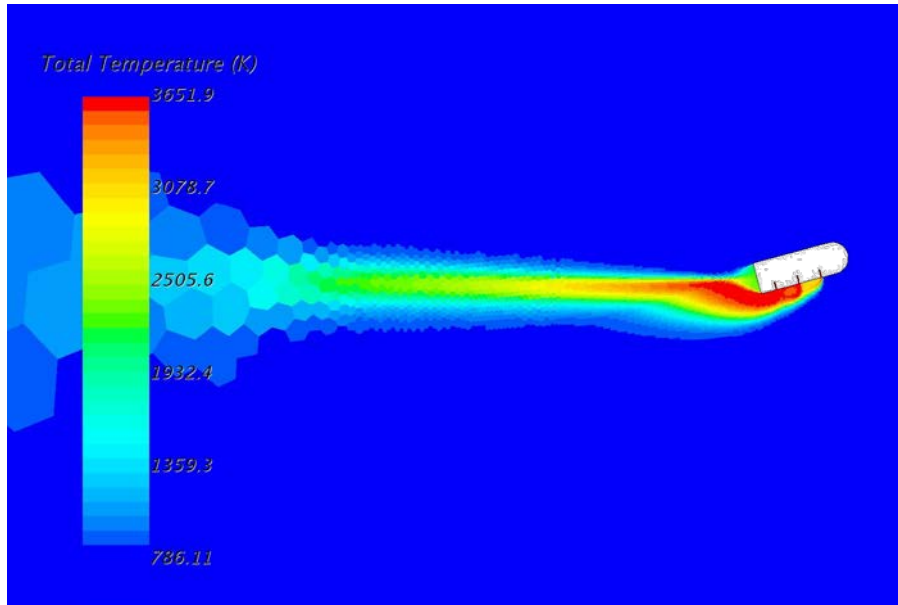


Fig. 117 $\alpha = 15^\circ$, Mach 3

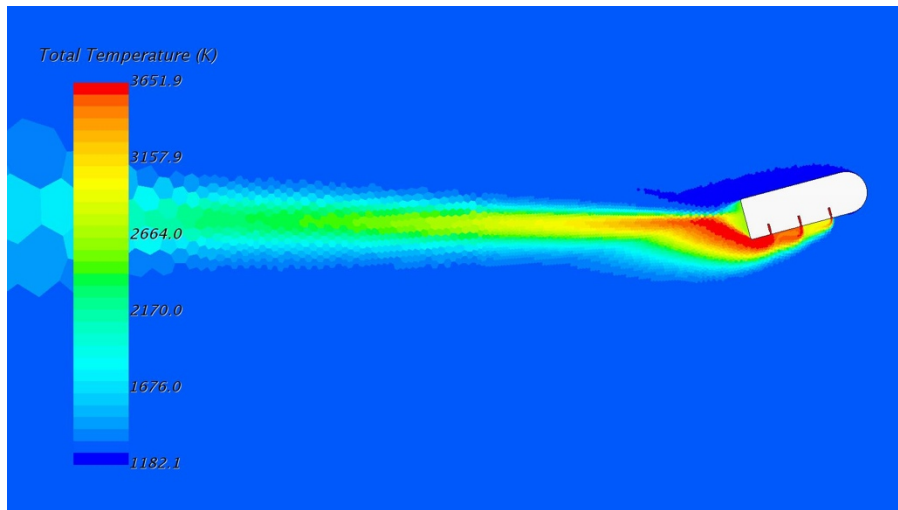


Fig. 118 $\alpha = 15^\circ$, Mach 4

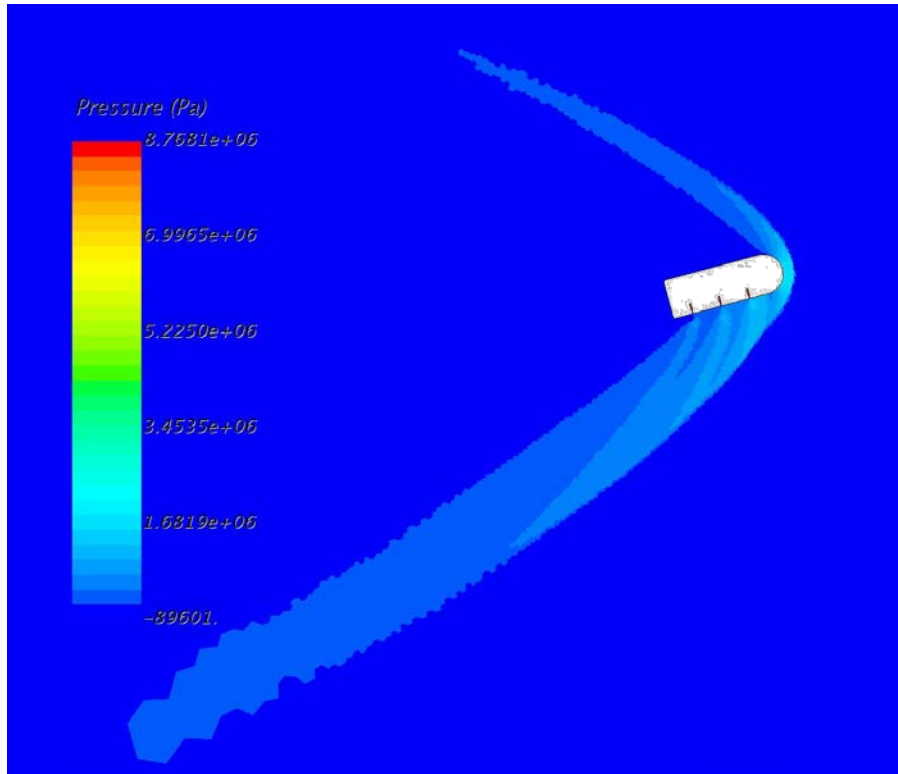


Fig. 119 $\alpha = 15^\circ$, Mach 4

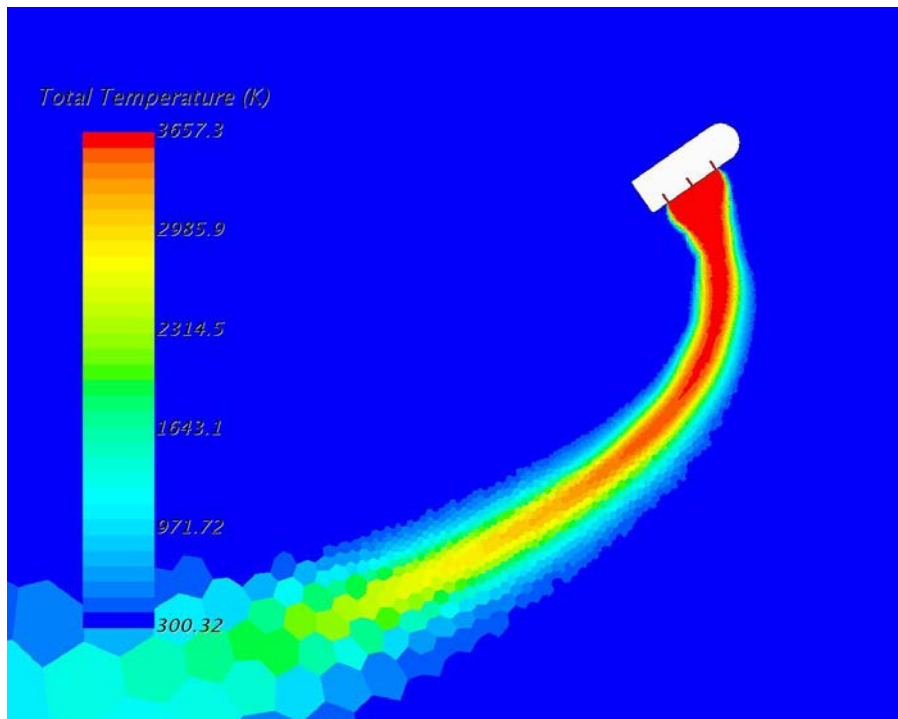


Fig. 120 $\alpha = 30^\circ$, Mach 1

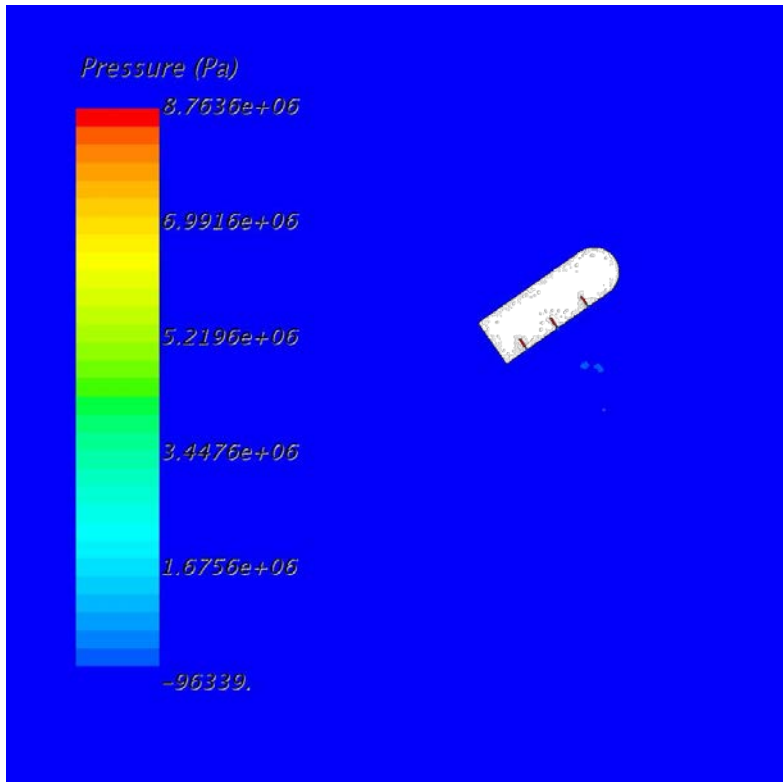


Fig. 121 $\alpha = 30^\circ$, Mach 1

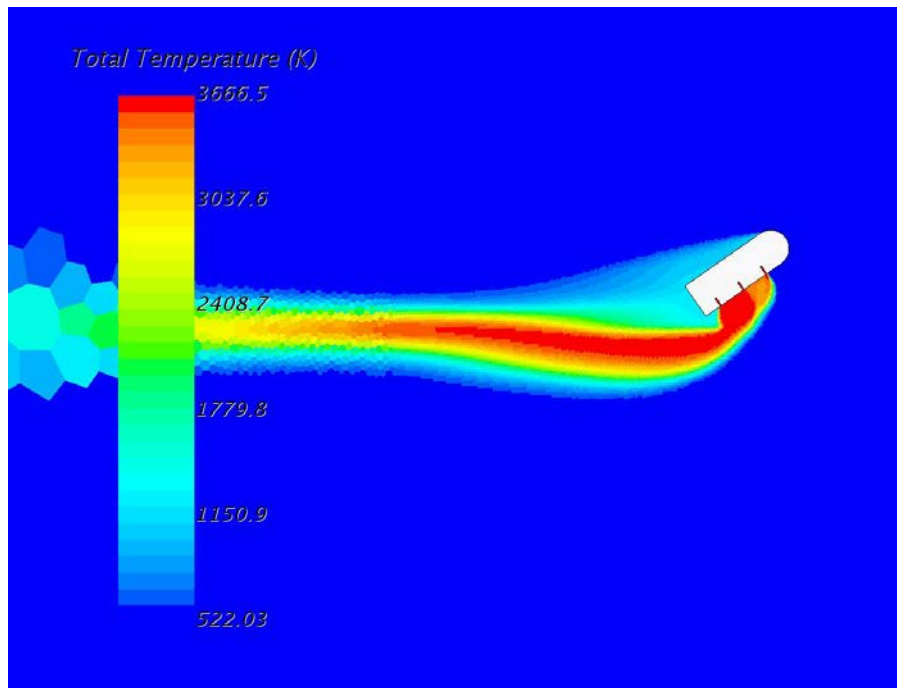


Fig. 122 $\alpha = 30^\circ$, Mach 2

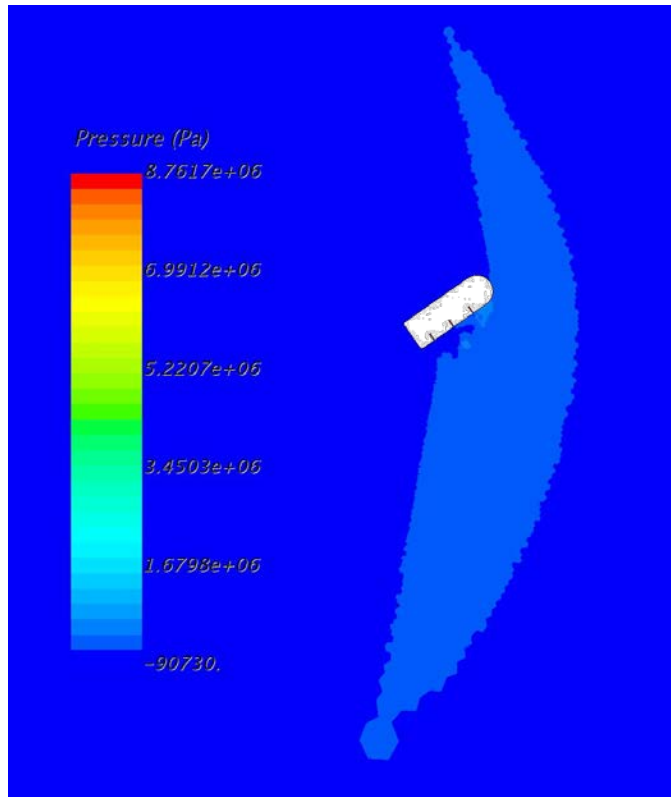


Fig. 123 $\alpha = 30^\circ$, Mach 2

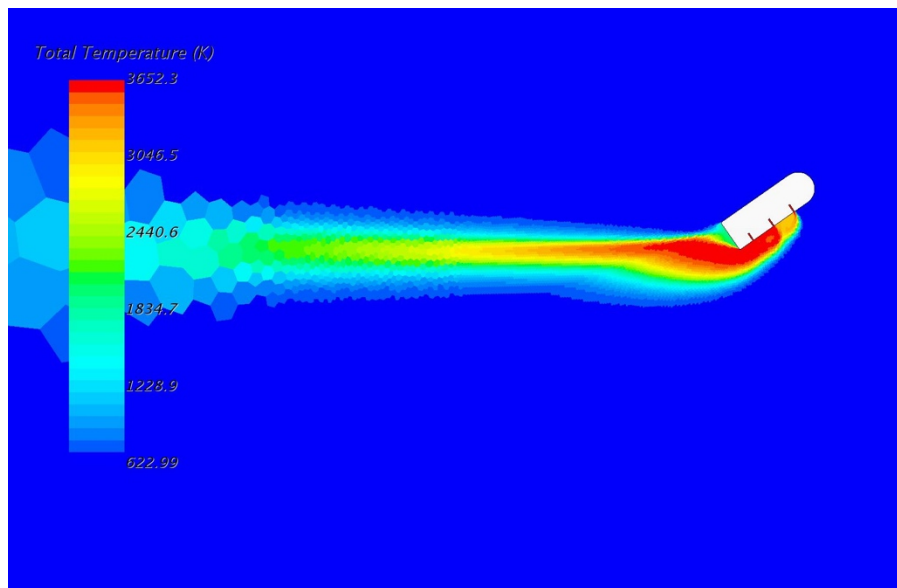


Fig. 124 $\alpha = 30^\circ$, Mach 2.5

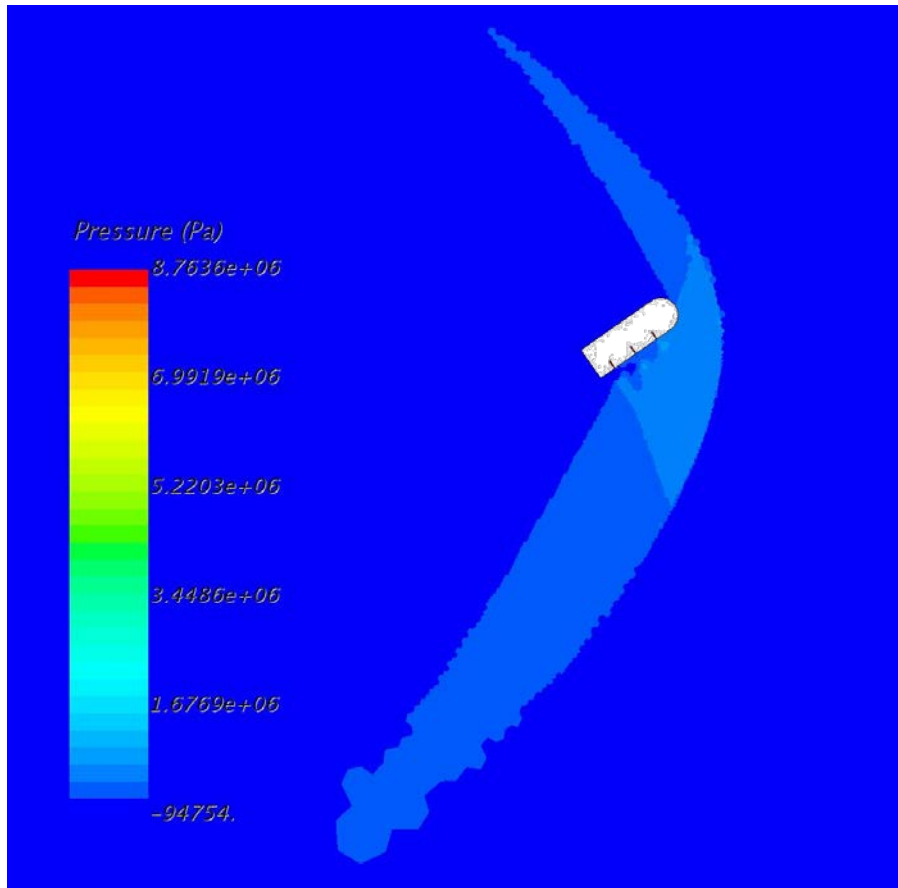


Fig. 125 $\alpha = 30^\circ$, Mach 2.5

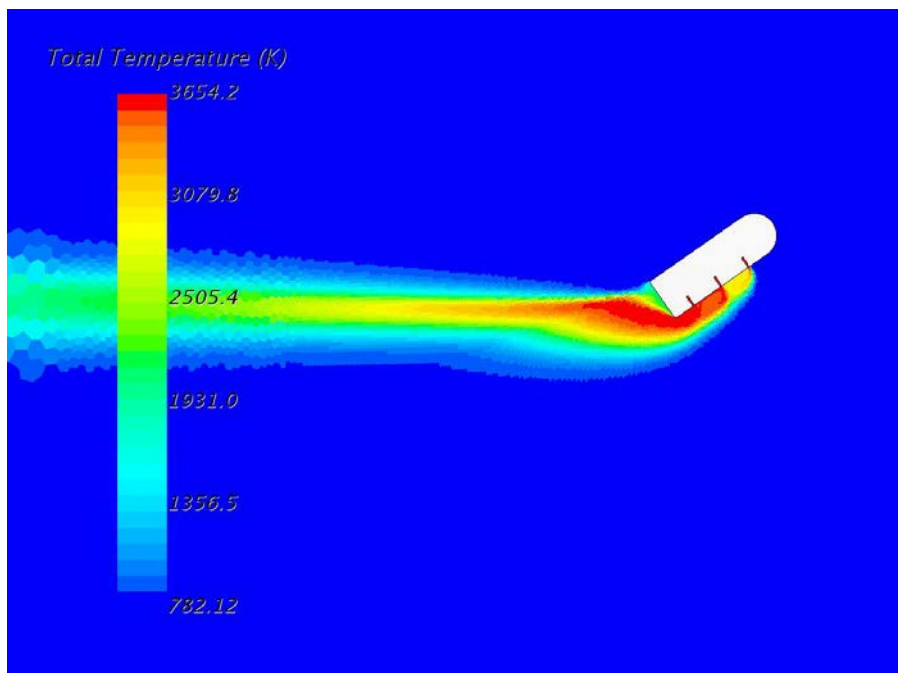


Fig. 126 $\alpha = 30^\circ$, Mach 3

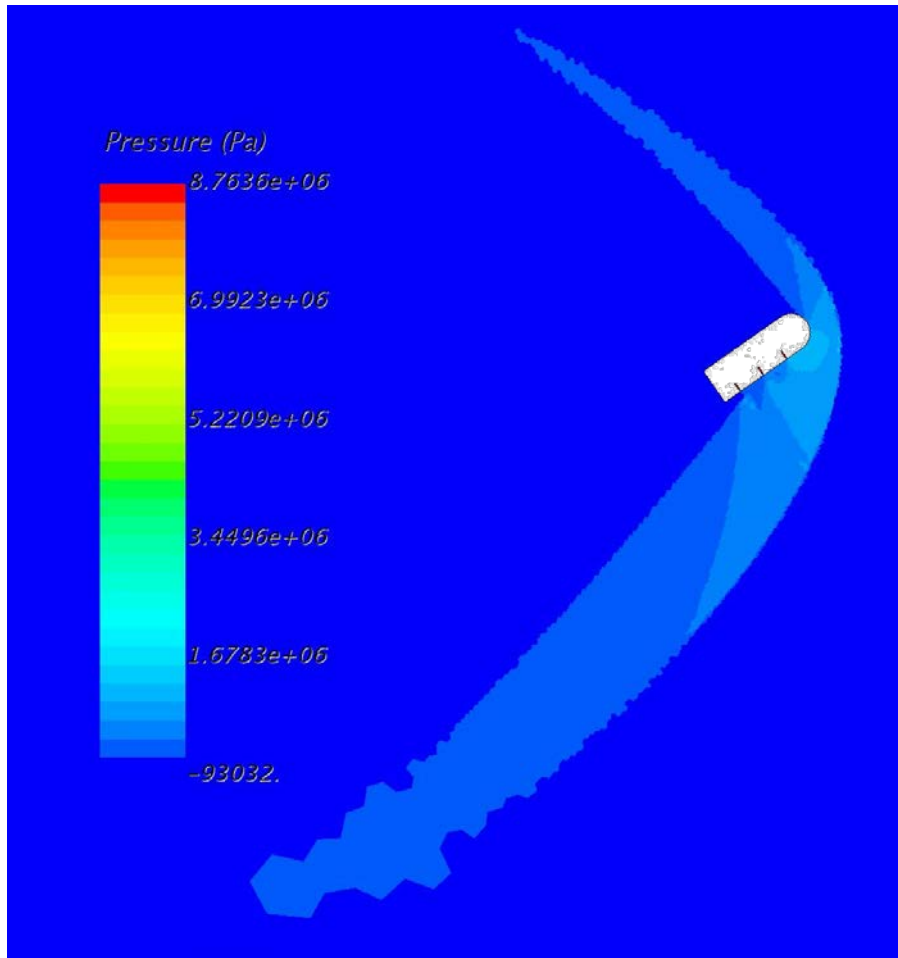


Fig. 127 $\alpha = 30^\circ$, Mach 3

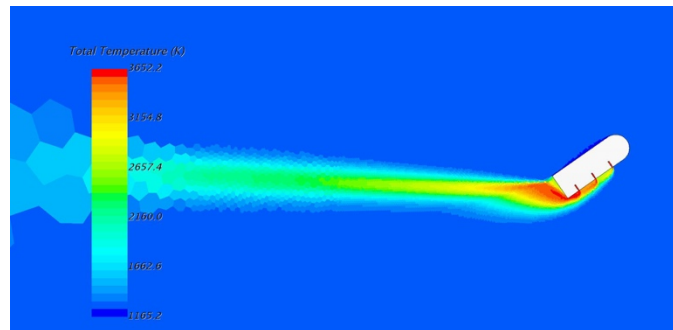


Fig. 128 $\alpha = 30^\circ$, Mach 4

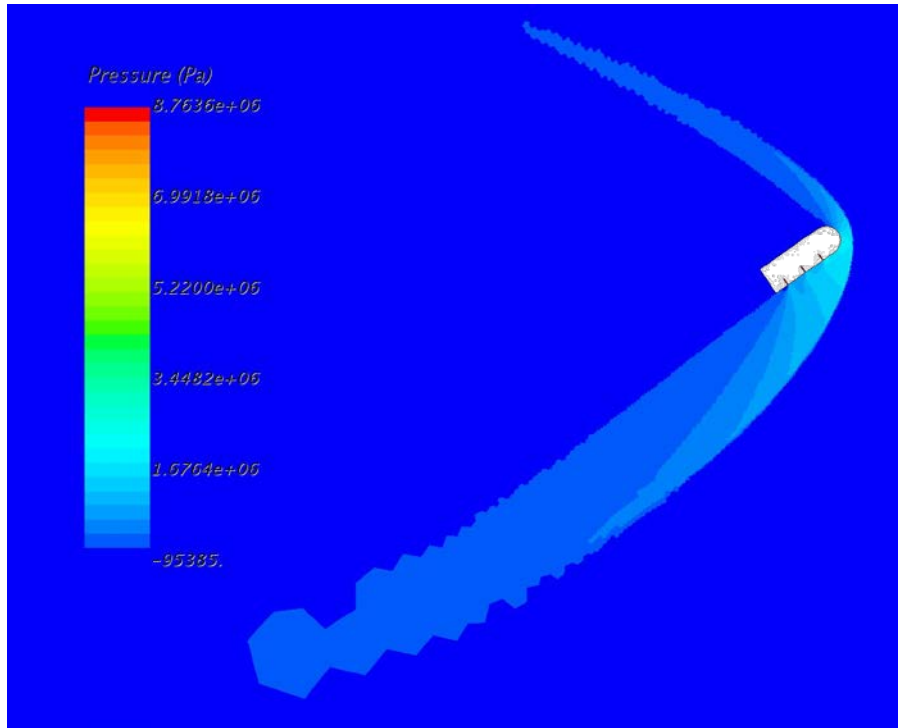


Fig. 129 $\alpha = 30^\circ$, Mach 4

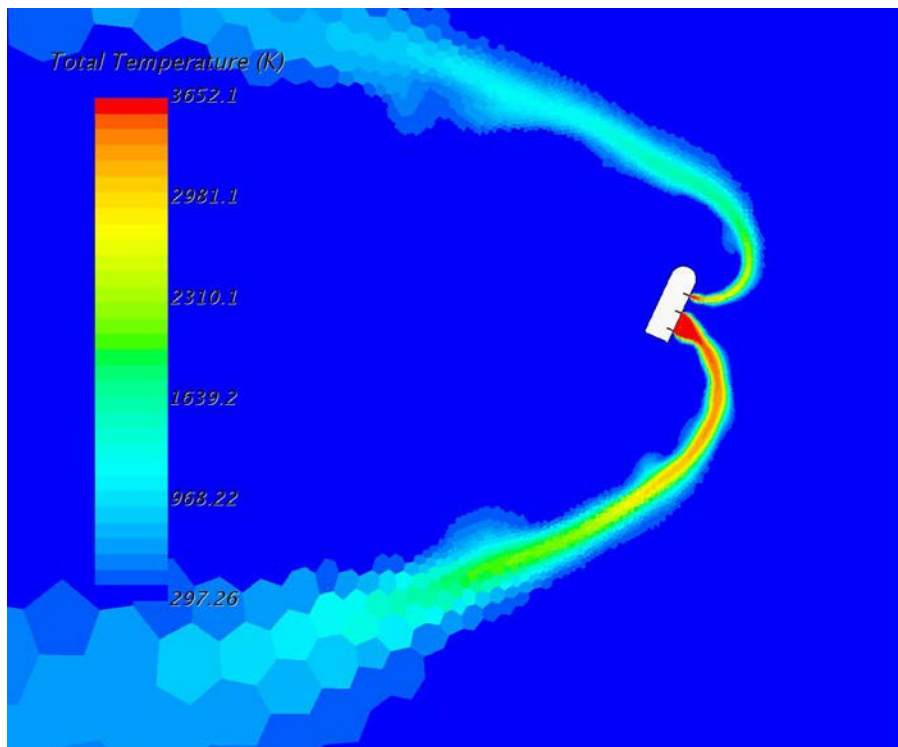


Fig. 130 $\alpha = 60^\circ$, Mach 1

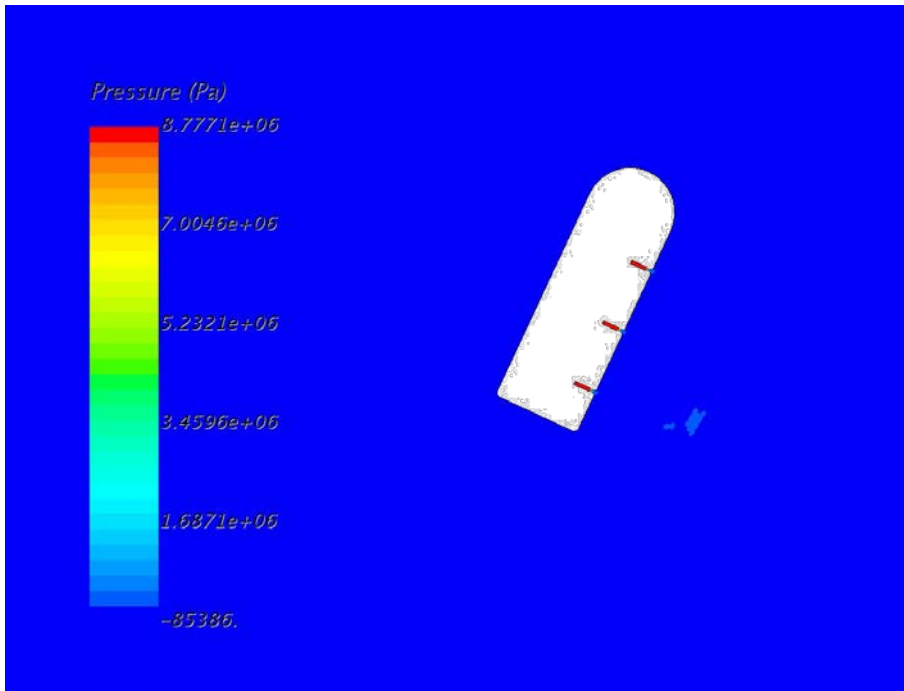


Fig. 131 $\alpha = 60^\circ$, Mach 1

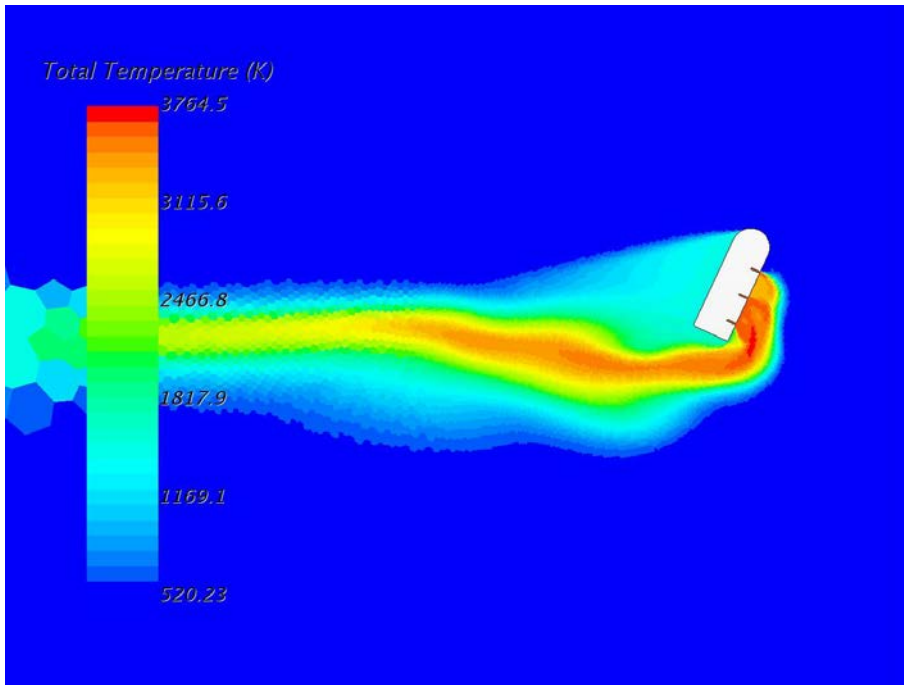


Fig. 132 $\alpha = 60^\circ$, Mach 2

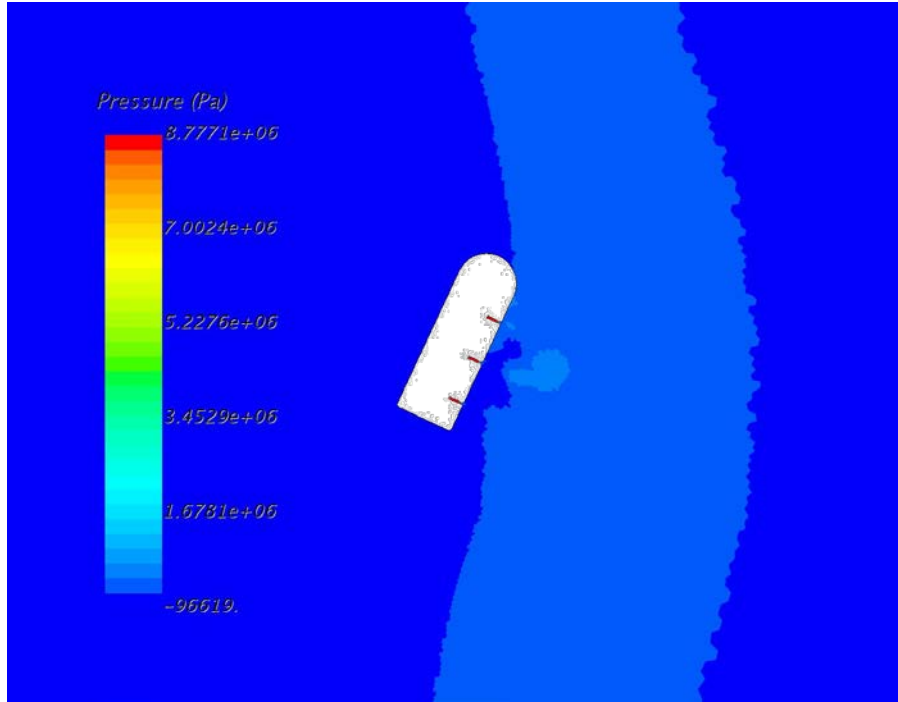


Fig. 133 $\alpha = 60^\circ$, Mach 2

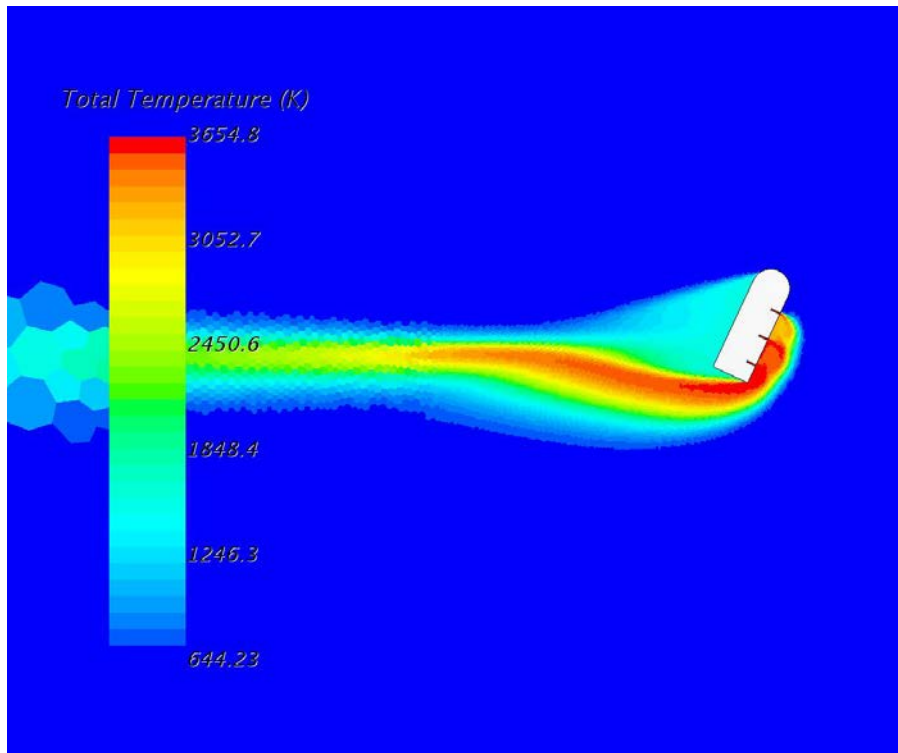


Fig. 134 $\alpha = 60^\circ$, Mach 2.5

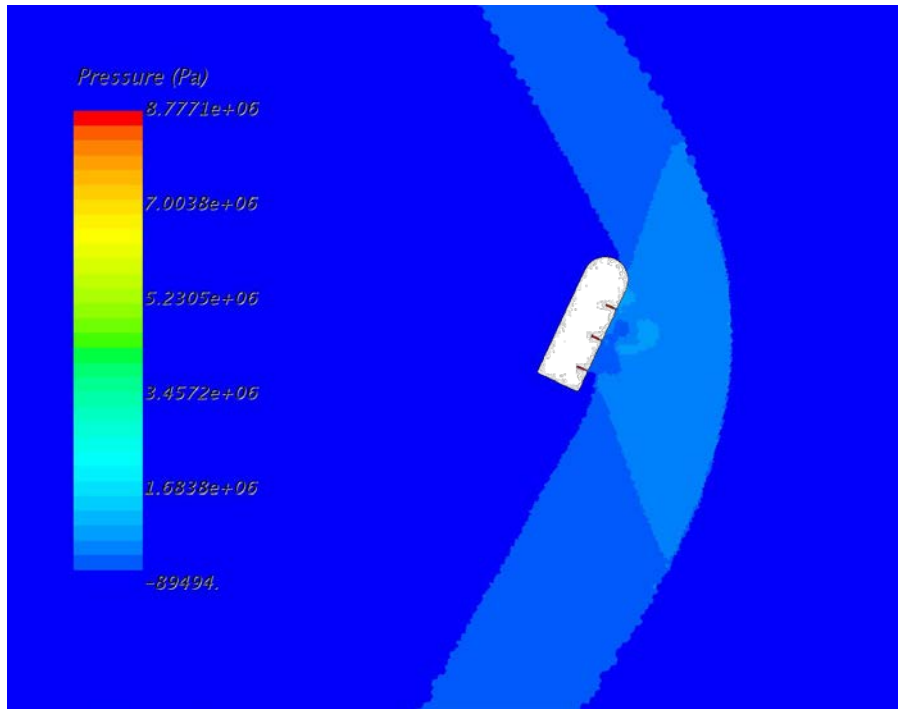


Fig. 135 $\alpha = 60^\circ$, Mach 2.5

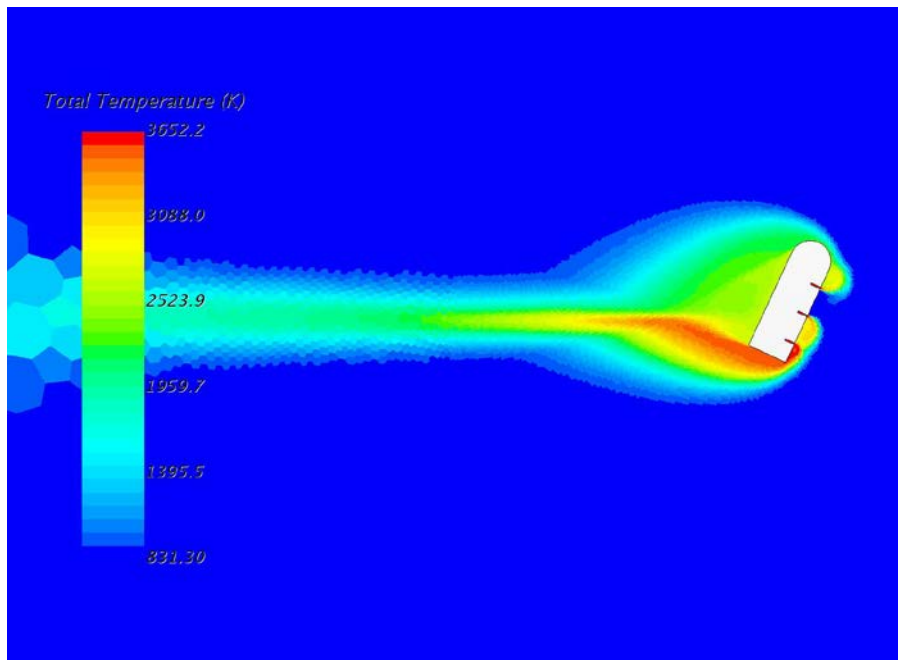


Fig. 136 $\alpha = 60^\circ$, Mach 3

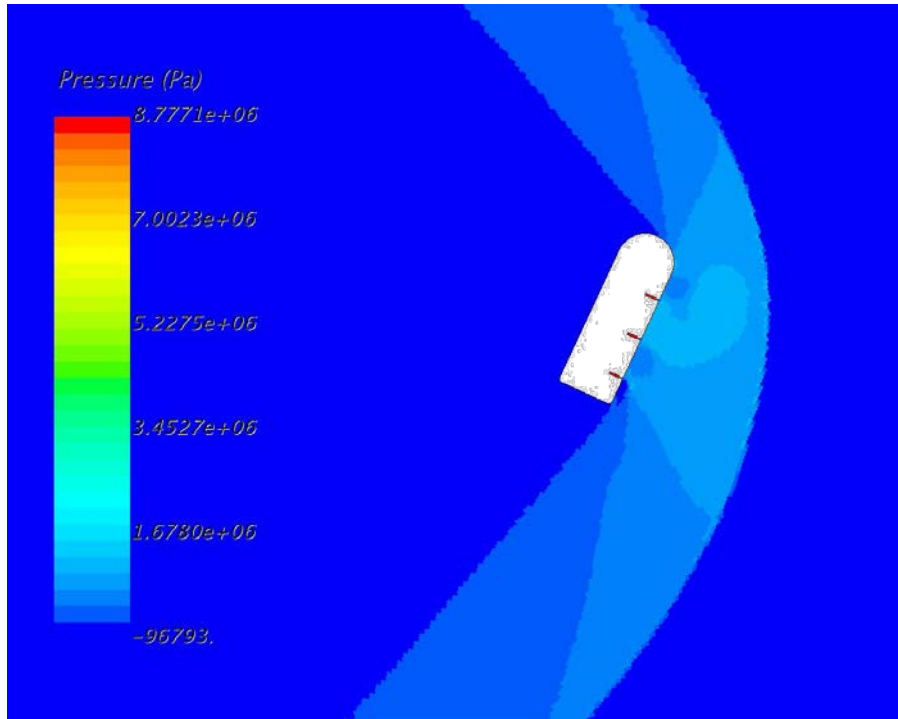


Fig. 137 $\alpha = 60^\circ$, Mach 3

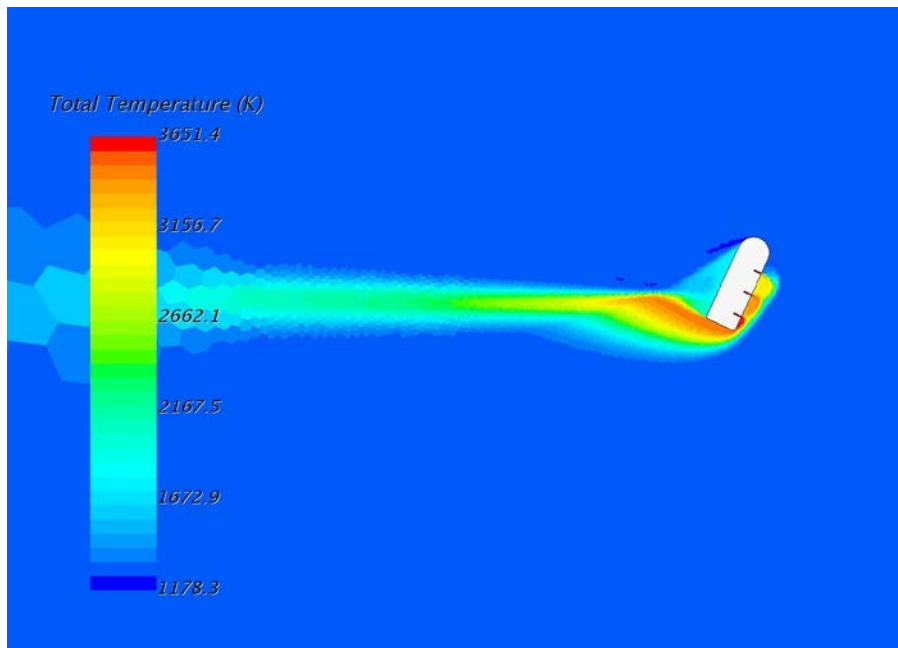


Fig. 138 $\alpha = 60^\circ$, Mach 4

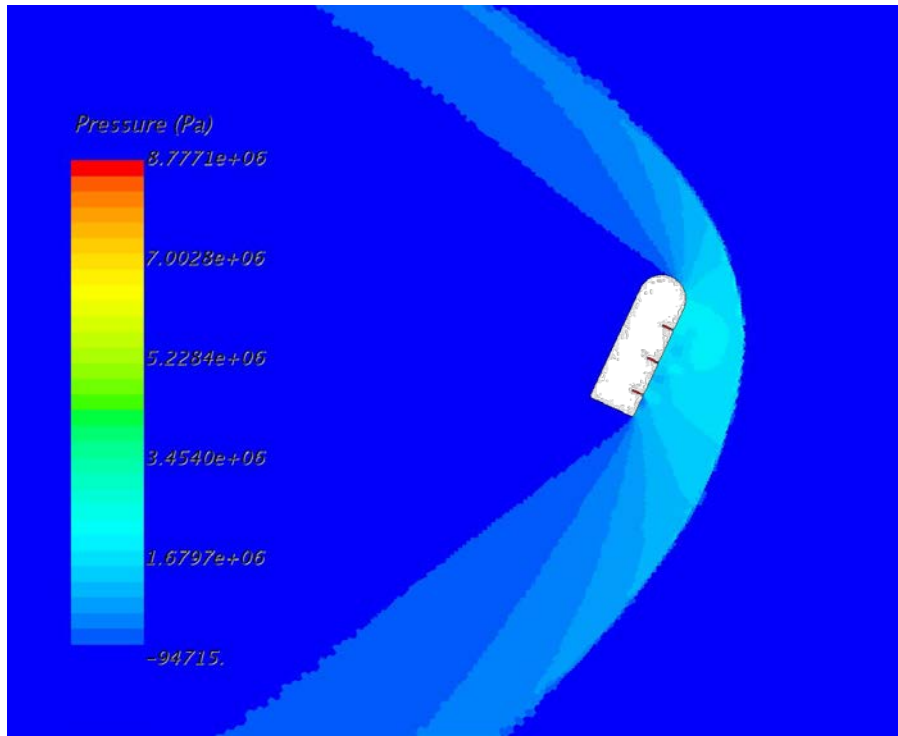


Fig. 139 $\alpha = 60^\circ$, Mach 4

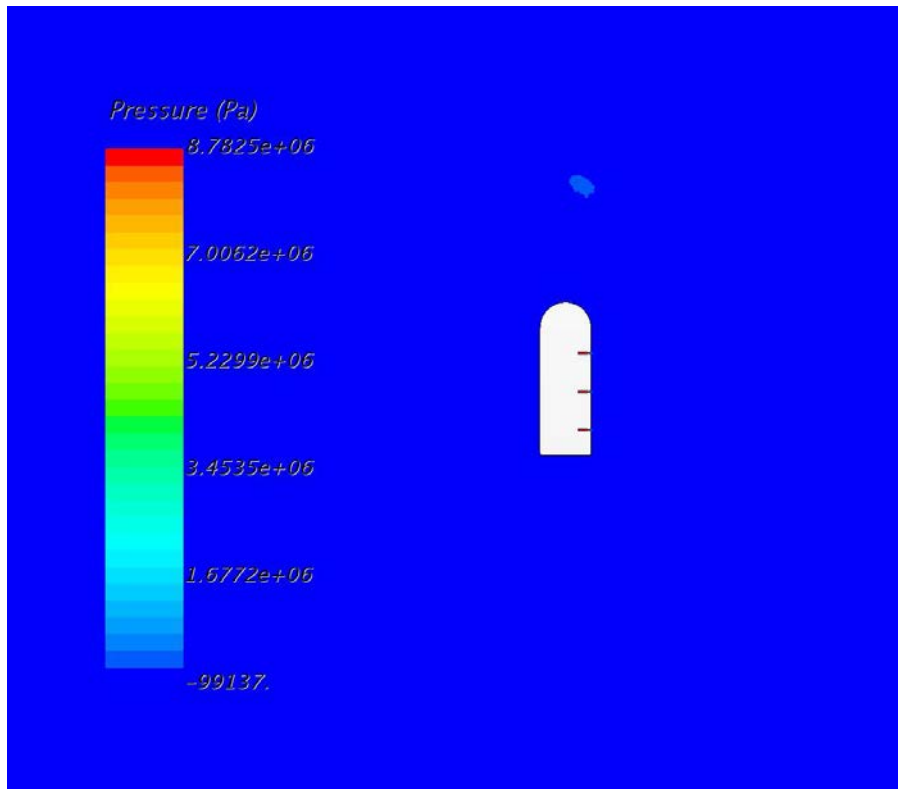


Fig. 140 $\alpha = 90^\circ$, Mach 1

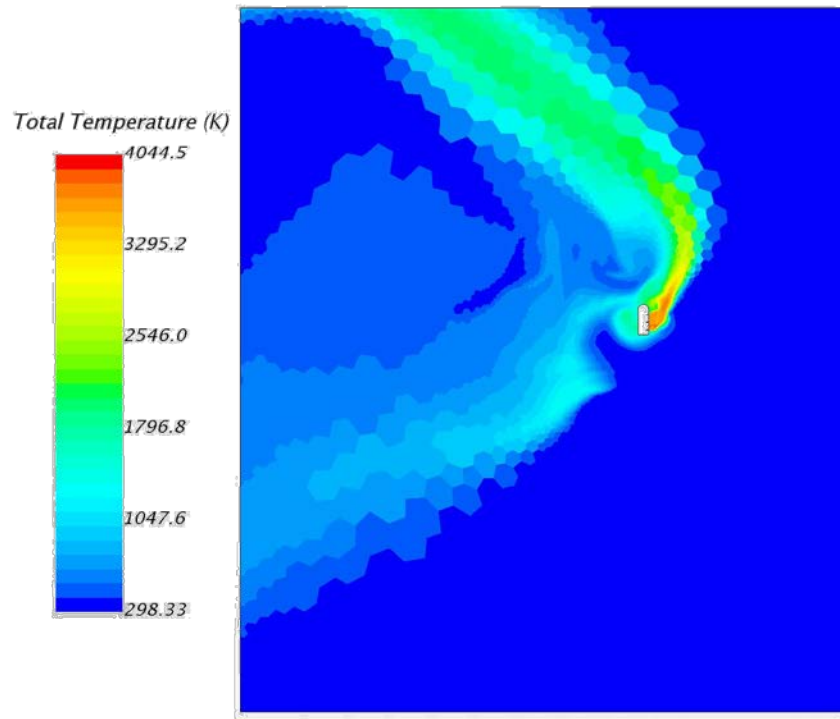


Fig. 141 $\alpha = 90^\circ$, Mach 1

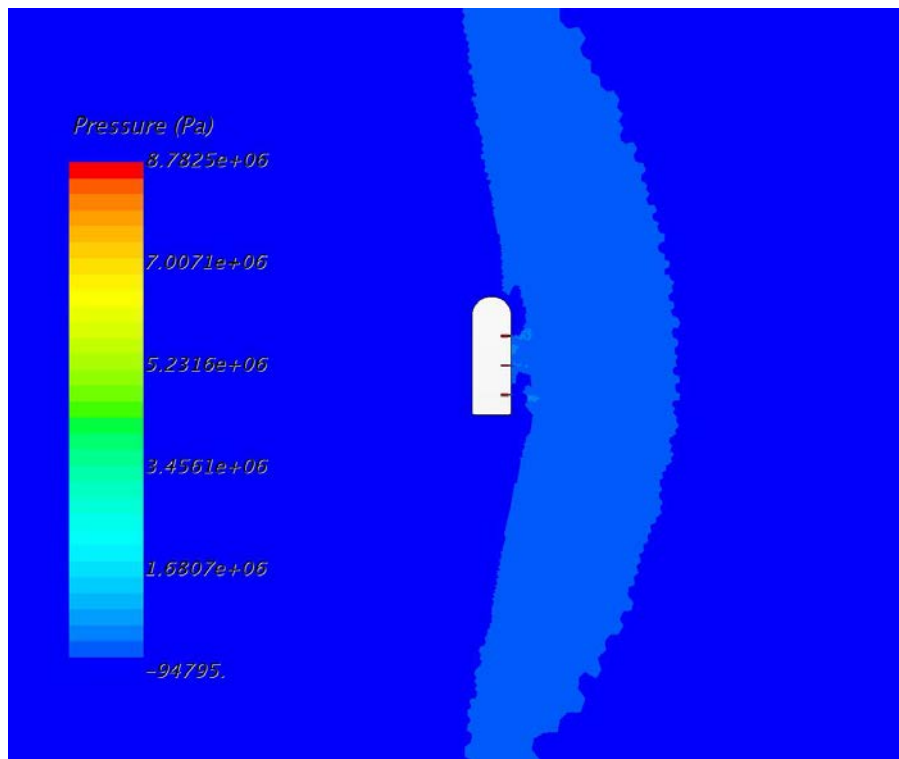


Fig. 142 $\alpha = 90^\circ$, Mach 2

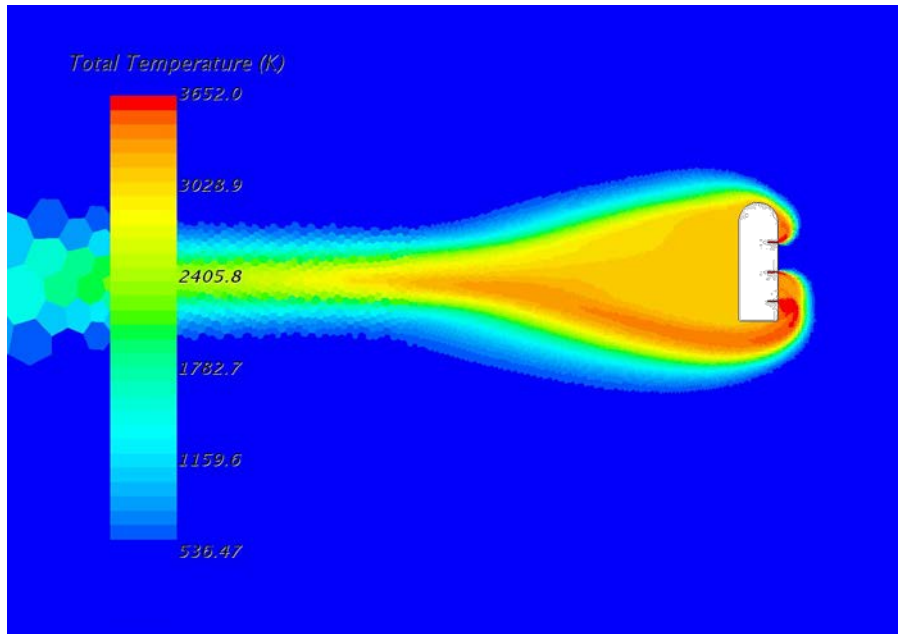


Fig. 143 $\alpha = 90^\circ$, Mach 2

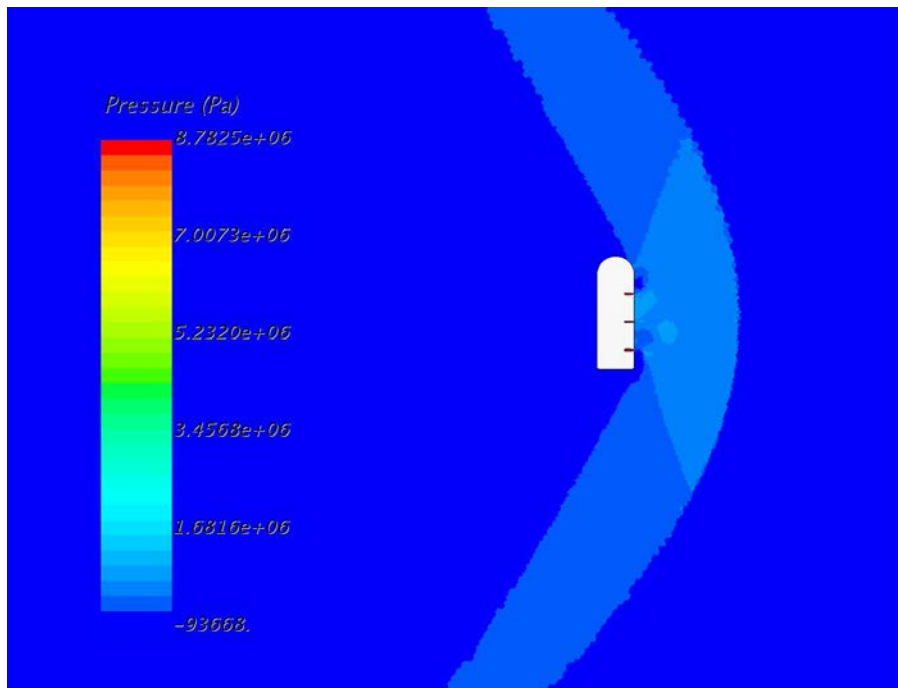


Fig. 144 $\alpha = 90^\circ$, Mach 2.5

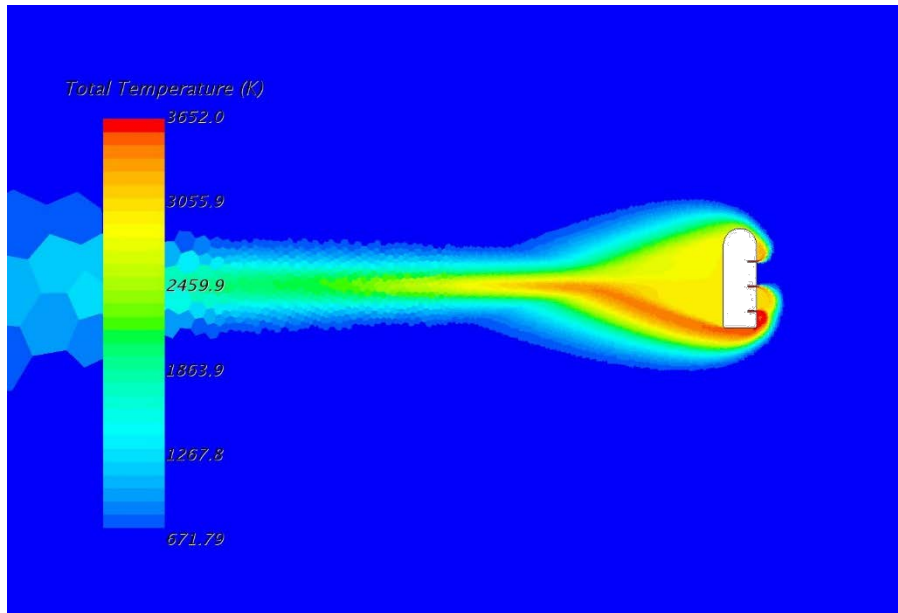


Fig. 145 $\alpha = 90^\circ$, Mach 2.5

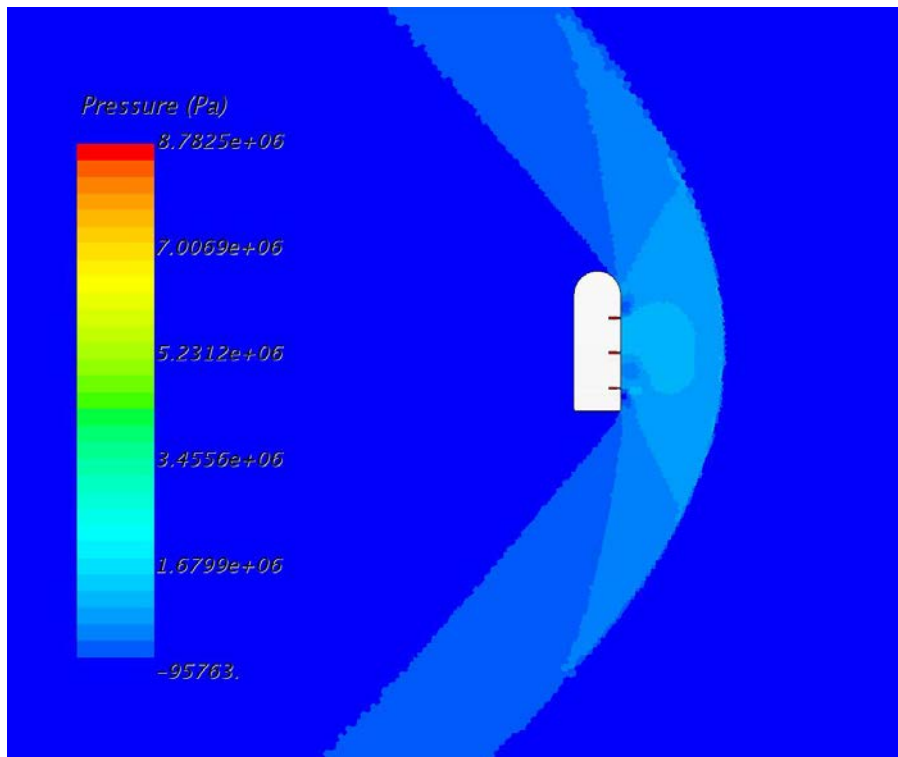


Fig. 146 $\alpha = 90^\circ$, Mach 3

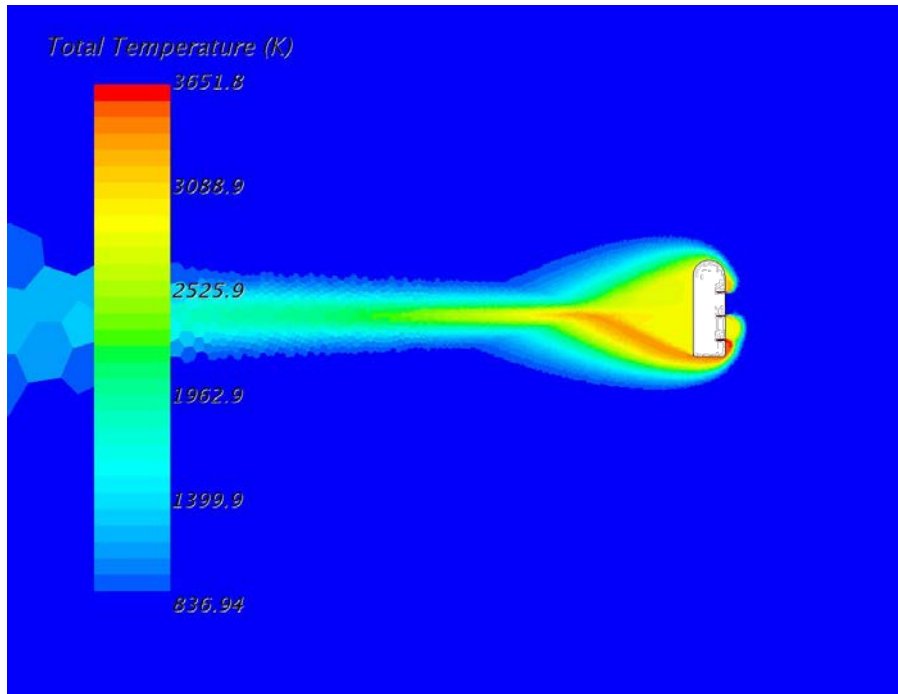


Fig. 147 $\alpha = 90^\circ$, Mach 3

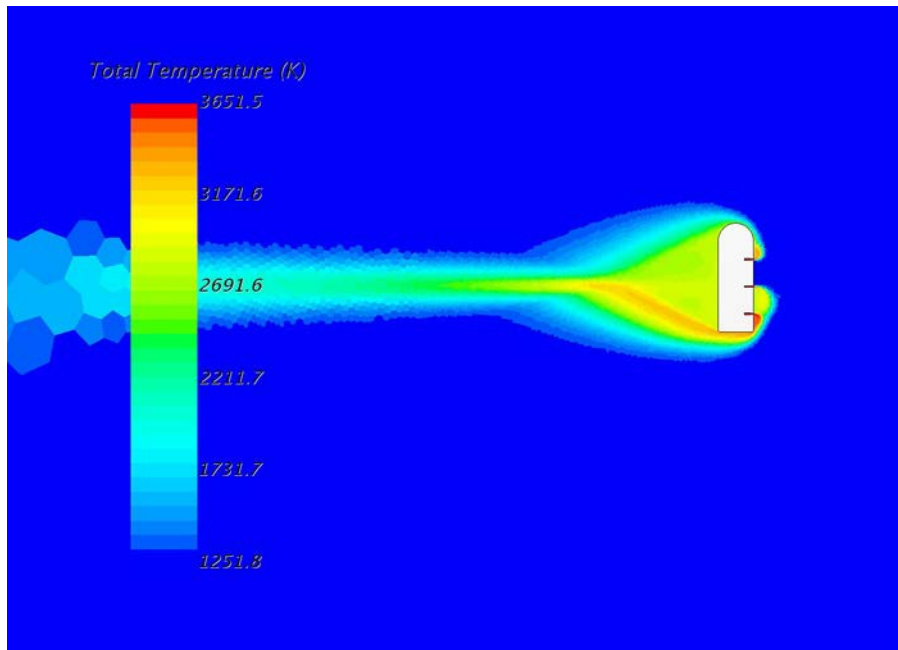


Fig. 148 $\alpha = 90^\circ$, Mach 4

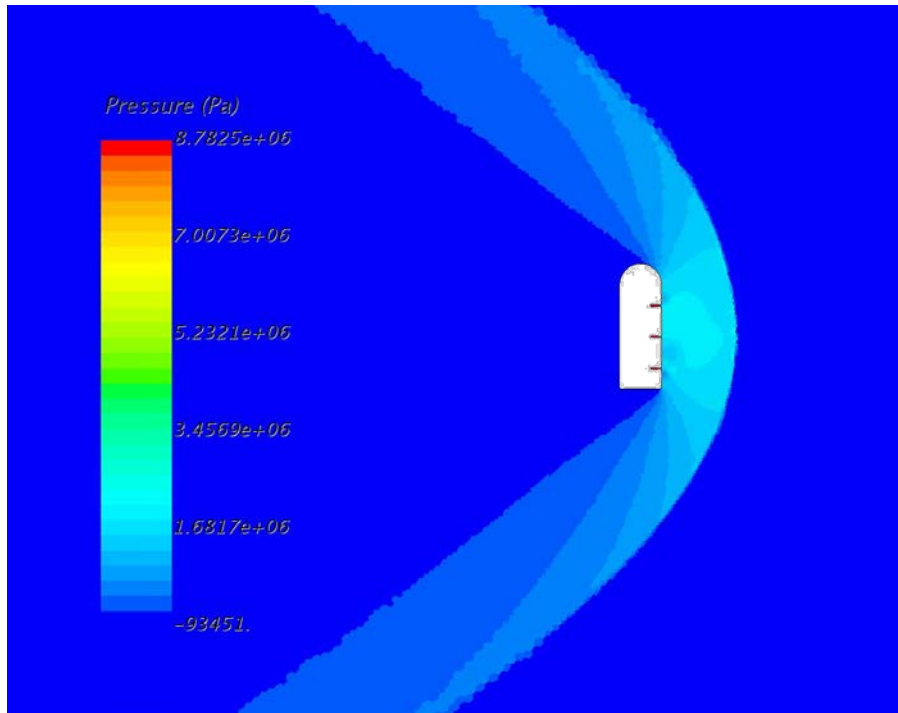


Fig. 149 $\alpha = 90^\circ$, Mach 4

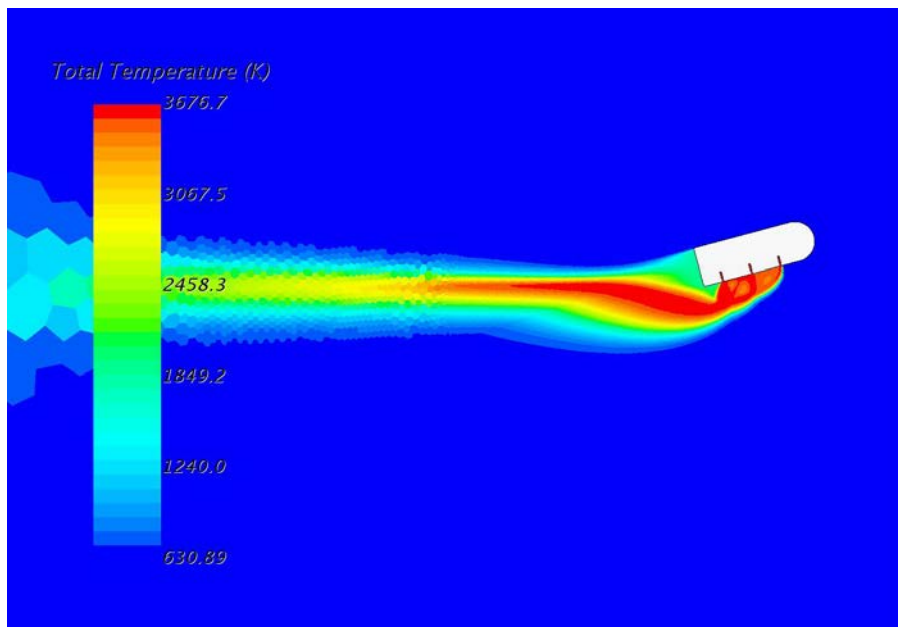


Fig. 150 $\alpha = 15^\circ$, Mach 1, Refined Mesh

Refined Mesh Temperature and Pressure Figures

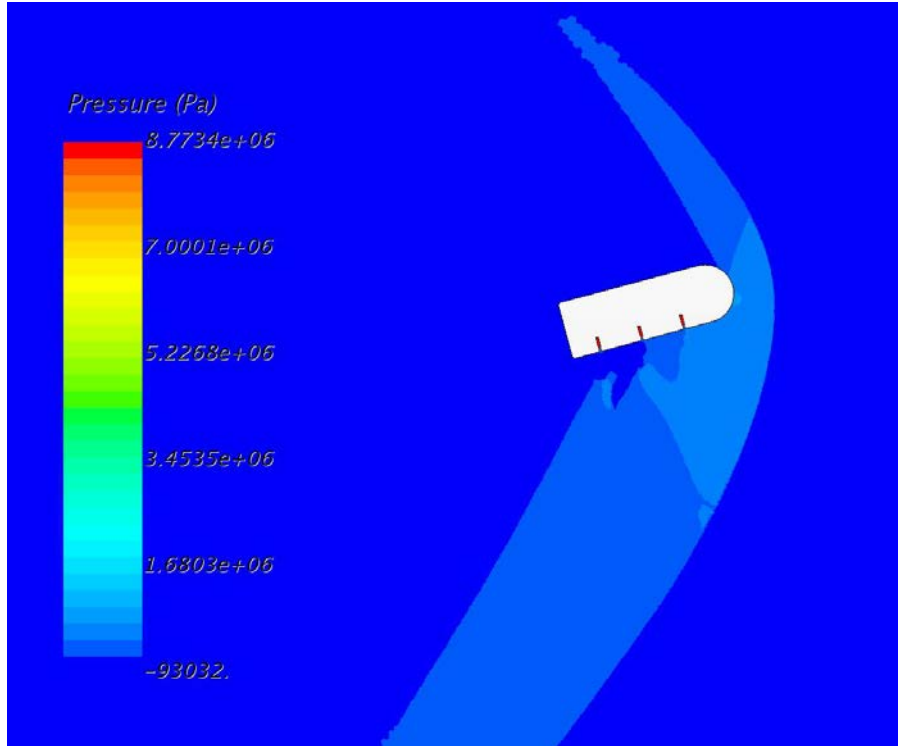


Fig. 151 $\alpha = 15^\circ$, Mach 2.5, Refined Mesh

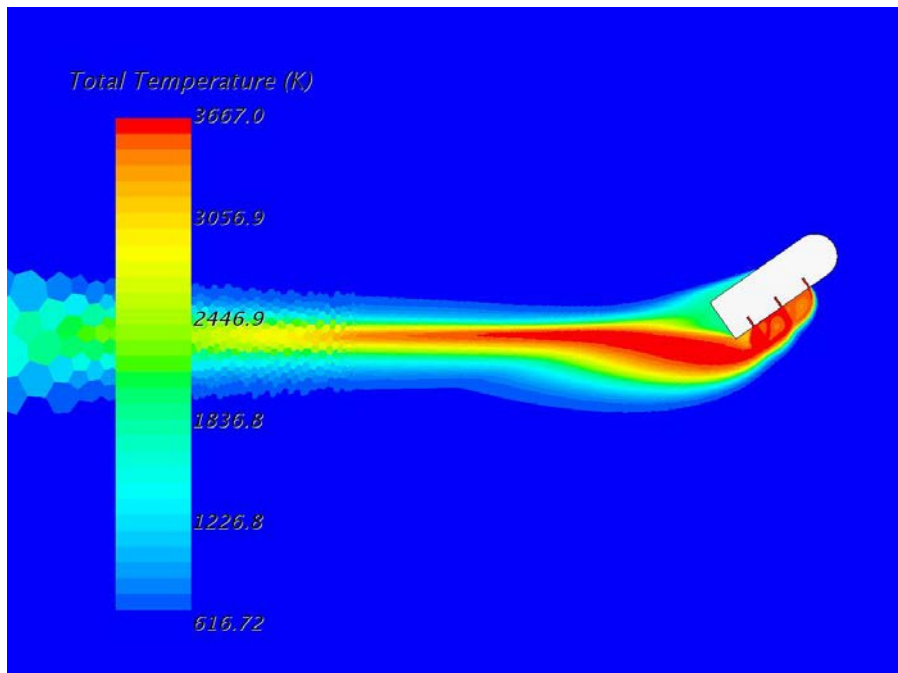


Fig. 152 $\alpha = 30^\circ$, Mach 2.5, Refined Mesh

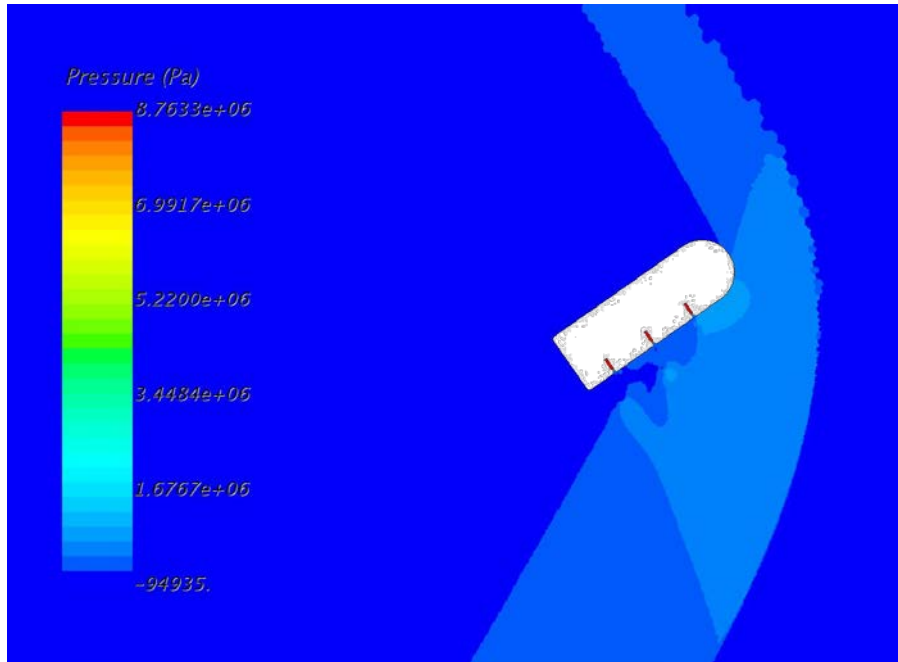


Fig. 153 $\alpha = 30^\circ$, Mach 2.5, Refined Mesh

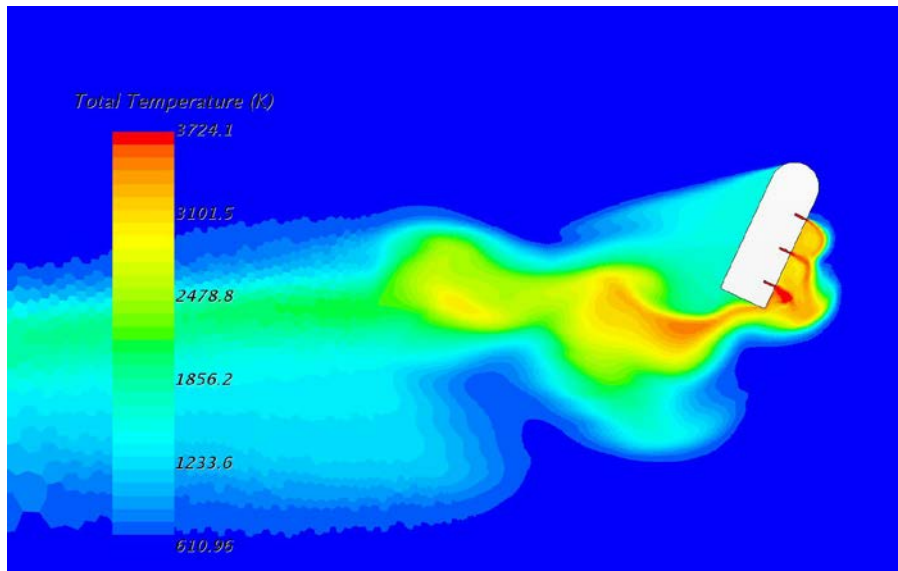


Fig. 154 $\alpha = 60^\circ$, Mach 2.5, Refined Mesh

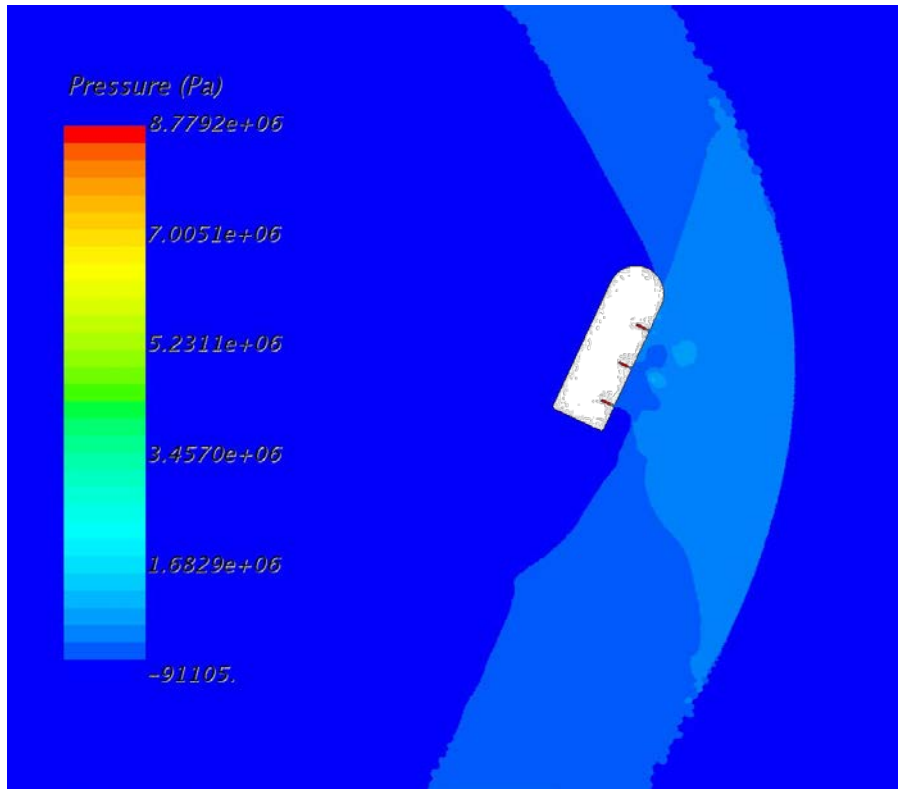


Fig. 155 $\alpha = 60^\circ$, Mach 2.5, Refined Mesh

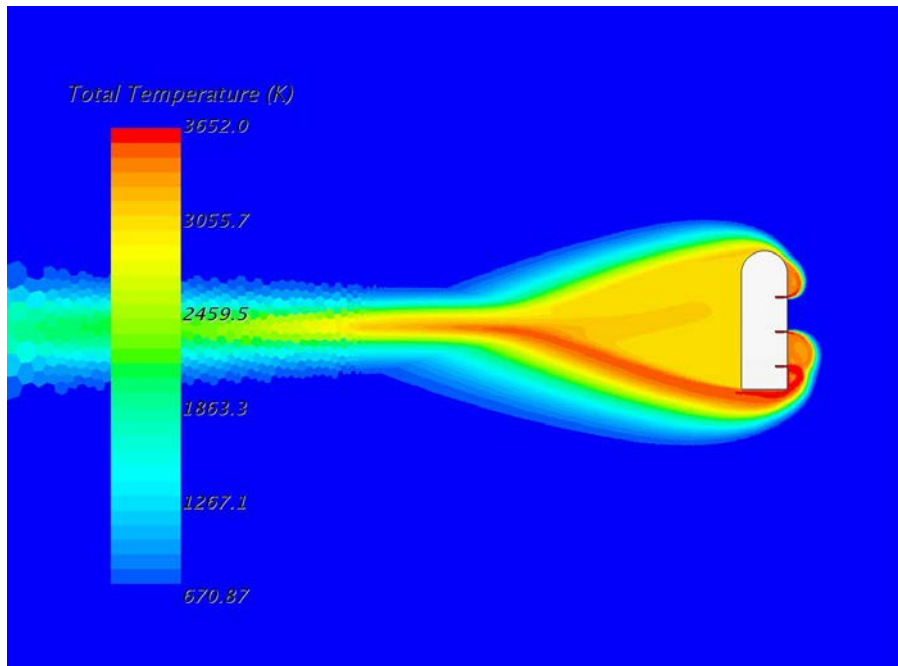


Fig. 156 $\alpha = 90^\circ$, Mach 2.5, Refined Mesh

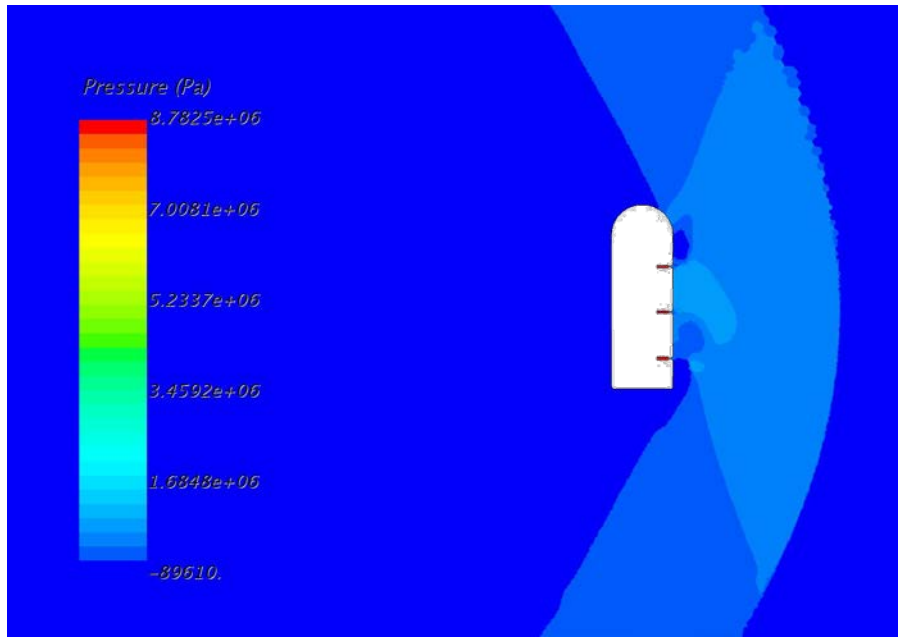


Fig. 157 $\alpha = 90^\circ$, Mach 2.5, Refined Mesh

Appendix B - Bell Nozzle MATLAB Code

```
% This LaTeX was auto generated from MATLAB code.
% To make changes, update the MATLAB code and republish this document.

%% Workspace Cleanup
clc, clear all, close all

%% CEA Stuff
% Necessary Values are O/F, Pressure, Temperature, and Gamma
OF = [1.5 1.6 1.7 1.8 1.9 2.0 2.1 2.2 2.3 2.4 2.5 2.6 2.7 2.8 2.9];

P_Chamber = [3.0 4.0 5.0 6.0 7.0 8.0 9.0 10.0 11.0 12.0 13.0 14.0 15.0]*10^6;

% Temperature
T = [2928.29 2937.98 2944.93 2950.25 2954.51 2958.02 2960.99 2963.54 2965.77
2967.74 2969.49 2971.07 2972.51;
3083.25 3097.48 3107.84 3115.86 3122.34 3127.73 3132.31 3136.27 3139.75
3142.83 3145.60 3148.10 3150.37;
3214.45 3233.48 3247.52 3258.51 3267.46 3274.95 3281.37 3286.95 3291.88
3296.26 3300.21 3303.79 3307.06;
3323.66 3347.50 3365.28 3379.34 3390.88 3400.60 3408.98 3416.30 3422.79
3428.60 3433.85 3438.62 3442.99;
3412.63 3441.07 3462.51 3479.58 3493.70 3505.67 3516.03 3525.13 3533.23
3540.51 3547.11 3553.14 3558.67;
3483.34 3515.98 3540.79 3560.70 3577.25 3591.38 3603.65 3614.49 3624.17
3632.90 3640.84 3648.11 3654.81;
3538.09 3574.36 3602.14 3624.57 3643.33 3659.40 3673.43 3685.86 3697.01
3707.09 3716.29 3724.74 3732.54;
3579.42 3618.69 3648.95 3673.51 3694.13 3711.88 3727.43 3741.25 3753.68
3764.96 3775.27 3784.77 3793.56;
3609.83 3651.48 3683.71 3709.98 3732.12 3751.23 3768.03 3783.00 3796.50
3808.77 3820.02 3830.41 3840.04;
3631.59 3675.03 3708.79 3736.38 3759.70 3779.88 3797.65 3813.53 3827.87
3840.94 3852.94 3864.03 3874.33;
3646.55 3691.33 3726.21 3754.79 3778.99 3799.98 3818.49 3835.06 3850.04
3863.72 3876.29 3887.93 3898.75;
3656.24 3701.96 3737.65 3766.94 3791.78 3813.35 3832.41 3849.48 3864.94
3879.06 3892.06 3904.10 3915.31;
3661.80 3708.17 3744.42 3774.20 3799.49 3821.47 3840.91 3858.34 3874.13
3888.57 3901.87 3914.19 3925.68;
3664.14 3710.92 3747.53 3777.64 3803.22 3825.47 3845.17 3862.83 3878.85
3893.50 3907.00 3919.53 3931.20;
3663.95 3710.96 3747.77 3778.07 3803.83 3826.24 3846.09 3863.90 3880.06
3894.84 3908.47 3921.12 3932.91];

% Ratio of specific heat
G = [1.2192 1.2226 1.2251 1.2271 1.2287 1.2301 1.2312 1.2322 1.2331
1.2339 1.2346 1.2353 1.2359;
1.2018 1.2053 1.2080 1.2101 1.2119 1.2134 1.2147 1.2158 1.2168
1.2177 1.2185 1.2193 1.2199;
1.1871 1.1906 1.1932 1.1954 1.1971 1.1987 1.2000 1.2012 1.2022
1.2032 1.2040 1.2048 1.2056];
```


1.1747 1.1780 1.1806 1.1826 1.1844 1.1859 1.1872 1.1884 1.1894
 1.1904 1.1912 1.1920 1.1928;
 1.1645 1.1675 1.1699 1.1718 1.1735 1.1749 1.1761 1.1773 1.1783
 1.1792 1.1800 1.1808 1.1815;
 1.1562 1.1590 1.1611 1.1629 1.1644 1.1657 1.1668 1.1679 1.1688
 1.1697 1.1705 1.1712 1.1719;
 1.1497 1.1522 1.1541 1.1557 1.1570 1.1582 1.1592 1.1602 1.1610
 1.1618 1.1625 1.1632 1.1638;
 1.1448 1.1470 1.1487 1.1501 1.1513 1.1523 1.1533 1.1541 1.1549
 1.1556 1.1562 1.1568 1.1573;
 1.1410 1.1430 1.1445 1.1458 1.1469 1.1478 1.1486 1.1494 1.1501
 1.1507 1.1513 1.1518 1.1523;
 1.1382 1.1400 1.1414 1.1425 1.1435 1.1444 1.1451 1.1458 1.1464
 1.1470 1.1475 1.1480 1.1484;
 1.1360 1.1377 1.1390 1.1401 1.1410 1.1418 1.1424 1.1431 1.1436
 1.1441 1.1446 1.1450 1.1454;
 1.1344 1.1359 1.1372 1.1382 1.1390 1.1397 1.1404 1.1410 1.1415
 1.1419 1.1424 1.1428 1.1432;
 1.1330 1.1346 1.1357 1.1367 1.1375 1.1382 1.1388 1.1393 1.1398
 1.1403 1.1407 1.1410 1.1414;
 1.1320 1.1334 1.1346 1.1355 1.1362 1.1369 1.1375 1.1380 1.1385
 1.1389 1.1393 1.1397 1.1400;
 1.1311 1.1325 1.1336 1.1345 1.1353 1.1359 1.1365 1.1370 1.1374
 1.1378 1.1382 1.1385 1.1389];

%Molecular weight, g/mol

MW= [17.397 17.411 17.422 17.430 17.436 17.441 17.446 17.450 17.453
 17.456 17.459 17.461 17.463;
 18.004 18.026 18.042 18.055 18.065 18.073 18.080 18.087 18.092
 18.097 18.101 18.105 18.109;
 18.581 18.612 18.635 18.652 18.667 18.679 18.690 18.699 18.707
 18.714 18.721 18.727 18.732;
 19.128 19.168 19.197 19.221 19.241 19.257 19.271 19.284 19.295
 19.305 19.314 19.322 19.329;
 19.643 19.692 19.730 19.759 19.784 19.805 19.823 19.839 19.853
 19.866 19.878 19.888 19.898;
 20.128 20.186 20.230 20.266 20.295 20.321 20.343 20.363 20.380
 20.396 20.411 20.424 20.436;
 20.582 20.648 20.699 20.740 20.775 20.805 20.831 20.854 20.875
 20.894 20.911 20.927 20.942;
 21.007 21.080 21.138 21.184 21.223 21.257 21.287 21.313 21.337
 21.359 21.379 21.397 21.414;
 21.405 21.486 21.548 21.599 21.642 21.680 21.713 21.742 21.769
 21.793 21.815 21.836 21.855;
 21.780 21.866 21.933 21.988 22.034 22.075 22.110 22.142 22.171
 22.198 22.222 22.245 22.266;
 22.134 22.224 22.294 22.353 22.402 22.445 22.483 22.517 22.548
 22.577 22.603 22.627 22.649;
 22.468 22.562 22.636 22.696 22.748 22.793 22.833 22.869 22.902
 22.932 22.959 22.985 23.009;
 22.785 22.882 22.958 23.021 23.075 23.122 23.164 23.201 23.235
 23.266 23.295 23.322 23.346;
 23.087 23.187 23.265 23.330 23.385 23.433 23.476 23.515 23.550
 23.582 23.612 23.639 23.665];

```

    23.375 23.477 23.557 23.623 23.679 23.729 23.773 23.812 23.848
23.881 23.912 23.940 23.966];

```

```

%% Preliminary Plotting

```

```

% Mainly used to demonstrate trends that occur

```

```

figure
hold on
for i = 1:length(OF)
    name = ['O/F:' ' ' num2str(OF(i))];
    plot(P_Chamber/10^6, T(i,:), 'displayname', name)
end
title('Temperature vs. Chamber Pressure')
xlabel('Pressure (MPa)')
ylabel('Temperature (K)')
legend('show')
hold off

```

```

%% All the Initial Conditions

```

```

R = 8314; %gas constant
G_0 = 9.8; %gravity earth
G_m = 3.711; %gravity mars

thrust = 600; %Newtons
F_thrust = 0; %initialization variable. Don't have to change. If we do make
P_ambient = 101325; %Pressure ambient
P_exit = 101235; %exit at nozzle
dia_e = 0.0127; %initial guess at exit diameter

Lstar = 0.9; %characteristic length of combust chamber., dependent on fuel
IT_ratio = 10; %injector to throat ratio, will decide combust dia
theta_c = 40*pi/180; %contraction, combust chamber
theta_e = 15*pi/180; %exit divergence

```

```

% index of O/F Ratio used

```

```

i = 7;

```

```

% index of Pressure used

```

```

j = 7;

```

```

%% Rocket Design Calculations

```

```

while F_thrust < thrust
    Ve = sqrt((2 * G(i, j) / (G(i, j) - 1)) * ...
        (R / MW(i, j) * T(i, j)) * ...
        (1 - (P_exit / P_Chamber(j)) ^ ((G(i, j) - 1) / G(i, j))));
    area_e = pi * (dia_e / 2) ^ 2;

    ep1 = (2 * G(i, j) / (G(i, j) - 1));
    ep2 = (P_exit / P_Chamber(j)) ^ (2 / G(i, j));
    ep3 = 1 - (P_exit / P_Chamber(j)) ^ ((G(i, j) - 1) / G(i, j));
    area_t = area_e / gammad(G(i, j)) * sqrt(ep1 * ep2 * ep3);

    m_dot = P_Chamber(j) * area_t * gammad(G(i, j)) / sqrt(R / MW(i, j) * T(i, j));

```

```

        F_thrust = m_dot*Ve+(P_exit-P_ambient)*area_e;
        if F_thrust < thrust
            dia_e = dia_e + 0.0005;
        end
    end

err = abs(thrust-F_thrust)/thrust;
epsilon = area_e/area_t;

Veq = F_thrust/m_dot;

Isp = Veq/abs(G_0).5*(1+cos(theta_e));

M_exit = sqrt(2/(G(i,j)-1)*((P_Chamber(j)/P_ambient)^((G(i,j)-1)/G(i,j))-1));
dia_t = 2*sqrt(area_t/pi);

area_i = area_t*IT_ratio;
dia_i = 2*sqrt(area_i/pi);

volume_c = Lstar*area_t;
len_c = 4*volume_c/(pi*dia_i^2) + (dia_i^3 - dia_t^3)/(6*dia_i^2) + (dia_i - dia_t)/(2*tan(theta_e));
len_e = (dia_e - dia_t)/(2*tan(theta_e));

conical_engine_misc = table([theta_c, theta_e, Lstar, epsilon, OF(i)],...
    'rownames',{'Contraction Angle','ExpansionAngle','L*','Epsilon','O/F Ratio'})
conical_engine_dims = table([dia_i,dia_t,dia_e,len_c,len_e],...
    [dia_i,dia_t,dia_e,len_c,len_e]/0.0254,...
    'rownames',{'Combustor Diameter','Throat Diameter','Nozzle Exit Diameter','Length of Co'})
    'variablenames',{'Metric','Imperial'})

%% Bell Nozzle Stuff
percent_bell = 0.8;

dia_e_bell = sqrt(epsilon)*dia_t;
len_e_bell = percent_bell*len_e;
expan_radius = 0.382*dia_t/2;
contrac_radius = 1.5*dia_t/2;

theta_e = 7;
theta_n = 33;

Bell_engine_misc = table([theta_c, theta_e, Lstar, epsilon, OF(i)],...
    'rownames',{'Contraction Angle','ExpansionAngle','L*','Epsilon','O/F Ratio'})
Bell_engine_dims = table([dia_i,dia_t,dia_e_bell,len_c,len_e_bell,expan_radius,contrac_rad],...
    [dia_i,dia_t,dia_e_bell,len_c,len_e_bell,expan_radius,contrac_radius]/0.0254,...

```

```
'rownames',{ 'CombustorDiameter','ThroatDiameter','NozzleExitDiameter','LengthofCombustor' },  
'variablenames',{ 'Metric','Imperial' })
```

```

%% More Bell Nozzle Stuff
R_t = dia_t/2;

theta_throat = deg2rad(135:90);
x_throat = 1.5*R_t/2*cos(theta_throat);
y_throat = 1.5*R_t*sin(theta_throat)+1.5*R_t+R_t;

theta_exit = deg2rad(90:theta_n 90);
x_exit = 0.382*R_t*cos(theta_exit);
y_exit = 0.382*R_t*sin(theta_exit) + 0.382*R_t+R_t;

t = 0:.01:1;

N_x = x_exit(end);
N_y = y_exit(end);

E_x = len_e_bell;
E_y = dia_e_bell/2;

m1 = tan(deg2rad(theta_n));
m2 = tan(deg2rad(theta_e));

C1 = N_y - m1*N_x;
C2 = E_y - m2*E_x;
Q_x = (C2 - C1)/(m1 - m2);
Q_y = (m1*C2 - m2*C1)/(m1 - m2);

for i = 1:size(t,2)
    x_bell(i) = (1-t(i))^2*N_x + y - 2*(1-t(i))*t(i)*Q_x + t(i)^2*E_x;
    y_bell(i) = (1-t(i))^2*N_y + 2*(1-t(i))*t(i)*Q_y + t(i)^2*E_y;
end

x = [x_throat,x_exit,x_bell];
y = [y_throat,y_exit,y_bell];

figure
hold on
plot(x,y)
plot(x,y)
axis equal

%% Nozzle Stuff for CAD
num_of_segments = 4;

NQ_step = (Q_x - N_x)/num_of_segments;
NQ_points = zeros(2,num_of_segments + 1);
QE_points = zeros(2,num_of_segments + 1);

for i = 1:num_of_segments + 1
    NQ_points(1,i) = N_x + NQ_step*i;
    NQ_points(2,i) = m1*NQ_points(1,i) + C1;
end

```

```

QE_step = (E_x - Q_x)/num_of_segments;
for i = 1:num_of_segments - 1
    QE_points(1,i) = Q_x + QE_step*i;
    QE_points(2,i) = m2*QE_points(1,i) + C2;
end

scatter(NQ_points(1,:),NQ_points(2,:));
scatter(QE_points(1,:),QE_points(2,:));

for i = 1:num_of_segments - 1
    plot([NQ_points(1,i);QE_points(1,i)],[NQ_points(2,i);QE_points(2,i)],'r')
end

function [ val ] = gammag( gamma )
% Summary of this function goes here
% Detailed explanation goes here
val = sqrt(gamma * ((1 + gamma)/2)^((1 + gamma)/(1 - gamma)));

end

```